

Computational Modeling of Structural Energy Storage

by
Somayeh Sarah Rezaei Aderyani

A dissertation submitted to the Department of Mechanical Engineering
Cullen College of Engineering
in partial fulfillment of the requirements for the degree of

DOCTOR OF PHILOSOPHY

in Mechanical Engineering

Chair of Committee: Dr. Haleh Ardebili

Committee Member: Dr. Pradeep Sharma

Committee Member: Dr. Yashashree Kulkarni

Committee Member: Dr. Jae-Hyun Ryou

Committee Member: Dr. Debora Rodrigues

University of Houston
May 2020

Copyright 2020, Somayeh Sarah Rezaei Aderyani

DEDICATION

This dissertation is dedicated to my husband, Yahya, who has been a constant source of support and encouragement during the challenges of graduate school and life. I am truly thankful for having you in my life.

This PhD thesis is also dedicated to my parents, Ahmad and Monireh, who have always loved me unconditionally and taught me anything is possible with hard work, determination, and dedication.

ACKNOWLEDGEMENTS

I would like to thank the University of Houston for providing me this learning opportunity and I appreciate the financial support from AFOSR and TcSUH that funded the research discussed in my dissertation.

Foremost, I would like to thank and express my sincere gratitude to my advisor Dr. Haleh Ardebili for her support, guidance, and helpful advice during my doctoral study. I would like to thank for her motivation, enthusiasm, immense knowledge and being patient with me and trusting me to perform my work.

I would like to thank my graduate committee members Dr. Pradeep Sharma, Dr. Yashashree Kulkarni, and Dr. Jae-Hyun Ryou from department of Mechanical Engineering and Dr. Debora Rodrigues from department of Civil and Environmental Engineering for serving as a member of my dissertation committee and reviewing my thesis. All the fruitful discussions, valuable suggestions, and the constructive criticisms have been much appreciated.

I would also like to extend my deepest gratitude to Dr. Jodie L. Lutkenhaus, Dr. Micah J. Green, Dr. James G. Boyd and Dr. Dimitris C. Lagoudas from Texas A&M University for the assistance they provided on my research during these years.

Last, but certainly not the least, I am really appreciative of all my colleagues and friends from University of Houston and Texas A&M University for their constant encouragement and support. This work would not have been possible without their continuous help and contributions.

ABSTRACT

Flexible structural energy storage is a rapidly emerging area with tantalizing applications such as integrated devices in textiles and smart suits, portable electronic devices and electric vehicles (EV). Due to several outstanding properties, graphene oxide (rGO)/ aramid nanofiber (ANF) composite material has emerged as a compelling choice as a structural electrode for supercapacitors and batteries. A key question of significant technological relevance pertains to what kind of nanoscale architecture motifs may lead to enhanced ionic diffusivity — the key characteristic dictating the overall performance of the electrode. In this work, we attempt to address this precise question, through multiphysics computational modeling in the context of several experimentally realizable nanoarchitectures, namely, “layered” and “house of cards” nanostructures. We investigate different arrangements (staggered, aligned and square) with various degrees of waviness of the rGO nanosheets inside the ANF polymer matrix.

Nanoarchitecture modeling results indicate that decreasing waviness of the rGO sheets can enhance the ion diffusivity in the staggered and aligned arrangements of the electrode material, while this effect is stronger in staggered arrangement than aligned arrangement. The results obtained from nanoarchitecture computational modeling are compared to the porous media approach. It is shown that the widely used porous electrode theory such as Bruggeman or Millington-Quirk relations, overestimates the effective diffusion coefficient. Also, the results from nanoarchitecture modeling are validated with experimental measurements obtained from impedance spectroscopy (EIS) and cyclic voltammetry (CV). The effective diffusion coefficients obtained from nanoarchitectural modeling show better agreement with experimental measurements.

The effective properties obtained from nanoarchitecture modeling is used to simulate cyclic voltammetry (CV) of rGO/ANF structural supercapacitors. Various electrochemical kinetics evaluated to characterize structural supercapacitors. The insights obtained from this study can lead to a more effective design of electrode architectures.

Finally, the effect of temperature on solid polymer Li-ion batteries is investigated through a 1D model that predicts the discharge behavior of flexible pouch cells at different temperatures. The simulations results show a good agreement with experimental measurements and yields fundamental insight which is essential for future developments in flexible solid polymer Li-ion batteries.

TABLE OF CONTENTS

DEDICATION	iii
ACKNOWLEDGEMENTS	iv
ABSTRACT.....	v
LIST OF TABLES	ix
LIST OF FIGURES	x
1 INTRODUCTION	1
1.1 Scope and Outline of This Dissertation	2
1.2 Electrochemical Energy Storage	5
1.3 Computational Modeling of Electrochemical Systems.....	7
1.4 COMSOL Multiphysics.....	8
2 Structural Supercapacitors	10
2.1 Overview	10
2.2 Reduced Graphene Oxide/Aramid Nanofiber Structural Electrodes.....	12
3 The Effect of Electrode Nanoarchitecture on Ionic Diffusivity	17
3.1 Introduction.....	17
3.2 Geometry Development.....	19
3.3 Ionic Transfer in Electrode Material.....	24
3.4 Results and Discussion	27
3.5 Conclusions.....	34
4 Nanoarchitecture vs. Porous Media Diffusion Models.....	35
4.1 Introduction.....	35
4.2 Digital Image Processing.....	36
4.3 Nanoarchitecture Based Computational Modeling	41
4.4 Governing Equations.....	42
4.5 Experimental Section.....	45
4.6 Results and Discussion	46
5 Computational Modeling of rGO/ANF Structural Supercapacitors	54

5.1	Introduction.....	54
5.2	Modeling Cyclic Voltammetry.....	55
5.3	Governing Equations.....	59
5.4	Modeling Assumptions	62
5.5	Results and Discussion	63
5.6	Conclusions.....	67
6	Solid Polymer Lithium-Ion Batteries	68
6.1	Overview	68
6.2	Polyethylene Oxide Solid Polymer Li-Ion Batteries	69
6.3	Thermal Modeling of Li-Ion Batteries.....	70
7	The Effect of Low Temperatures on Solid Polymer Li-Ion Batteries	72
7.1	Introduction.....	72
7.2	Governing Equations.....	73
7.3	Results and Discussion	77
7.4	Conclusions.....	80
8	Conclusions and Future Work.....	81
8.1	Conclusions.....	81
8.2	Future Work.....	83
	References.....	85
	Appendix A.....	113
	Appendix B.....	122

LIST OF TABLES

Table 1.1	Comparison of key parameters between supercapacitors and Li-ion batteries...	5
Table 3.1	Summary of various modeling approaches to investigate diffusivity [108].	18
Table 3.2	Simulation results for effective diffusion coefficient and tortuosity [108].	34
Table 4.1	Summary of SEM image processing for porosity measurement [135].	39
Table 4.2	Summary of SEM image processing to estimate length and thickness [135]. ..	40
Table 4.3	Comparison of transport properties of house of cards nanostructure [135].	52
Table 4.4	Comparison of transport properties of layered nanostructure [135].	52
Table 5.1	Parameters used in simulation of CV measurements of rGO/ANF electrodes.	62
Table 5.2	Resistance and capacitance obtained as fitting parameters in the simulation. ..	66
Table A.1	Diffusion coefficient (m^2/s) for common ions in various electrolytes [108].	121

LIST OF FIGURES

Figure 1.1 The Dissertation Summary	4
Figure 1.2 Ragone plot for electrochemical energy storage [23][24].	6
Figure 1.3 (a) Supercapacitors, and (b) Li-ion batteries in limited shape factors of prismatic, cylindrical, and coin cells.....	7
Figure 2.1 Structure of an ideal supercapacitor.	11
Figure 2.2 (a) Vacuum filtered rGO/ANF sample, (b) SEM images of cross-sectional area of layered nanostructure [108].	14
Figure 2.3 (a) Hydrogel rGO/ANF sample, (b) SEM images of different compositions of house of cards with compressed and uncompressed configurations [108].	15
Figure 3.1 Aligned and staggered arrangements of rGO nanosheets (flat and wavy) describing layered nanostructure [108].....	19
Figure 3.2 (a) Characterizing waviness (w) based on parallel sine curves, (b) geometry development for one rGO sheet in COMSOL [108].....	21
Figure 3.3 Developed geometries for nanocomposite representative volume considering different rGO nanosheets waviness [108].....	23
Figure 3.4 Electric potential in electrolyte solution between rGO/ANF nanosheets [108].	25
Figure 3.5 Concentration contour plots, $D = 10^{-10} \text{ m}^2/\text{s}$ [108].	28
Figure 3.6 Concentration-time plots for three points shown in the staggered arrangement indicating three-time stages of diffusion development: 1) linear area, 2) transition area, and 3) saturated area [108].....	29
Figure 3.7 Ionic flux streamlines along the red line causes the sharp point in the middle of the concentration-distance plots [108].....	30
Figure 3.8 The effect of diffusion coefficient on concentration development for staggered arrangement with $w = 1/24$, $D = 10^{-9}$ to $10^{-6} \text{ m}^2/\text{s}$ [108].....	31
Figure 3.9 (a) The effect of rGO waviness on ionic diffusivity in staggered arrangement, (b) increasing rGO waviness impedes the ionic diffusivity [108].	32
Figure 3.10 Average concentration-time ^{1/2} plot ($D = 10^{-10} \text{ m}^2/\text{s}$) is used to calculate effective diffusivity and tortuosity [108].	33

Figure 4.1 SEM Images of rGO/5%wt ANF nanocomposites through different fabrication methods [135].	37
Figure 4.2 Threshold applied to SEM images of house of cards and layered nanostructures, (a) Scanning Probe Image Processing software, and (b) ImageJ software [135].	38
Figure 4.3 Pore area distribution for one SEM image of rGO/ANF sample [135].	39
Figure 4.4 Image processing method to estimate (a),(b) the length and thickness of rGO/ANF nanosheets, (c),(d) the void fraction volume of nanocomposites for house of cards and layered structure, respectively [135].	40
Figure 4.5 (a) average thickness distribution, (b) average length distribution of rGO/ANF nanosheets, (c), and (d) average porosity distribution for house of cards and layered nanocomposites, respectively [135].	41
Figure 4.6 Unit cell development for (a) house of cards, (b) layered nanostructure based on SEM images; The rGO/ANF nanosheets, represented by gray rectangles as building blocks of each unit cell, are arranged in square and staggered configurations to describe house of cards and layered nanostructures, respectively [135].	42
Figure 4.7 Applied boundary conditions in each geometry [135].	45
Figure 4.8 (a),(b) K^+ ions concentration contour plots, and (c),(d) electric potential profiles for square and staggered nanoarchitecture unit cells [135].	47
Figure 4.9 Concentration-time plot of K^+ and OH^- at point P shows that ions progress in the unit cell through a Fickian diffusion mechanism [135].	48
Figure 4.10 Concentration-length plot for line L shows that K^+ ions are attracted towards the negatively charged rGO/ANF surface while OH^- ions are repelled [135].	49
Figure 4.11 Electric potential profile at $t = 0s$ and $t = 0.05s$ for (a) Line L, (b) nanochannel. The electric potential near the surface of rGO/ANF sheets is -1 mV and at the center of line L goes to zero and increases to -0.986mV for nanochannel [135].	50
Figure 4.12 Average concentration-time ^{1/2} for house of cards and layered structures to calculate effective diffusion coefficient of K^+ ions [135].	51
Figure 4.13 Comparison of the calculated D_{eff} for porosity% (0-70%) through porous media approaches and nanoarchitecture modeling [135].	53
Figure 4.14 Path tracking method to calculate the tortuosity of the nanoarchitectures regarding $\tau = L_1/L_0$ which is defined as the shortest pathway between two points within the geometry; Curve C_1 can represent the longest pathway between two points [135].	53

Figure 5.1 Schematics of rGO/ANF structural supercapacitor with house of cards nanoarchitecture.....	54
Figure 5.2 Ideal supercapacitor modeling for cyclic voltammetry measurements of rGO, rGO/10%ANF, and rGO/25%ANF.....	64
Figure 5.3 Comparison of various electrode kinetics for rGO/25%ANF CV measurements.....	65
Figure 5.4 (a) Triangular cyclic potential sweep from 0V to 1V during two cycles, (b) the average current density obtained in a form of step function.....	65
Figure 5.5 (a) Ion concentration development in the diffuse layer for rGO/10%wtANF with 20 mV/s scan rate obtained from modeling CV, (b) concentration profile at time 0s and after 200s.....	66
Figure 6.1 Ionic conductivity in solid polymer electrolyte is due to polymer chain segmental mobility [218].	69
Figure 7.1 Schematics of pouch cell and the single particle model [223][224][225].	72
Figure 7.2 Equilibrium potential vs. SOC for Graphite and LiCoO ₂ [45][114].	75
Figure 7.3 Potential (V) vs. discharge capacity (mAh/cm ²) through both modeling and experimental measurements. The model can predict the battery performance in low temperatures.....	78
Figure 7.4 Temperature profile for 4°C, 10°C, and 25°C.....	79
Figure 7.5 Modeling shows by increasing salt concentration in negative electrode the battery performance can be improved at 4°C.	79
Figure A.1 Schematics of vacuum filtration method [15][16][17][18][108].	113
Figure A.2 Schematics of sol-gel method [19][72].	114
Figure A.3 1D and 2D geometry development with boundary conditions; blue indicates zero flux and red indicates $c=c_0$ [108].	116
Figure A.4 One-dimensional diffusion mass transfer is preferred in thin films, when the value of diameter/thickness ratio of the sample is large enough to neglect the diffusion of ions from the sample edges [108].	117
Figure A.5 Series and parallel laminates and related equations to determine effective diffusion coefficient [108][117][118].	117

Figure A.6 Concentration contour plots for rGO/25wt%ANF in aligned and staggered arrangements with various degrees of waviness of $a/\lambda = 1/16, 1/24, 1/32$, and 0 (straight sheets) [108].	118
Figure A.7 Concentration-time plot of 3-points in the geometry- left (blue), middle (green), and right (red). These plots indicate that how ion transfer develops through the geometry in three-time stages: (1) time needed for ions to reach the point, (2) transient, and (3) equilibrium [108].	119
Figure A.8 The effect of diffusion coefficient on concentration for staggered arrangement with $w = 1/24$, $D = 10^{-17} \text{ m}^2/\text{s}$ to $D = 10^{-10} \text{ m}^2/\text{s}$ [108].	120
Figure A.9 (a),(b) Average concentration-time plots for aligned and staggered arrangements ($D = 10^{-10} \text{ m}^2/\text{s}$). Increasing waviness of rGO sheets, decreases the ionic concentration in both aligned and staggered arrangements. (c),(d) Average concentration-time ^{1/2} plots for aligned and staggered arrangements ($D = 10^{-10} \text{ m}^2/\text{s}$) is used to calculate effective diffusivity and tortuosity [108].	120
Figure B.1 Concentration contour plots for OH^- ions in (a) square unit cell for house of cards, and (b) staggered unit cell for layered nanoarchitectures [135].	122
Figure B.2 (a) Concentration-time plot for K^+ and OH^- at point P in staggered unit cell for layered nanostructure shows a Fickian diffusion behavior. (b) concentration development of K^+ and OH^- along line L in the nanochannel indicates that K^+ ions are accumulated at the rGO/ANF surface due to negatively charged surfaces and OH^- ions are repelled from the surfaces [135].	122
Figure B.3 Electric potential for line L in the nanochannel at time 0s and 0.01s, the electric potential is -1 mV at the rGO/ANF surface and goes to zero at the boundary condition in the middle of nanochannel [135].	123

NOMENCLATURES

A	Area of the electrode active material, m^2
A_c	Tafel slope, V
c_i	Salt concentration, mol/m^3
c_l	Solution phase concentration, mol/m^3
$c_{l,ref}$	Reference solution phase concentration (taken to be equal to 1 mol/m^3)
c_s	Concentration of lithium in the solid particles, mol/m^3
$c_{s,max}$	Maximum concentration, mol/m^3
C_p	Heat capacity at constant pressure, J/K
D_{eff}	Effective diffusion coefficient, m^2/s
D_i	Salt diffusion coefficient, m^2/s
D_s	Solid phase diffusion coefficient, m^2/s
$E_{a,j}$	Activation energy for solid phase diffusion coefficient of electrodes
E_{cell}	Cell potential, V
F	Faraday constant, 96487 C/mol
h	Heat transfer coefficient lumped factor, $Wm^{-2}K^{-1}$
I_{app}	Applied current density, A/m^2
i_0	Initial exchange current density, A/m^2
i_{loc}	Exchange current density, A/m^2
J	Flux of the species i by the electrochemical reactions, $mol\ s^{-1}m^2$
L	Thickness of the electrode, μm
M_t	Concentration at time t , mol/m^3
M_{eq}	Equilibrium concentration, mol/m^3
q	Rate of heat generation, W/m^3
R	Universal gas constant, $8.314\text{ J mol}^{-1}\text{ K}^{-1}$
R_j	Radius of the electrode particle, μm
R_{SPE}	Solid polymer electrolyte resistance, $\Omega.m^2$
SOC	State of charge
T	Temperature, K
t	Time, s
U	Open circuit equilibrium potential, V
v	Velocity of the bulk fluid, m/s
V_j	Total electrode volume, m^3
w	Waviness of rGO/ANF sheets
z_i	Number of charges

Greek

α	temperature correction factor
α_c	Cathodic transfer coefficient of surface reaction
δ	Diffuse layer thickness, nm
ϵ	Electrolyte permittivity or dielectric constant, F/m
ϵ_0	Vacuum permittivity, 8.85×10^{-12} F/m
ϵ_r	Relative permittivity
ϵ_s	Volume fraction of the solid phase active material in the electrode
η	Overpotential, V
φ_l	Potential of the solution phase, V
φ_s	Potential of the solid phase, V
$\Phi(x, t)$	Electric potential, V
κ	Reaction rate constant
κ_{eff}	Effective ionic conductivity of porous region, S/m
λ	Wavelength in sine wave, m
λ_j	Average thermal conductivity of porous region, W/m/K
λ_D	Debye length, nm
ρ	Density, kg/m ³
σ	Warburg coefficient, W s ^{-1/2}
σ_{eff}	Effective electronic conductivity of solid phase, S/m
ν	Voltammetric scan rate, V/s
τ	Tortuosity
ω	Angular frequency $2\pi f$, rad/s

1 INTRODUCTION

The world's heavy reliance on burning fossil fuels to produce energy plays a dominant role in global warming and climate change as a major source of local air pollution and emitter of greenhouse gases [1][2]. Since 1950 until now, climate change due to human activities has impacted the life on earth, dramatically. Warmer ocean waters, polar ice caps melting, stronger hurricanes, animal extinction or loss of habitat, and the spread of the diseases like the most recent crisis of COVID-19 pandemic are the direct consequences of climate change [3].

Considering the energy demand growth and the extreme necessity for emission-free energy sources to combat the climate change, fundamental research is needed for speeding up the transition to clean and renewable energy sources such as solar, wind, and electrochemical energy storage [4][5]. As a key partner of renewables, electrochemical energy storage is a standalone system that in contrast to solar and wind is not intermittent. Over the last decades, development of portable electrochemical energy storage, such as batteries and supercapacitors, has revolutionized the cellular phones and laptop computers and now enables the hybrid and all-electric vehicles [5]. Electrochemical system has demonstrated to be an auspicious approach to generate and store clean energy that eventually leads to climate change mitigation [5].

Driven by explosion in mobile and portable electronic devices and the proliferation of drones and electric vehicles, significant attention is directed towards developing new materials for energy storage with higher efficiency, longer life cycle, and flexible form factor [1][5][6]. An ultimate goal is to maximize power and energy densities of the energy storage via state-of-the-art composite materials. The next generation of energy storage

systems require development of multifunctional composite components that are lightweight, flexible and capable of load-bearing in addition to the high electrochemical performance [7][8][9]. In a wide variety of applications, from wearable biomedical sensors and smart electronic textiles to electric vehicles and power system stabilization in space launchers and satellites structural energy storage is a promising way to save weight and space of the device. Eliminating the casing and replacing each component with a reinforced composite that can tolerate cyclic loading will even lead to a safer energy storage technology. Technical breakthroughs gained by fundamental research, both experimentally and computationally, will lead to new concepts for high-power energy storage systems that meets the growing demand on flexible scalable power supply of the future [1][7][9][10][11][12][13][14].

1.1 Scope and Outline of This Dissertation

The main focus of this dissertation is to understand the transport phenomena and electrochemical performance of flexible structural energy storage devices through multiphysics computational modeling. Two different electrochemical energy storage have been studied in this dissertation. The first system presented here is the structural supercapacitor consisting of a new class of composite materials based upon reduced graphene oxide (rGO) and Kevlar[®] aramid nanofiber (ANF) [15][16][17][18][19]. This composite electrode material has demonstrated increases in elastic modulus and toughness and is a promising candidate for next generation flexible structural energy storage. In Chapter 2 it is shown that through different fabrication methods, various nanoarchitectures are produced in rGO/ANF structural electrodes. Two “layered” and “house of cards” nanostructures of rGO/ANF electrodes that obtained through vacuum filtration and sol-gel

methods respectively are compared through SEM images. Each of these nanoarchitectures has inherent tradeoffs with regard to electronic conductivity, ionic diffusivity, and mechanical properties.

In Chapter 3 a rigorous nanoarchitecture model is developed for layered nanostructure. Two staggered and aligned arrangements of rGO sheets are developed to investigate the effect of nanoarchitecture on ionic diffusivity. In addition, various degrees of waviness for rGO sheets are considered. The model presented in this study accounts the diffusion of ions in a Fickian mass transfer. The effective diffusivity obtained for each architecture compared with experimental results.

In Chapter 4 a 2D model is developed for house of cards nanostructure and the results for concentration and potential gradient are compared with porous electrode theory results. The simulation results are also compared with experimental measurements through cyclic voltammetry and electrochemical impedance spectroscopy.

In Chapter 5, a 1D model is developed to simulate the cyclic voltammetry of the whole cell supercapacitor made of rGO/ANF structural electrodes. In this study, different electrode kinetics are considered including Tafel equation and Butler-Volmer equation with very low current density. The simulation results are validated with experimental measurements. This rigorous model can serve as a benchmark for optimizing and designing new structural electrodes.

In the second part of this dissertation, the effect of low temperatures on flexible solid polymer electrolyte lithium-ion (Li-ion) batteries is investigated. The second energy storage is the flexible Li-ion batteries consisting of graphite (LiC_6) anode, lithium cobalt oxide (LiCoO_2) cathode, and Polyethylene oxide (PEO) solid polymer electrolyte (SPE).

In Chapter 6 a literature review on thermal modeling of Li-ion batteries is provided. The performance of solid polymer Li-ion batteries at low temperatures is investigated by developing a multiphysics 1D model. The heat transfer model is coupled with the electrochemical single particle battery model. The battery performance is simulated for temperatures of 4°C, 10°C, and 25°C and compared with experimental measurements. The mathematical development is presented in Chapter 7. Figure 1.1 shows the summary of the dissertation.

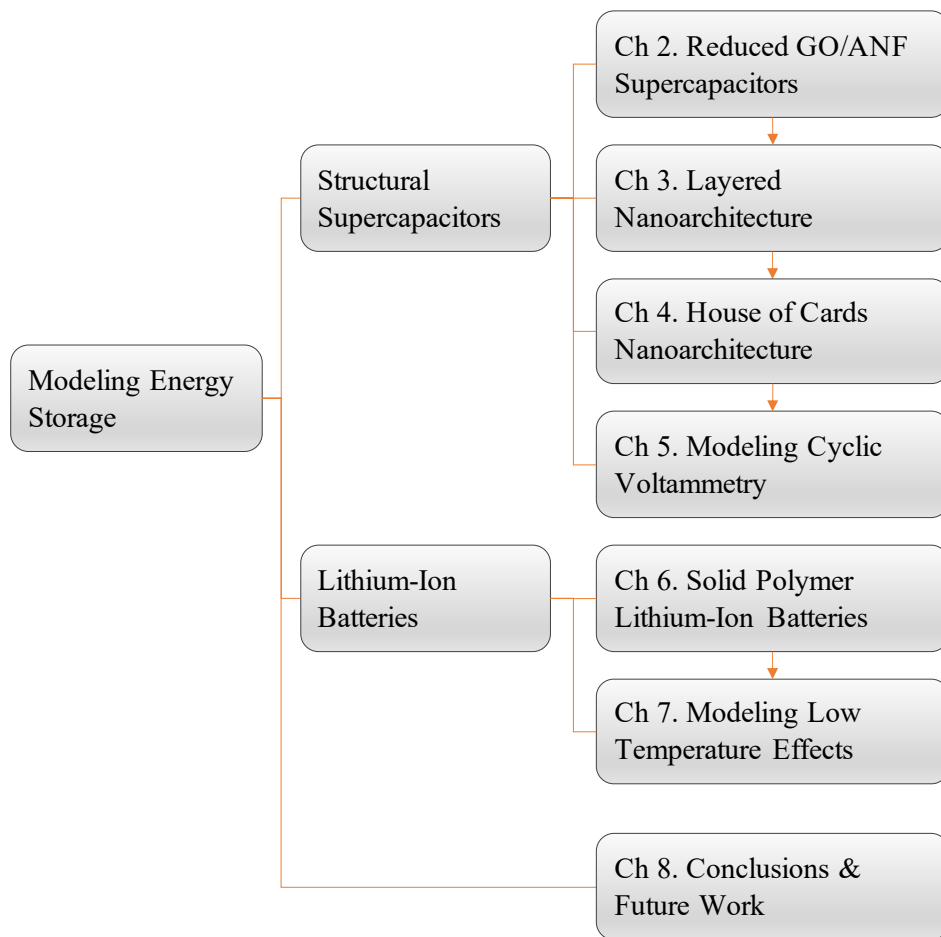


Figure 1.1 The Dissertation Summary.

1.2 Electrochemical Energy Storage

Two primary types of electrochemical energy storage systems are supercapacitors and Lithium-ion (Li-ion) batteries which are categorized as capacitive and chemical energy storage systems, respectively [20][21][22]. Supercapacitors and Li-ion batteries have relatively similar construction; however, they store energy in quite different mechanisms. Batteries store energy in the form of chemical energy through reactants (chemical energy storage), whereas electrical capacitors store electrical energy directly as electrostatic charge (capacitive energy storage) [21]. Three major electrochemically active components of supercapacitors and Li-ion batteries are anode, cathode and electrolyte. A nonconductive polymer separator contained with the electrolytic solution divides the electrodes preventing the internal short circuit [20][21][22]. Table 1.1 compares some of the key parameters of supercapacitors and Li-ion batteries based on data from Maxwell Technologies, Inc.

Table 1.1 Comparison of key parameters between supercapacitors and Li-ion batteries.

Specification	Supercapacitors	Li-Ion Batteries
Specific Energy (Wh/kg)	5 (typical)	100-265
Specific Power (W/kg)	Up to 10,000	1000-3000
Nominal Cell Voltage (V)	2.2-2.75	3.6-4.2
Life Cycle	> 1 million	> 500

Source: Maxwell Technologies, Inc.

The Ragone plot in Figure 1.2 demonstrates the general performance of supercapacitors and Li-ion batteries based on power density versus energy density. Li-ion batteries have higher energy density, while supercapacitors have higher power density [23][24]. A great volume of research studies in Li-ion batteries and supercapacitors is focused on improving the system performance and moving towards the top right corner of the Ragone plot to achieve higher energy and power densities [25][26][27][29][30][31].

Figure 1.3 shows the available conventional supercapacitors and Li-ion batteries in the market with limited form factor to only a few geometries (coin, cylindrical, and prismatic).

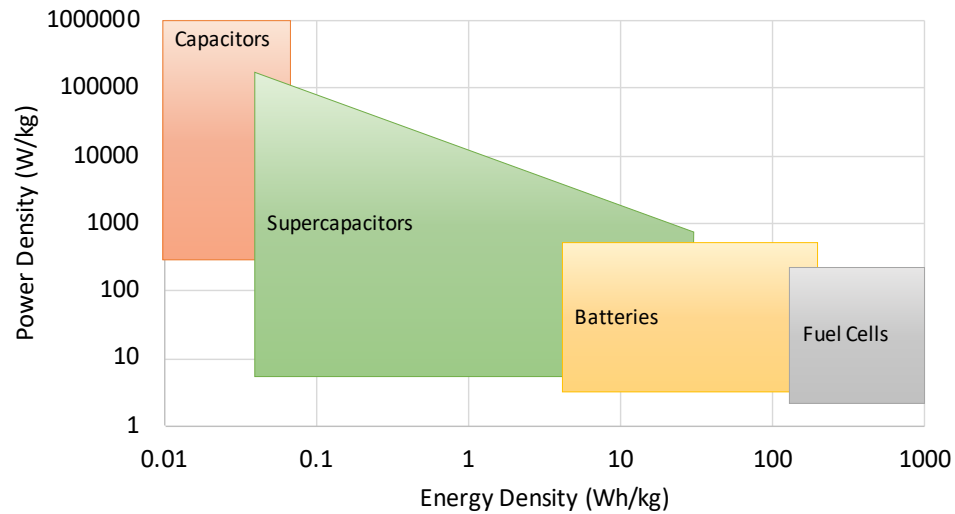


Figure 1.2 Ragone plot for electrochemical energy storage [23][24].

The design of batteries and supercapacitors with high energy-storage capabilities is an ongoing research, mainly focused on synthesis of new multifunctional nanostructured materials for electrodes and electrolyte components [8][9][10]. In the recent years, development of flexible energy storage devices has achieved tremendous interests due to emerging wearable and flexible electronics [14][32]. The main goal is to introduce various shape factors to the device while improving the device electrochemical performance. For example, in flexible Li-ion batteries replacing the liquid electrolyte with solid polymer electrolyte not only increases the device flexibility, but also improves the batteries safety[33][35]. Structural electrode materials are basically the reinforced electrode active materials with polymer matrix that enable more flexibility to the device [8][10].

The next generation of energy storage systems require development of multifunctional composite components that are structurally self-reliance in addition to high electrochemical performance [1][11][12][10]. Replacing each component with a reinforced

composite that can tolerate cyclic loading will eventually lead to a safer energy storage that can be incorporated into practically any portable electronics in many applications [35][36][37].

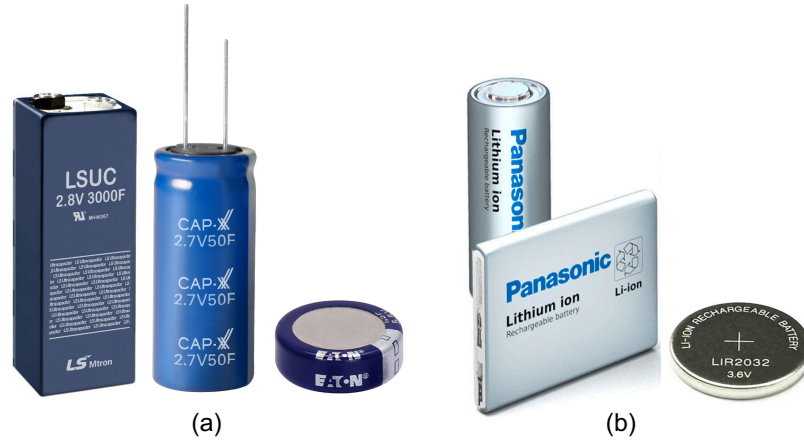


Figure 1.3 (a) Supercapacitors, and (b) Li-ion batteries in limited shape factors of prismatic, cylindrical, and coin cells.

The combination of experimental work with theory, modeling, and simulation contributes to understand the underlying processes in electrochemical systems. Theoretical development has enabled the rational design of nanostructured multifunctional materials with vastly improved performance, while lowered the cost of prototyping [38][39][40][41].

1.3 Computational Modeling of Electrochemical Systems

Quantitative understanding of material properties such as porosity, effective diffusion coefficient and electrical conductivity both through experiments and computational modeling plays a critical role to design nanocomposite structural electrode materials with optimal performance [38][39][40][41]. However, computational modeling compared with experiments is quicker and often more efficient in providing accurate optimization of processes and devices. Progress in modeling and fundamental understanding of the theories behind charge storage and transfer mechanism will accelerate

new material designs with higher energy and power at lower cost. Moreover, computational modeling can be beneficial to predict the system performance during charge-discharge cycling and under various operating conditions. A key factor in computational advances is validation of theoretical methods with experimental results that ensures the reliability of the models and further improvement of computational tools [1][38][39][40][41].

1.4 COMSOL Multiphysics

COMSOL Multiphysics® is a powerful simulation platform with finite element analysis solver that is employed to understand, design, and optimize processes and devices in a wide range of applications in areas of chemical, electrical, mechanical, fluid, acoustic, etc. The modules embedded in COMSOL software provide a modeling workflow from designing geometries, material properties, defining the physics of specific phenomena to solving and postprocessing the modeling results [42][43].

These modules are either exclusively engaged to investigate specific physical phenomena and maintain all the possible related boundary conditions or in general forms as mathematical expressions enabling the users to define their own conditions. For example, the mass transfer in a thin layer of charge in a diffuse double layer at the electrode/electrolyte interface can be easily studied through the Chemical Species Transport modules such as coupling Poisson-Nernst-Planck Equations, Transport of Diluted Species, and Transport of Concentrated Species modules [44].

The electrical and chemical characteristics of an electrochemical cell such as a supercapacitor or a battery can be explored through the Electrochemistry modules such as Electroanalysis, Battery Interfaces, and Li-ion Battery modules[44]. On the other hand, the users can adopt the Mathematics modules such as PDE Interfaces, Coefficient Form PDE

and General Form PDE to define a proper model based on their physics and have control over all aspect of the design. The ability of coupling any number of physical phenomena as well as user defined physics have made this software a suitable workbench for more creative and challenging problems [44][45]. Different studies are suggested by COMSOL for time-dependent, stationary or eigenfrequency conditions which the solution from any of the previous study steps can be used as input to the next study step [42][43][44][45].

Other advantages of COMSOL software can incorporate other programming languages like JAVA and MATLAB via LiveLinkTM to extend the modeling with scripting programming. Moreover, COMSOL supports all the standard CAD and ECAD files through CAD Import Module and Design Module that allows for import and export of a wide range of industry standard CAD files. The Application Builder in COMSOL contains functionality for building simulation applications with restricted inputs and outputs for a specific task [42][43].

The finite element method used in COMSOL Multiphysics solver is not as efficient as other available commercial software. In contrast, the finite volume method (FVM-based) software is usually faster and better suited for iterative solvers for specific fluid flows and mass transfer problems. In FEM solver, the computation time can increase significantly for complicated geometries and rigorous modeling equations. The accuracy of the solution also depends on the mesh size, complexity of the geometry, model equations and assigned initial and boundary conditions [46].

2 Structural Supercapacitors

2.1 Overview

Supercapacitors with their superior attributes including high power density and long life cycles, have become one of the highly attractive electrochemical devices, especially for those applications that require a sudden burst of energy supply such as regenerative braking in electric vehicles [1][7]. Recent developments in flexible and wearable electronics have driven the supercapacitor technology towards structural compatibility with a wide range of applications including the smart and portable electronics and biometrics, and in-ground and aerial vehicles [8-14]. To accomplish this goal, research efforts have been focused on developing novel structural electrode materials through both experimental and modeling approaches [15-19].

Supercapacitors also known as electrochemical capacitors or ultracapacitors are electrochemical energy storage that consist of two identical electrodes immersed in an electrolyte and separated by an ion permeable membrane[20]. The electrolyte is a mixture of positive and negative ions dissolved in a solvent. Electrical energy is stored in supercapacitors through the double-layer phenomenon. When a voltage is applied to a supercapacitor, ions with the opposite charge to the electrode's polarity form an electric double-layer at the electrode/electrolyte interfaces [21]. The double-layer consists of an electronic layer at the surface lattice structure of the electrode and a layer of ions with opposite polarity in the electrolyte. In the double-layer, two storage principles contribute in supercapacitors total capacitance: the capacitance due to electrostatic separation of charge in Helmholtz layer and the pseudocapacitance due to Faradic redox reactions with electron charge transfer in the double-layer. The latter happens when ions pervade the

double-layer becoming specifically adsorbed ions. Figure 2.1 shows the schematic of a typical supercapacitor [22].

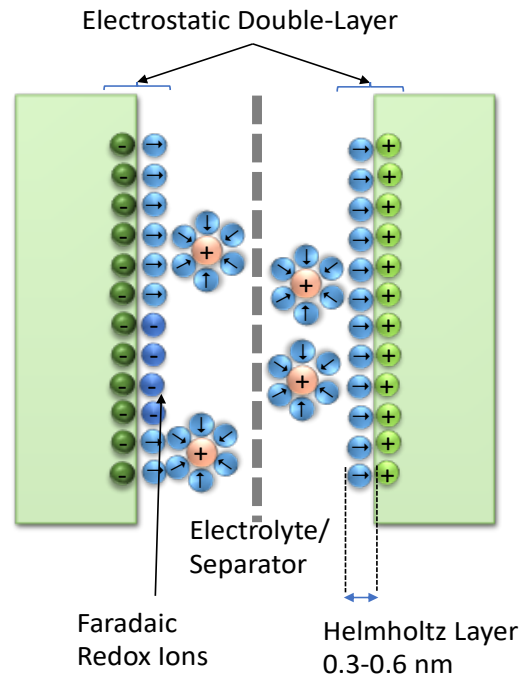


Figure 2.1 Structure of an ideal supercapacitor.

The adhesion forces in both storage principles are mainly electrostatic forces at the electrode surface and not due to chemical reactions and generation of chemical bonds. In the case of pseudocapacitors, only electron charge transfers between electrode and electrolyte in Faradic redox reaction [22][23]. Materials exhibiting electrochemical double layer behavior are activated carbon, porous carbon, carbon nanotube and graphene, whereas the materials with pseudocapacitors behavior are transition-metal oxides like RuO_2 , IrO_2 , or MnO_2 . Supercapacitors are used in applications requiring many rapid charge/discharge cycles, rather than long term compact energy storage [22][24][25][30][36][37].

Two dynamic modeling approaches are used to investigate the performance of supercapacitors [40][41]. The common standard model consists of equivalent RC circuits and transition-line. The RC models are oversimplified and can provide useful analytical formulae to interpret experimental measurements. Also, by considering more complicated equivalent circuits of nested transmission lines the effect of microstructure on capacitive charging can be determined. However, the equivalent RC circuit models cannot be used for predictive modeling since they are usually used to fit experimental data. Moreover, this modeling approach neglects the ionic diffusivity and nonuniform concentration of ions in the electrode/electrolyte interface[40]. The second approach is the dynamic modeling through coupled Poisson-Nernst-Planck equation. This model considers the transient electric potential and ionic concentration in the diffuse layer. This model is valid for binary symmetric electrolyte assuming identical diffusion coefficients for cations and anions. On the other hand, this model needs modification for modeling asymmetric concentrated electrolyte solution considering finite ion size. In the following chapters the Poisson-Nernst-Planck equation is adapted to model structural supercapacitors [41].

2.2 Reduced Graphene Oxide/Aramid Nanofiber Structural Electrodes

Although carbon-based materials including highly porous activated carbon, carbon nanofibers, and carbon nanotubes have been widely considered as electrode materials in supercapacitors [47][48][49][50], structural composite material made of reduced graphene oxide (rGO) embedded in aramid nanofiber (ANF) polymer matrix has attracted much interests due to its outstanding mechanical and electrochemical properties. Two-dimensional graphene-based materials have captured much attention in recent years as a promising candidate for structural electrodes [51][52][53][54][55][56][57][58][59]. The

large surface area to volume ratio of graphene can significantly increase the energy storage capability of supercapacitors. The ionic transfer along the flat surface area and through the layered structure of graphene sheets can be more efficient than through the pores in carbon-based materials [53][54]. The reduced graphene oxide (rGO) or functionalized graphene is one of the graphene-based materials overcomes the restacking issue in graphene layers. This is mainly attributed to the presence of the oxygen groups in the rGO that increases the interlayer distance between graphene sheets [55]. Restacking of graphene layers are generally caused by its highly active edge planes that can lead to surface access reduction and capacitance loss in the graphene electrode [56][57].

To enhance the mechanical properties of reduced graphene oxide as a flexible electrode, one strategy is to incorporate the graphene oxide into a polymer matrix and develop a hybrid nanocomposite material. Among polymers used in flexible electrodes, aramid nanofibers (ANFs) extracted from Kevlar (poly-phenylene terephthalamide, PPTA), has been considered as an auspicious possibility with remarkable mechanical properties [15][16][17][18][19][60][61][62][63][64][65]. Kevlar that is famously used for bullet-proof vests, is a fiber formed from rigid-rod polyaramid with high tensile modulus of 185 GPa and strength of 4 GPa [66][67]. Aramid nanofiber can provide a strong matrix for graphene-based materials, especially in applications that require frequent bending and deformation[67][68][69]. Common methodologies to fabricate rGO/ANF nanocomposite thin films include vacuum-assisted filtration, sol-gel process, and monolith technique[15][16][17][18][19]. A “layer-by-layer” thin film or paper like “brick-and-mortar” structure can be obtained through vacuum-filtration technique [15][16][17][18][61][70].

In vacuum-assisted filtration method, these two components are processed into free-standing electrodes. More specifically, GO/DMSO and ANF/DMSO dispersions are mixed together. Afterwards, water is added to re-protonate the ANF amide bonds and the mixture is vacuum filtrated. This leads to extensive hydrogen bonding and π - π stacking interactions between the ANF amide bonds and the GO oxygen-containing groups [15].

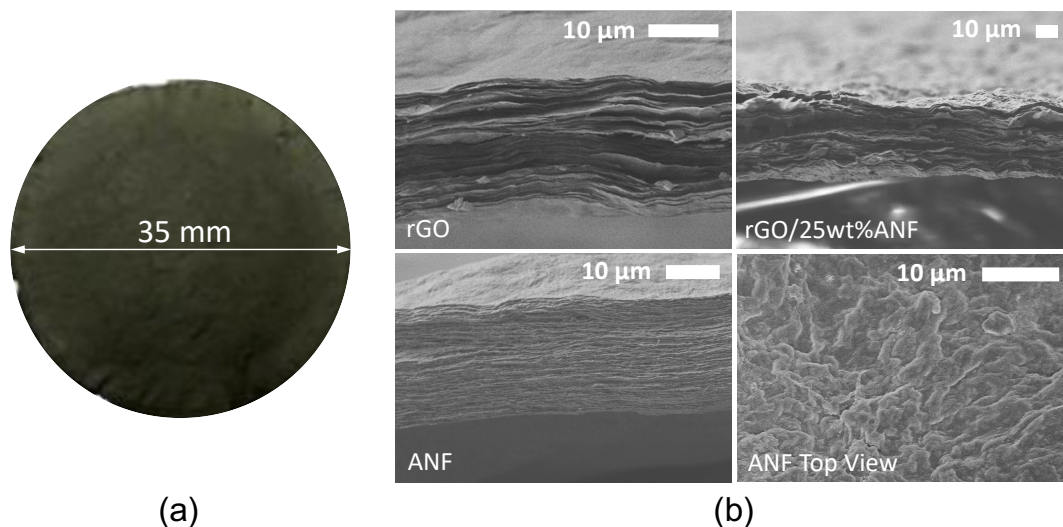


Figure 2.2 (a) Vacuum filtered rGO/ANF sample, (b) SEM images of cross-sectional area of layered nanostructure [108].

The as-prepared electrodes are thermally reduced to yield reduced graphene oxide composites (rGO/ANF). Cross-section SEM images reveal a highly layered structure with aligned, interlocking rGO/ANF nanosheets with high in-plane strength and out-plane flexibility and controllable compositions, as shown in Figure 2.2. The rGO nanosheets exhibit a wavy morphology and the ANFs are not observed from the SEM images due to their small size. The electrodes have thicknesses 8-16 μm . The schematics of vacuum filtration technique is shown in Figure A.1 and more details of experimental setup is provided in section A.1, Appendix A.

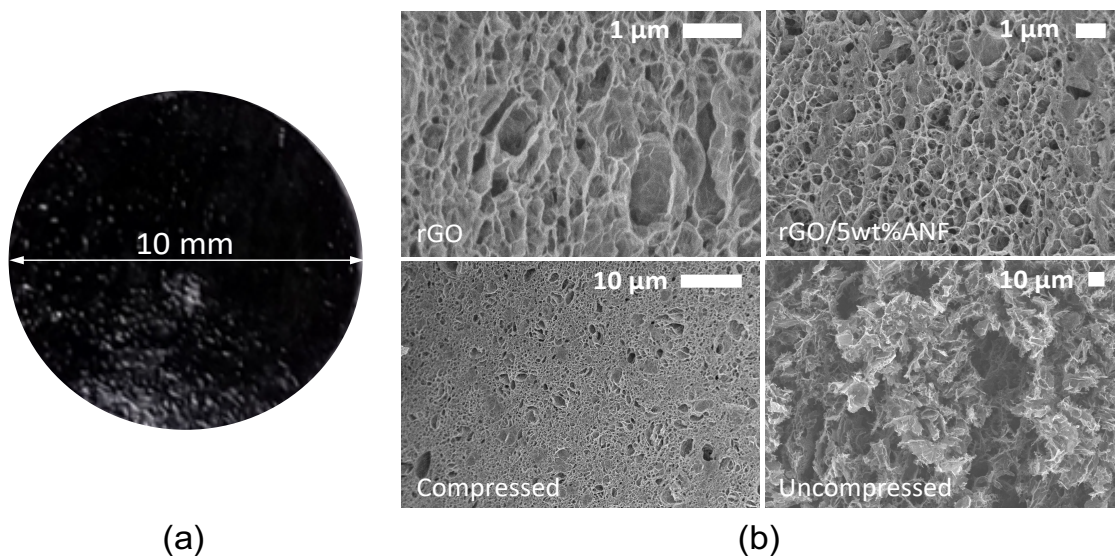


Figure 2.3 (a) Hydrogel rGO/ANF sample, (b) SEM images of different compositions of house of cards with compressed and uncompressed configurations [108].

On the other hand, a porous “house-of-cards” nanoarchitecture can be accessed through the sol-gel method [71][72][73][74]. This method involves cross linking of the functional groups and aerogel-appropriate drying steps. This results in an electrically conductive porous functionalized graphene sheets skeletal structure and ANFs can be added either prior to gelation or coated through post-processing. The house of cards nanostructure can be noted as randomness of solid network that leads to isotropic properties; however, the house of cards expression emphasizes on the arrangements of rGO/ANF nanosheets which can be different from typical spherical porous media nanocomposites [75][76][76]. The sample and SEM images of house of cards nanoarchitecture is shown in Figure 2.3. The electrodes have thicknesses 1-2 mm. The schematics of sol-gel technique is shown in Figure A.2 and more details of experimental setup is provided in section A.1, Appendix A.

These different fabrication approaches to produce rGO/ANF nanocomposites have introduced nanoscale architectural variations that may affect the mechanical and

electrochemical properties of nanocomposite. These architectures constitute tradeoffs regarding electronic conductivity, electrochemical activity, and mechanical properties. For example, the house of cards network architecture is likely to be more brittle, depending on the network-reinforcing role of guest ANFs in the host rGO structure. In contrast, the network architectures have tunable pore size and better electrochemical properties, with high electrical conductivity, high surface area, and rapid ion transport. In contrast, the paper and Layer-by-Layer films may suffer from ion diffusion limitations and ANF-dominated contact resistance. Layered structure films with ANF spacers may also exhibit enhanced capacitance depending upon nanosheet spacing [15][16][17][18][19][72].

In Chapters 3 and 4, a computational modeling is established to investigate the effect of these nanostructures on composite electrode properties such as ionic diffusivity, porosity and tortuosity and the results are compared and validated with experimental measurements. In Chapter 5, the modeling approach is expanded to further study the electrochemical behavior of the whole cell structural supercapacitor made of rGO/ANF electrodes and the plots of current density, voltage and ionic concentration are investigated.

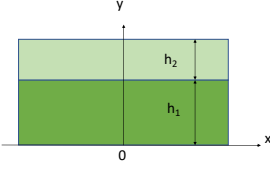
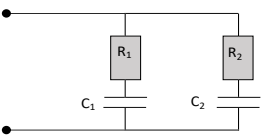
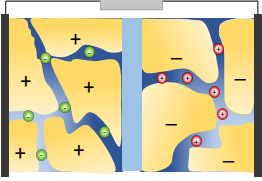
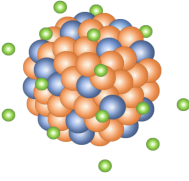
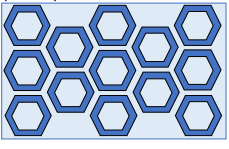
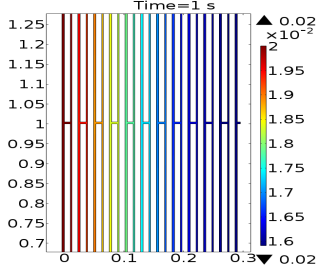
3 The Effect of Electrode Nanoarchitecture on Ionic Diffusivity

3.1 Introduction

Electrochemical and mechanical properties of structural electrodes are highly influenced by material's nanoarchitecture. Specifically, ionic transport in structural electrode is mainly due to diffusion mechanism and an accurate diffusion analysis of structural electrodes is a key to improve design and performance of structural energy storage. In the previously reported studies that have explored various aspects of electrode materials in supercapacitors through computational modeling, generally, the architectural effects were either not considered or fully investigated [78][98]. These studies have mostly focused on the investigation of interfacial side reactions [78], heterogeneous [79], and electrochemical properties of porous electrodes and they often treat electrode material as a porous media and the influence of material architecture on diffusivity is neglected.

In one study, Johnson and Newman [80] developed a model for a porous electrode to analyze the desalting processes in terms of ionic adsorption on porous carbon. In another study, Srinivasan et al. [93] developed an analytical model and used it to study constant-current discharging, cyclic voltage sweeping, and the AC impedance of carbon double-layer capacitors. In most of these studies, the effective diffusion coefficient is assumed to be a constant value or is estimated through Bruggeman's relation, $D_{\text{eff}} = \epsilon D / \tau$ [82][83][92][93]. Modeling material nanoarchitecture is limited to MD simulations [99][100][101][102][103] with restricted conditions or moisture adsorption of composite material [104][105][106]. In Table 3.1 we have summarized several modeling approaches reported in the literature that investigate the ionic diffusivity in composite materials.

Table 3.1 Summary of various modeling approaches to investigate diffusivity [108].

Model	Ref. Study	Advantages	Disadvantages
Analytical Model (Different Fields) 	Li et al. [84] Joliff et al. [85] Yang et al. [86]	Useful to model simple geometries Computationally convenient Describes water diffusion kinetics in some composites	Not accurate for complicated geometries and boundary conditions Requires simplifications Transport limitations due to micropores are ignored
Electrical Model (Supercapacitors) 	Yu et al. [87] Kahlert et al. [88] Kim et al. [89], Buller et al. [90]	Characterizes supercapacitor capacitance and diffusivity Combines the charge-transfer resistance and the diffusion impedance Describe self-discharge due to Investigates diffusion	Large variations in the reported values of diffusion coefficient Uncertainties in the experimental determination of the parameters Electrode material's Architecture is not considered
Porous Media Model (Supercapacitors) 	Lin et al. [91], Verbrugge et al. [92] Srinivasan et al. [93], Kim et al. [94] Zhang et al. [96]	Effective diffusivity is calculated by $D_{eff} = \epsilon D / \tau$ Investigates the effect of thickness and pore size Relatively simple model	Transport properties are determined based on the solvent velocity Materials are assumed to be homogenous with uniformly distributed pores Only the effect of electrode thickness can be investigated
Molecular Dynamics (Supercapacitors) 	Kondrat et al. [99] Shim et al. [100], Pean et al. [101] Youngs et al. [102], Merlet et al. [103]	Shows the dependency of diffusion coefficient on potential inside of the pores Investigates the material properties in molecular level Characterizes diffusion coefficient by ion confinement and electrosorption effects	Limited to the nanoporous materials Variations of diffusion coefficient are observed Computationally expensive; experimental validation is required
Architecture Model (Composite Materials) 	Tang et al. [104], Cussler et al. [105] Korkees et al. [106], Zid et al. [107]	Considers the effect of composite architecture on water absorption, diffusivity, permeability, etc. Predicts the variation of material properties with the concentration	Requires simplifications due to geometrical complexities The morphology of materials is usually more complicated in reality
Architecture Model (Supercapacitors) 	This Study [108]	Shows dependency of diffusion coefficient on the detailed nano- and microstructures Enables a more effective design of electrode architectures	Computationally time consuming relative to porous media modeling Can involve simplifications

To investigate the effect of electrode nanostructure on ionic diffusivity, Zhang et al. [96] have developed a 3D mathematical model for CNT/PPy composite considering electrode surface as macroporous, nanoporous and planar films. It is concluded that macroporous structure has better performance for ionic transportation. In another study, Kaus et al. [97] have introduced a complex electrical model that can predict the effect of charge duration, initial voltage and temperature on open circuit voltage decay. They have shown that the potential decay in supercapacitors is moderately related to the redistribution of ions and ionic diffusion plays significant role in supercapacitors performance. In this study, we have focused on “layer-by-layer” and “brick and mortar” architectures of rGO with 25wt%ANF composite that is reported as a promising candidate for structural electrodes [15][16] obtained through vacuum filtration technique.

3.2 Geometry Development

The schematics of the layer-by-layer architecture influenced by SEM images are shown in Figure 3.1.

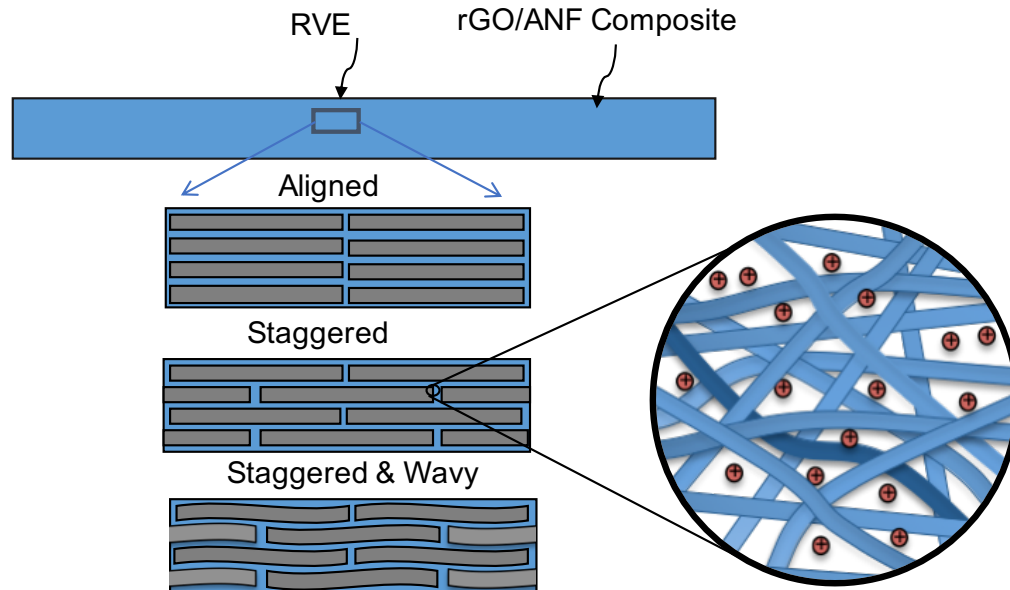


Figure 3.1 Aligned and staggered arrangements of rGO nanosheets (flat and wavy) describing layered nanostructure [108].

To develop a repeating unit cell based on the SEM images of rGO/25wt%ANF composites, it is assumed that rGO nanosheets are building blocks of unit cells that are surrounded by the ANF polymer matrix in two different arrangements: aligned and staggered. We have developed 2D geometries in COMSOL Multiphysics for these arrangements and also considered the rGO nanosheets' waviness adding more complex and realistic features of rGO nanosheets. The waviness of rGO sheets is defined based on the sine wave characteristics.

To define the waviness of rGO nanosheet, it is crucial to use the parallel curve equations instead of using the translational movement of the sine wave [109][110][111][112][113]. The main reason is by changing the waviness of the sheets, the area between the two curves representing the thickness of rGO sheets will not be conserved and will decrease by increasing the waviness. The parallel of a sine curve can be defined as the envelope of circles whose centers are on the curve and their radius defined the offset from the base sine curve, alternatively [110][111][112].

Figure 3.2a shows the sine wave and its parallel curve that are compared to the transitional sine function with an offset d . Here, the area between two curves equals to the area between two flat rGO sheets. The area between two curves reduces if we use the transitional curve. The geometry developed in COMSOL for waviness of one rGO nanosheet is also shown in Figure 3.2b. A constant offset of $0.01\mu\text{m}$ normal to the base curve is assumed for the thickness of each rGO nanosheet. The parametric representations of a vertical sine curve are defined as [110]

$$x = asiny \Rightarrow \begin{cases} y_1(t) = b t, \\ x_1(t) = a \sin t, \end{cases} \quad (3.1)$$

where $a = \pi b / c$. The parallel parametric formula of sine wave in the horizontal direction with a positive offset d is [111][112]

$$y_2(t) = y_1(t) - d \left(\frac{x'(t)}{\sqrt{y'(t)^2 + x'(t)^2}} \right), \quad (3.2)$$

which leads to the following expression

$$y_2(t) = b t - d \left(\frac{\frac{\pi}{c} \cos(t)}{\sqrt{1 + \left(\frac{\pi}{c}\right)^2 \cos^2(t)}} \right). \quad (3.3)$$

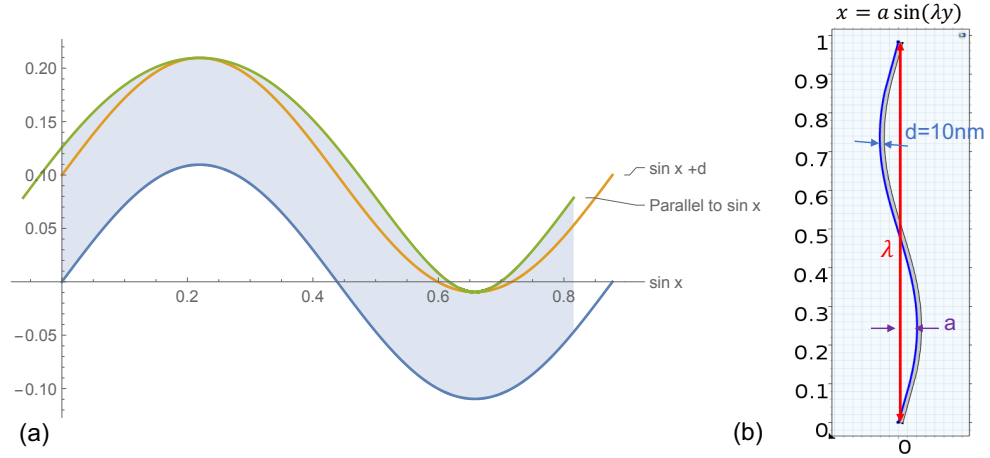


Figure 3.2 (a) Characterizing waviness (w) based on parallel sine curves, (b) geometry development for one rGO sheet in COMSOL [108].

The parallel parametric formula for sine wave in the vertical direction can be determined through

$$x_2(t) = x_1(t) + d \left(\frac{y'(t)}{\sqrt{y'(t)^2 + x'(t)^2}} \right), \quad (3.4)$$

that give us the following expression

$$y_2(t) = \frac{b \pi}{c} \sin(t) + d \left(\frac{1}{\sqrt{1 + \left(\frac{\pi}{c}\right)^2 \cos^2(t)}} \right), \quad (3.5)$$

here b can be evaluated based on the equation

$$b = \frac{1}{\left(4\sqrt{1 + \left(\frac{\pi}{c}\right)^2}\right) E\left(\frac{\pi}{2}, \frac{\pi^2}{\pi^2 + c^2}\right)}, \quad (3.6)$$

where E is the second kind Elliptic Integral. Although the sine wave is a smooth curve, its offset has more complicated mathematical structure[112][113]. The required parameters to determine the waviness of rGO sheets are $\lambda=2\pi b$ in the original sine wave defined as $x=a \sin(\lambda y)$ and the parameter c in $a=\pi b/c$ that is set to $\{8, 12, 16, 20\}$ to achieve waviness of $w = \frac{a}{\lambda} = \frac{1}{2c} : \left\{\frac{1}{16}, \frac{1}{24}, \frac{1}{32}, \frac{1}{20}\right\}$ and zero for straight sheets with zero waviness. Figure 3.3 indicates the representative volume of the nanocomposites with waviness assigned waviness.

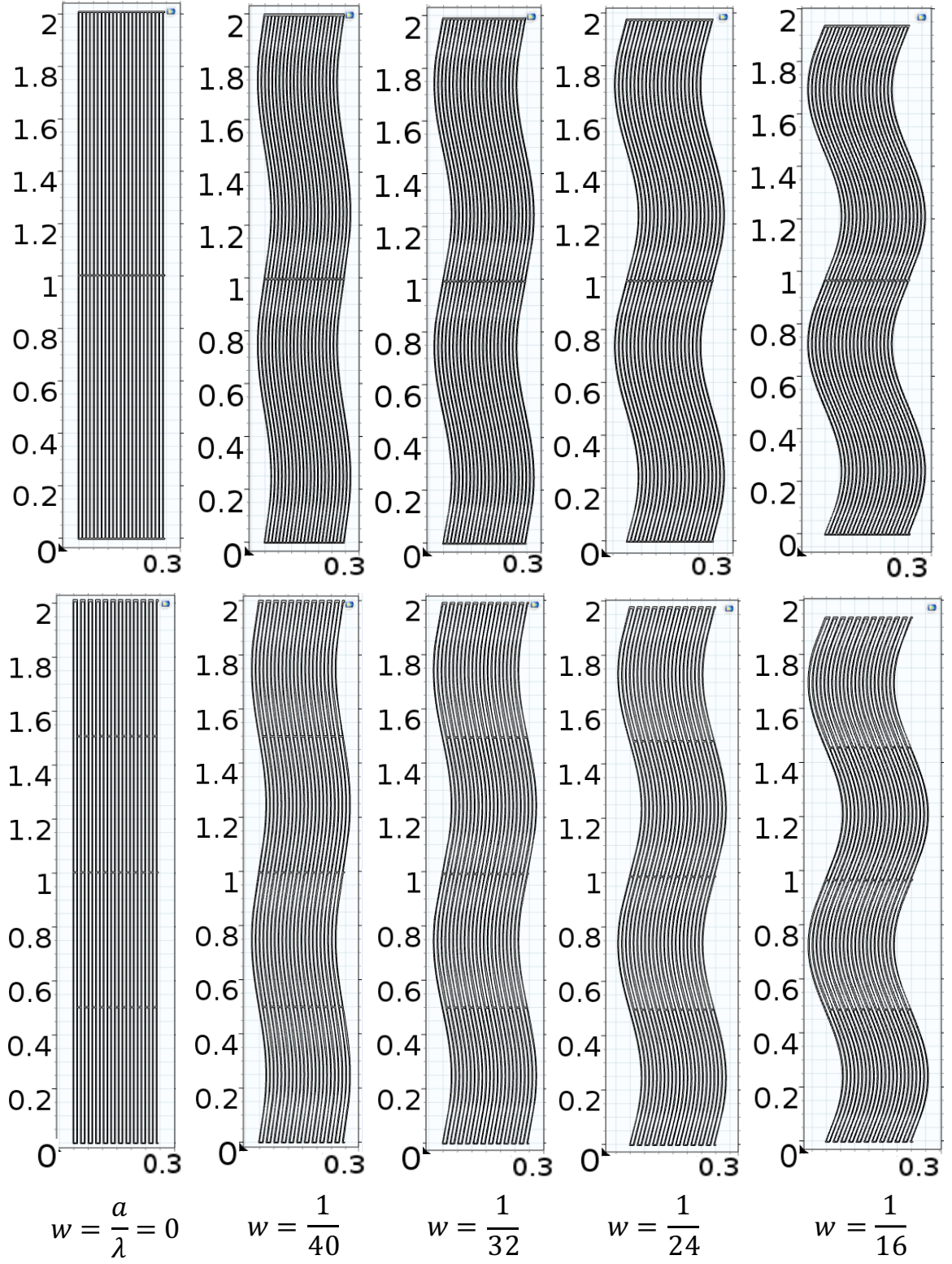


Figure 3.3 Developed geometries for nanocomposite representative volume considering different rGO nanosheets waviness [108].

3.3 Ionic Transfer in Electrode Material

3.3.1 Mathematical Description

We have adopted the dilute-solution theory [114][115] to describe the ionic transport phenomena. The electrolyte is assumed to be a binary solution (1:1 electrolyte) which is a solution of a single salt composed of one type of cation and one type of anion. The dilute-solution theory for binary electrolytes is equivalent to concentrated-solution theory and each species diffuses independently according to its own concentration gradient and diffusion coefficient [114]. The multicomponent diffusion equation can be simplified when the concentration dependence of the physiochemical parameters is not known or can be neglected. In the dilute solution theory, the flux density J_i ($\text{mol m}^{-2} \text{s}^{-1}$) of a solute species i can be described as a combination of mobile ionic species movement via three different phenomena: (i) diffusion flux (due to concentration gradient), (ii) migration flux (due to potential gradient) and (iii) convection flux (due to density gradient) and it is governed by Nernst-Planck equation as [114][115]

$$J_i = -D_i \nabla c_i - z_i F \frac{D_i}{RT} c_i \nabla \Phi + v c_i, \quad (3.7)$$

where c_i , D_i , and z_i are concentration (mol/m^3), diffusivity (m^2/s), and charge number of species i , respectively. The gas constant and temperature are represented by R and T , respectively. Here, the diffusion coefficient is assumed to be constant. In this equation, Φ is the electrostatic potential (V), F is Faraday's constant ($96,487 \text{ C/mol}$), and v is the velocity of the bulk fluid (m/s) [115][116]. When the flux density is inserted into the material-balance equation, it is useful to determine the concentration distribution throughout the medium as [114][115][116]

$$\frac{\partial c_i}{\partial t} = D_i \nabla^2 c_i + z_i F \nabla \cdot \left(\frac{D_i}{RT} c_i \nabla \Phi \right) - v \cdot \nabla c_i + R_i, \quad (3.8)$$

here, R_i is the homogeneous chemical reactions in the bulk of the electrolyte solution. In electrochemical systems, the reactions are limited to the electrode-electrolyte interface and in the case of supercapacitors which there is no faradic reaction, R_i is zero.

In studies of electrode kinetics, further simplification of the domain equation is required. Many previous studies have reported to dismiss the effect of migration in the presence of supporting (inert) electrolyte that reduces the electric field close to the electrode surface [114][115][116]. Supporting electrolytes in the electrochemical cells increases the electrolyte conductivity and reduces the effect of electric field as shown in Figures 3.4 [114][115][116].

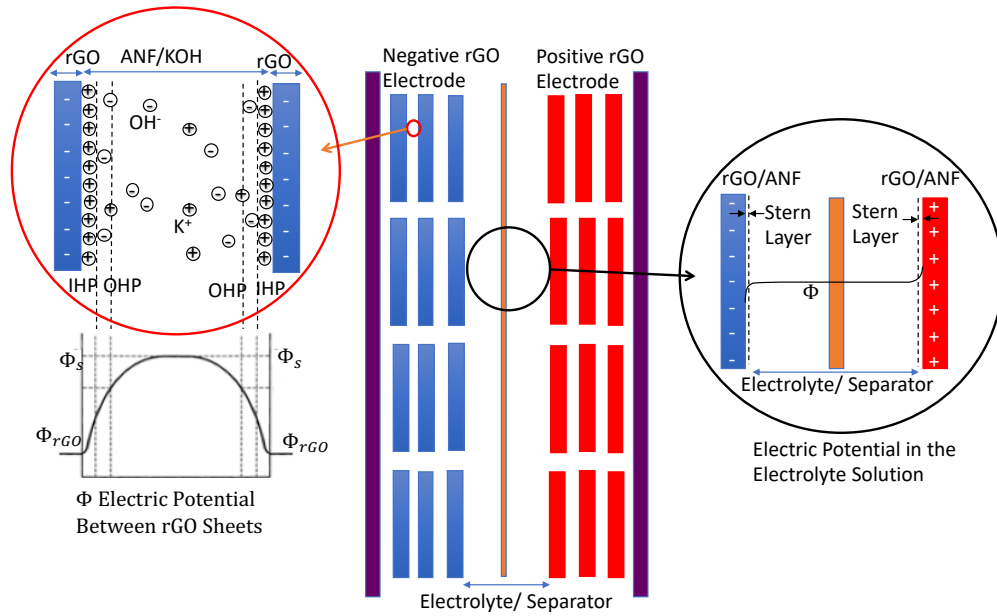


Figure 3.4 Electric potential in electrolyte solution between rGO/ANF nanosheets [108].

The mass transfer of species i then will be primarily due to diffusion and convection and the concentration distribution is governed by diffusion-convection equation as [114]

$$\frac{\partial c}{\partial t} = D \nabla^2 c - \mathbf{v} \cdot \nabla c, \quad (3.9)$$

where the diffusion coefficient D is compromise between the diffusion coefficient of the cation (D_+) and anion (D_-) and can be determined by the following equation [114][115] [116] for a binary electrolyte when $z_+ = -z_- = 1$ as

$$D = \frac{z_+ u_+ D_- - z_- u_- D_+}{z_+ u_+ - z_- u_-}. \quad (3.10)$$

By assuming that the supercapacitor system is under quiescent conditions (stagnant solution) or is unstirred with no density gradients the velocity, v equals to zero and hence convection flux would be zero. By employing these assumptions, the mass transfer equation will be truncated to the diffusion equation that is governed by Fick's second law as [117]

$$\frac{\partial c}{\partial t} = D \nabla^2 c. \quad (3.11)$$

At the electrode surface the diffusion is primary importance to the transport process [115]. At the electrode-electrolyte interface, the concentration of species i differs significantly from its bulk value. This permits a further simplification in the analysis of boundary conditions which is explained in the next section.

3.3.2 Boundary Conditions and 1D vs. 2D Diffusion Mass Transfer

The focus of this study is mainly on the effect of electrode nanoarchitecture on the ionic mass transfer. At the surface of the electrode in contact with electrolyte ($x=0$) it is assumed that the concentration of species i , has the maximum value of c_0 , see Figure A.3 in Appendix A. To satisfy the dilute solution theory, c_0 is set to be a small value of 0.02 mol/m³, while

$$c(0, t) = c_0, \quad \text{at } t \geq 0, \quad (3.12)$$

and the net flux density is assumed to be zero at the other boundaries including top, bottom, and $x = L$ of the representative volume element as well as on the surfaces of rGO blocks

$$-n \cdot \left[-D \left(\frac{\partial c_i}{\partial x} + \frac{\partial c_i}{\partial y} \right) \right] = 0. \quad (3.13)$$

This assumption for RVE is valid since the actual rGO/ANF sample exhibits as a thin film. Therefore, because of the large electrode diameter to thickness ratio, the majority of ions diffuse mainly through the surface of the sample and not through the edges. Therefore, diffusion mass transfer is assumed to be mainly one-dimensional and in x-direction (and zero in y-direction), see Figure A.4 in Appendix A. The rGO nanosheets are assumed to be impenetrable, impermeable, and transversely isotropic. The diffusion coefficient of rGO is orientation dependent and the sheets are presumed to be perpendicular to the electrolyte flow and the ion insertion occurs through the small subgrains in the rGO sheets. On the other hand, ions diffuse through tangled fibers of ANF polymer matrix. Determination of the effective diffusion coefficient for parallel-series laminates in heterogeneous composite materials has been studied in references [117][118] and are shown in Figure A.5.

3.4 Results and Discussion

3.4.1 Concentration Contour Plots

The concentration contour plots are obtained for all architectures and arrangements and a range of diffusion coefficients from 10^{-20} to 10^{-6} m²/s. Concentration contour plots of diffusion coefficient of 10^{-10} m²/s for both aligned and staggered arrangements are shown in Figure 3.5. The rGO sheet waviness is also considered for a/λ ratio of 1/16, 1/24, 1/32 and straight sheets. Figure A.6 in Appendix A shows the entire RVE for each geometry. The time needed for ions to move through the aligned arrangements is around 0.15s that is one order of magnitude faster than time required for ions to move in staggered arrangements that is 3s. The staggered arrangement geometries have more tortuous

pathways result in more complex passages for ionic movement. Therefore, the ionic transfer in staggered arrangement reaches the equilibrium condition taking more time than in aligned arrangements. On the other hand, the aligned arrangements have shorter pathways through electrode thickness, which lead to faster ionic movements towards the equilibrium concentration. The details related to these plots will be quantitatively explained in the following sections.

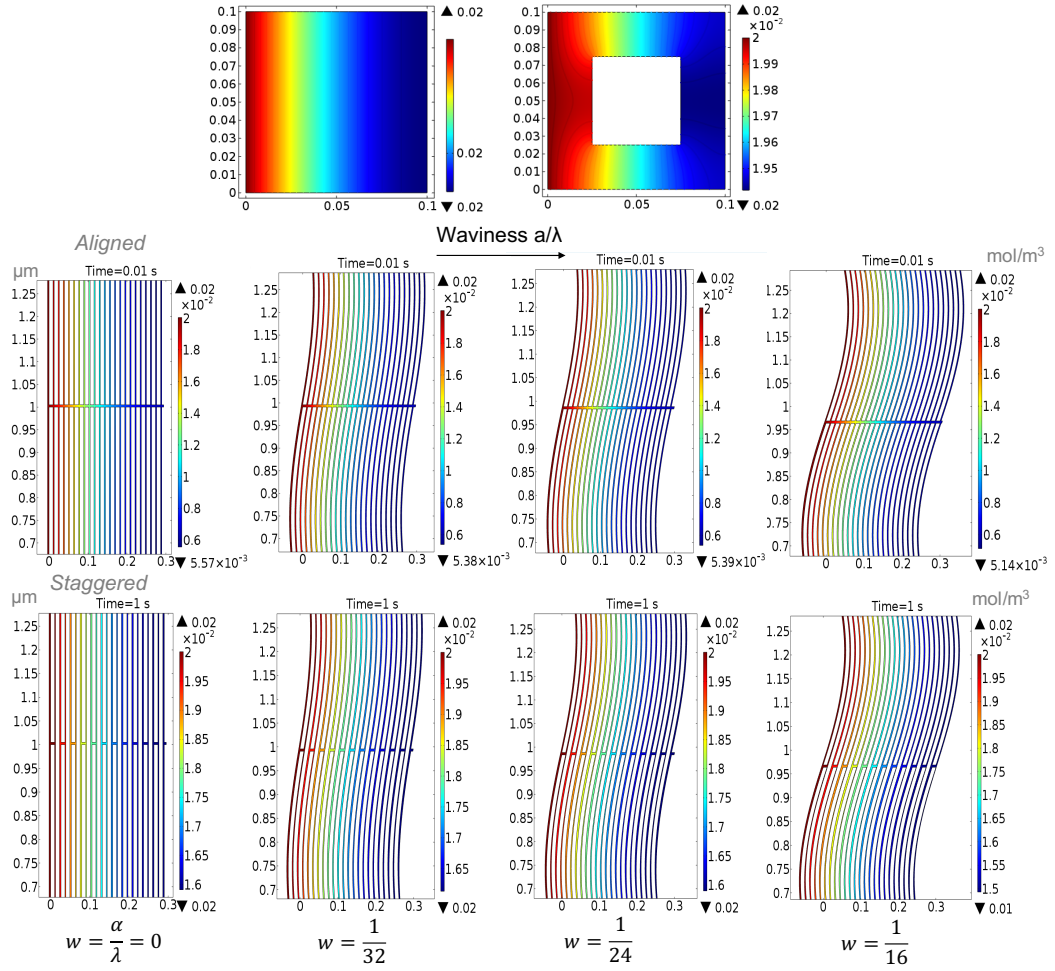


Figure 3.5 Concentration contour plots, $D=10^{-10} \text{ m}^2/\text{s}$ [108].

3.4.2 Concentration-Time Curves

The concentration-time plot of three points located in the left, middle, and right of the RVE thickness is shown in Figure 3.6. It can be seen that how the ionic transfer

develops in three stages. The stage (1) is the time needed for ions to reach the points. It is obvious that the longer time is required for ions to move towards the point selected far from the diffusion boundary. The stage (2) is the transient stage, in which the ion transfer continues regarding to the concentration equilibrium. Finally, when the ionic concentration reaches the maximum concentration, diffusion goes to the steady state condition in stage (3). The concentration-time plots for all the arrangements are illustrated in Figure A.7 in the Appendix A. It can be seen that if diffusivity is enhanced, it will directly improve capacitance, energy and power of the supercapacitors referring to the equations sections A.2 to A.3 in the Appendix A [78][79][81][83][114][115][116].

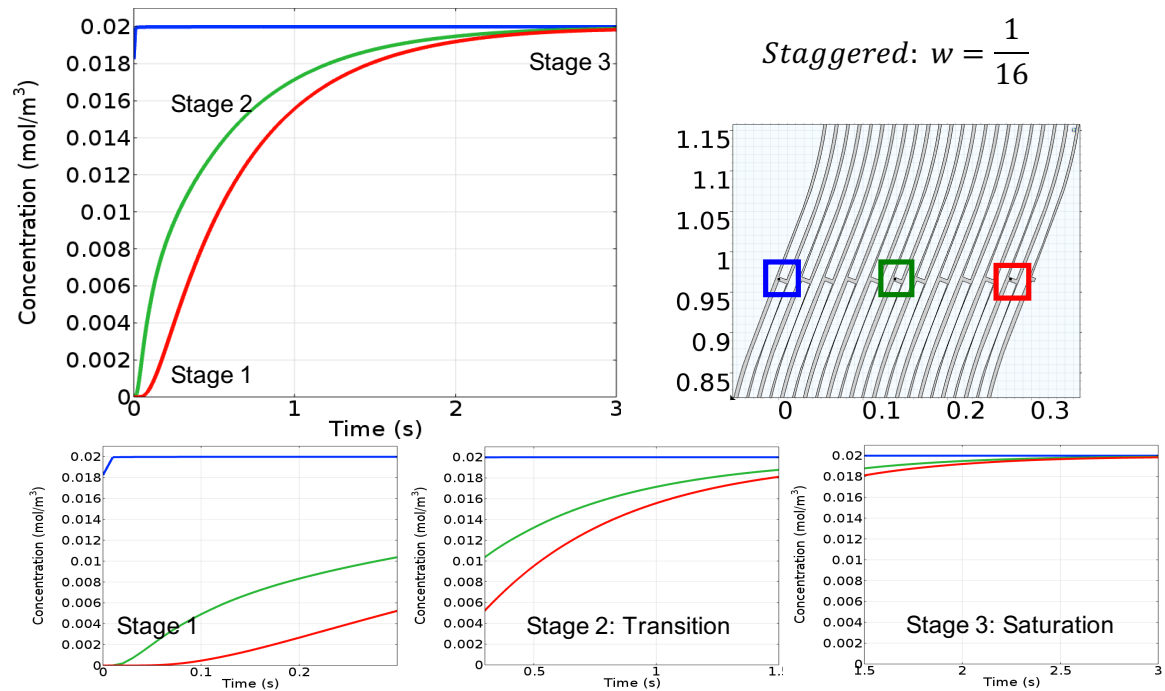


Figure 3.6 Concentration-time plots for three points shown in the staggered arrangement indicating three-time stages of diffusion development: (1) linear area, (2) transition area, and (3) saturated area [108].

3.4.3 Concentration-Distance Plots

Figure 3.7 shows different time steps of concentration development along the vertical red line in the staggered arrangement for diffusion coefficient of $10^{-10} \text{ m}^2/\text{s}$. The

sharp point in the middle of the plot is resulted from ion movement through the channel between rGO sheets. The flux streamlines shown in Figure 3.7 in the right can visualize this effect. It can be seen that the density of streamlines is higher in the middle of the channel rather than in contact with the rGO surfaces. Then ions confront lower resistance in the center of the channel and the velocity of ions in contact with the rGO surface is zero. In the absence of this channel, for 1D and a simple 2D block, a smooth curvature for concentration have been obtained.

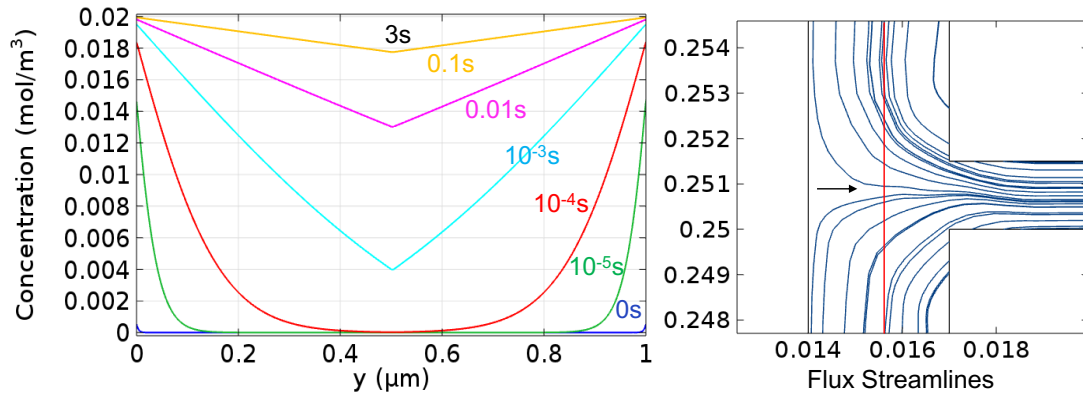


Figure 3.7 Ionic flux streamlines along the red line causes the sharp point in the middle of the concentration-distance plots [108].

3.4.4 The Effect of Diffusion Coefficient on Concentration

To consider a wide range of diffusion coefficients corresponding to various ion types in aqueous and non-aqueous electrolytes, the computation is performed for Fickian diffusion coefficients ranging from 10^{-20} m²/s to 10^{-6} m²/s. The ranges of diffusion coefficients for four common ions Li⁺, Na⁺, K⁺, and Mg²⁺ [119][120][121][122][123][124][125][126][127] in different electrolytes are reported in Table A.1 in the Appendix A. Figure 3.8 shows the effect of diffusion coefficients, from 10^{-9} m²/s to 10^{-6} m²/s, on ionic concentration, shown in 2D and 3D plots. More comparisons of lower diffusion coefficients are reported in Figure A.8. The results indicate that the diffusion coefficients

lower than $10^{-14} \text{ m}^2/\text{s}$ require significant amount of time to reach the steady state condition. Hence, for electrolytes containing ions such as K^+ and Li^+ , with diffusion coefficient of $10^{-9} \text{ m}^2/\text{s}$ and $10^{-10} \text{ m}^2/\text{s}$ respectively, the ionic transport occurs relatively rapidly.

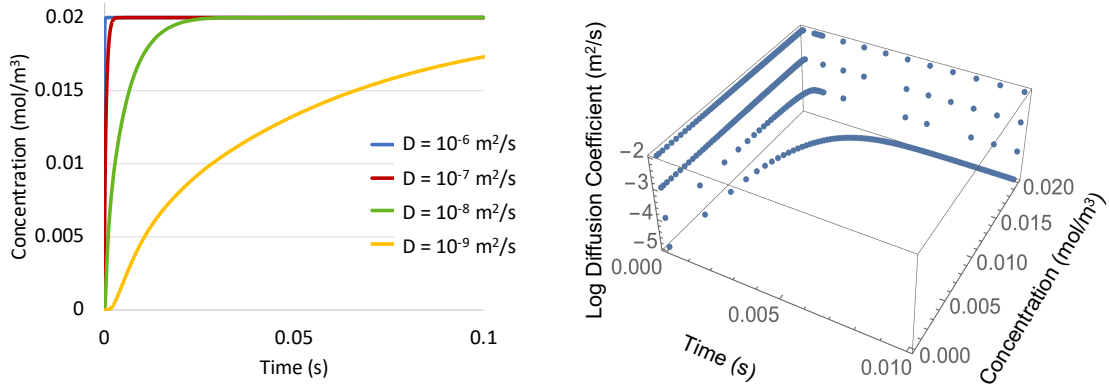


Figure 3.8 The effect of diffusion coefficient on concentration development for staggered arrangement with $w = 1/24$, $D = 10^{-9}$ to $10^{-6} \text{ m}^2/\text{s}$ [108].

3.4.5 The Effect of rGO Sheets Waviness (a/λ) on Ionic Diffusivity

The waviness of rGO sheets characterized as the a/λ ratio in a sine wave for $1/16$, $1/24$, $1/32$, $1/40$ and 0 (straight sheets). Figure 3.9a shows that increasing waviness impedes the ionic diffusivity in both arrangements due to the increasing tortuosity in the structure. Figure A.9 compares the effect of rGO sheets waviness on ionic diffusivity in aligned and staggered arrangements. However, increasing waviness of the rGO sheets in the aligned arrangement does not show a notable effect on the ionic transport. In the aligned arrangement, the ions can move faster along the aligned edges of rGO sheets, leading to minor differences in diffusivity between straight and wavy rGO nanosheets.

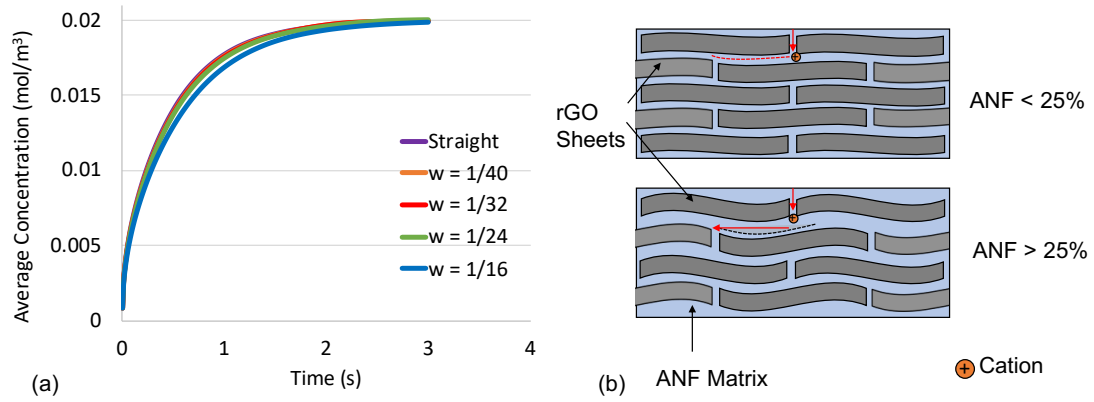


Figure 3.9 (a) The effect of rGO waviness on ionic diffusivity in staggered arrangement, (b) increasing rGO waviness impedes the ionic diffusivity [108].

The waviness causes more tortuous paths between rGO nanosheets in the staggered arrangement, since the ions are traveling along the surface of the wavy rGO, and it leads to slower ionic transport. For a composite with higher percentage of ANF (more than 25%ANF), ionic diffusion can occur faster because there is adequate space between the rGO sheets that facilitates ionic transfer through shorter pathways, see Figure 3.9b. Based on this result, electrode composite material with minimum rGO waviness is preferred.

3.4.6 Effective Diffusivity and Tortuosity

The effective diffusion coefficient for each nanoarchitecture is calculated assuming Fickian diffusivity [128] through

$$D_{\text{eff}} = \pi \left(\frac{kL}{4M_{\text{eq}}} \right)^2, \quad (3.14)$$

where k is the slope of linear segment of the average concentration vs. time^{1/2} plot shown in Figure 3.10 and calculated as [128]

$$k = \frac{M_t}{t^{1/2}}, \quad (3.15)$$

here, D_{eff} is the effective Fickian diffusion coefficient (m²/s), L is the material thickness (μm), M_t is the concentration at time t (mol/m³) and M_{eq} is the equilibrium concentration

for the dilute solution electrolyte. For this calculation, the ionic diffusivity of ANF matrix is varied from 10^{-12} to 10^{-10} m^2/s . The effective diffusivity is observed to decrease about 3 orders of magnitude in aligned and about 4 orders of magnitude in staggered architectures. The effective diffusion coefficient obtained for ionic diffusivity of 10^{-12} , 10^{-11} , and 10^{-10} m^2/s are respectively 10^{-15} , 10^{-14} , and 10^{-13} m^2/s for aligned and 10^{-16} , 10^{-15} , and 10^{-14} m^2/s for staggered arrangements. Experimentally, ionic diffusivity of K^+ in pure ANF matrix is measured to be in range of 10^{-12} - 10^{-11} m^2/s . The effective diffusivity of K^+ in rGO/25wt%ANF measured through cyclic voltammetry (CV) reported in the reference [16] is determined by applying Randles-Sevcik equation in a similar range from 10^{-16} to 10^{-14} m^2/s . This method is explained further in Chapter 4. The results verify that the staggered arrangement model provides a better prediction of the experimental ion diffusivity, due to its more realistic structural complexity compared to the aligned arrangement model.

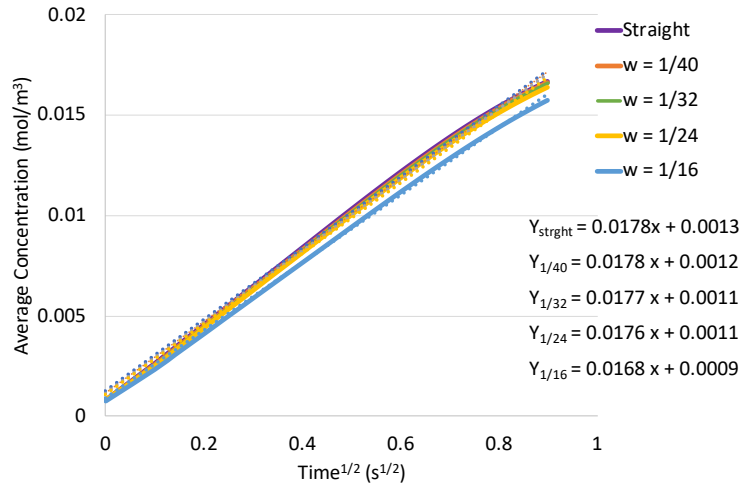


Figure 3.10 Average concentration-time^{1/2} plot ($D = 10^{-10}$ m^2/s) is used to calculate effective diffusivity and tortuosity [108].

For further investigation of structural effect, the average tortuosity of the material architecture has been determined regarding the effective diffusivity D_{eff} as [129]

$$D_{\text{eff}} = \frac{D}{\tau^2}, \quad (3.16)$$

where τ is the tortuosity, and D is the diffusion coefficient set at $10^{-10} \text{ m}^2/\text{s}$. The average tortuosity for the aligned and staggered arrangements is determined to be 329 and 7267, respectively. Table 3.2 reports the effective diffusion coefficient and tortuosity obtained for each arrangement and waviness through nanoarchitecture modeling. The results from this study are not limited to the supercapacitors' electrodes and can be applied to any layered nanostructure composite electrode used in any other energy storage such as Li-ion batteries.

Table 3.2 Simulation results for effective diffusion coefficient and tortuosity [108].

<i>Waviness</i>		<i>1/16</i>	<i>1/24</i>	<i>1/32</i>	<i>1/40</i>	<i>0 - Straight</i>
<i>Aligned</i>	$D_{\text{eff}} (\text{m}^2/\text{s})$	3.02×10^{-13}	3.03×10^{-13}	3.03×10^{-13}	3.04×10^{-13}	3.05×10^{-13}
	Tortuosity	330.7	329.9	329.9	329.1	327.5
<i>Staggered</i>	$D_{\text{eff}} (\text{m}^2/\text{s})$	1.26×10^{-14}	1.39×10^{-14}	1.40×10^{-14}	$1. \times 10^{-14}$	1.42×10^{-14}
	Tortuosity	7910	7208	7126	7047	7047

3.5 Conclusions

Two-dimensional models have been developed to describe the rGO/25%wt ANF composite electrodes with aligned and staggered arrangements of rGO sheets in ANF matrix with various waviness. The results show that the waviness impedes the ionic diffusivity in both arrangements. However, this effect is more significant in staggered arrangements than in aligned arrangements. The effective diffusivity and tortuosity of each arrangement agrees with the experimental measurements.

4 Nanoarchitecture vs. Porous Media Diffusion Models

4.1 Introduction

In Chapter 3, we have discussed that the nanostructure of composite electrodes is often neglected in modeling electrochemical systems due to the complicated geometry development and computational cost. A widely used approach to determine the effective diffusion coefficient of electrode materials is the porous electrode theory. In porous electrode theory, the effective diffusion coefficient is determined through $D_{\text{eff}} = \varepsilon D / \tau$ relation [82][83][92][93][94][95][114][115][116], where the effective diffusion coefficient of the electrode material is related to the molecular diffusion coefficient (D), porosity (ε), and tortuosity (τ) of the material. In this approach tortuosity is related to porosity either through Bruggeman's relation $\tau = \varepsilon^{-1/2}$ [130] or Millington-Quirk's relation $\tau = \varepsilon^{-1/3}$ [131][132].

Although the porous electrode theory provides simplicity in computational analysis, it cannot predict local electric potential distribution and ionic concentration gradients throughout the electrode material. These methods do not provide detailed information about the local concentration distribution of species and usually overestimate the ionic diffusion coefficients. Furthermore, the porous electrode approach predicts the same value of D_{eff} for the composite materials with the same void volume fraction while they may have different pore size distribution, pore connectivity and pore accessibility which may lead to different effective diffusion coefficients and electric conductivities. The porous electrode theory is generally more applicable for low porosity materials that can be treated as a continuum media. In the case of composite electrodes such as rGO/ANF nanocomposites that can be produced through various fabrication methods, a more rigorous

nanostructural modeling is required to capture nanoarchitectural difference within the materials [96][108][133].

Zhang et al. [133] developed multiscale models considering a hierarchical porous material to investigate effective ionic diffusivity and estimated the voltage response of the electric double-layer capacitors to charging based on microscopic properties such as pore size and pore connectivity. They concluded that the reliance on Bruggeman's relation significantly underestimates the gradients of both ion concentration and electric potential within the EDLC. In another study [134], they expressed the anisotropic diffusion coefficient and adsorption coefficient in terms of the pore radius and inter-pore throat width and connectivity in nanoporous materials.

In this chapter, we continue a similar modeling approach as Chapter 3, for rGO/ANF composite electrode including the house of cards nanoarchitecture. The results obtained from nanoarchitectural modeling of both house of cards and layered are compared with the porous media approach and also validated with experimental measurements. Our goal is to provide a model that captures the nanoarchitectural characteristics of materials and offers better estimations of the effective diffusion coefficient, local electric potential and concentration distributions.

4.2 Digital Image Processing

Scanning electron microscopy (SEM) provides very useful information through a direct observation of the material's structure. The SEM images of rGO/ANF composite electrodes indicate that the rGO/ANF nanosheets are randomly oriented at various angles in the house of cards structure Figure 4.1a, while in the layered structure, the paper-like rGO/ANF sheets are stacked on top each other, Figure 4.1b.

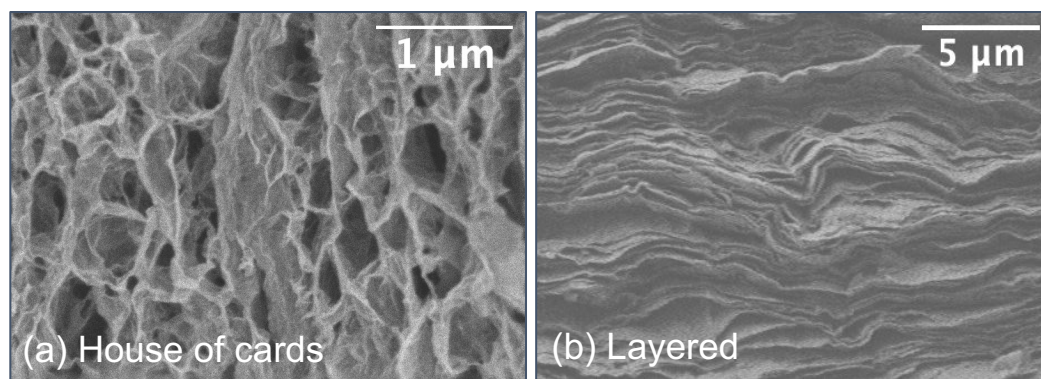


Figure 4.1 SEM Images of rGO/5%wt ANF nanocomposites through different fabrication methods [135].

Here, the digital image processing method (DIP) is used to determine the average porosity, pore size distribution, and the length and thickness of rGO/ANF nanosheets to design unit cells representing the nanoarchitectures of hydrogel and layered nanocomposites. The public domain image processing program ImageJ (developed by the National Institute of Health, USA, Division of Computer Research and Technology) as well as the Scanning Probe Image Processing (SPIP) Metrology software are utilized to treat and analyze the nanocomposite SEM images [136][137][138][139]. Indeed, each software for image processing has its own features, but in general image processing follows the same steps to provide statistical information about the images. These steps are as follow:

- (1) Select and open the SEM image in the software. The opened image size appears in pixels.
- (2) Adjust the scale of the image based on the scale bar provided on the SEM image and select the region of interest for analysis.
- (3) Adjust a threshold to binarize the image and distinguish the voids and materials in the image; the dark background shows the void area, while the material part appears in white.

- (4) The auto setting can be selected, or the sliders can be manually moved until all the interested areas are selected. Usually a histogram is displayed to provide assistance.
- (5) In “analyze and set measurements” sections, the parameters are specified to be measured.
- (6) The results tables and histogram plots will appear for further statistical analysis.

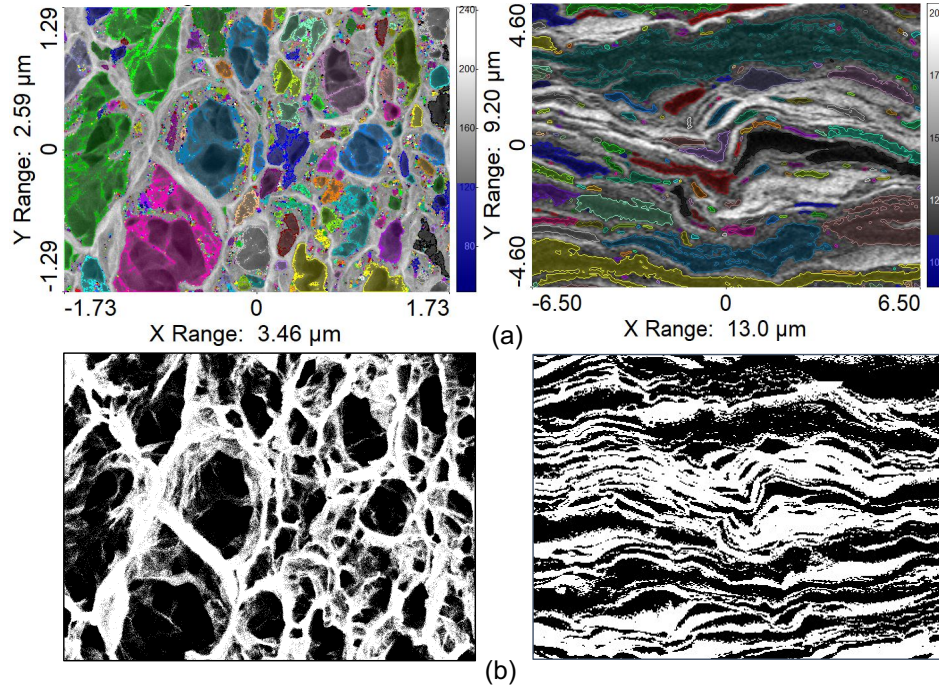


Figure 4.2 Threshold applied to SEM images of house of cards and layered nanostructures, (a) Scanning Probe Image Processing software, and (b) ImageJ software [135].

Figure 4.2 compares the applied threshold on SEM images utilizing ImageJ and SPIP software. The threshold is selected to assure all the voids are covered in black or colored area. A very close estimation of porosity is obtained for each image through both software. The statistical analysis to determine the average void volume fraction (average porosity) are summarized in Tables 4.1. Also, the histogram plot of the average pore area distributions for one the house of cards samples is reported in Figure 4.3. The average void per volume (porosity) is estimated to be 51.45% for house of cards and 41.56% for layered structure.

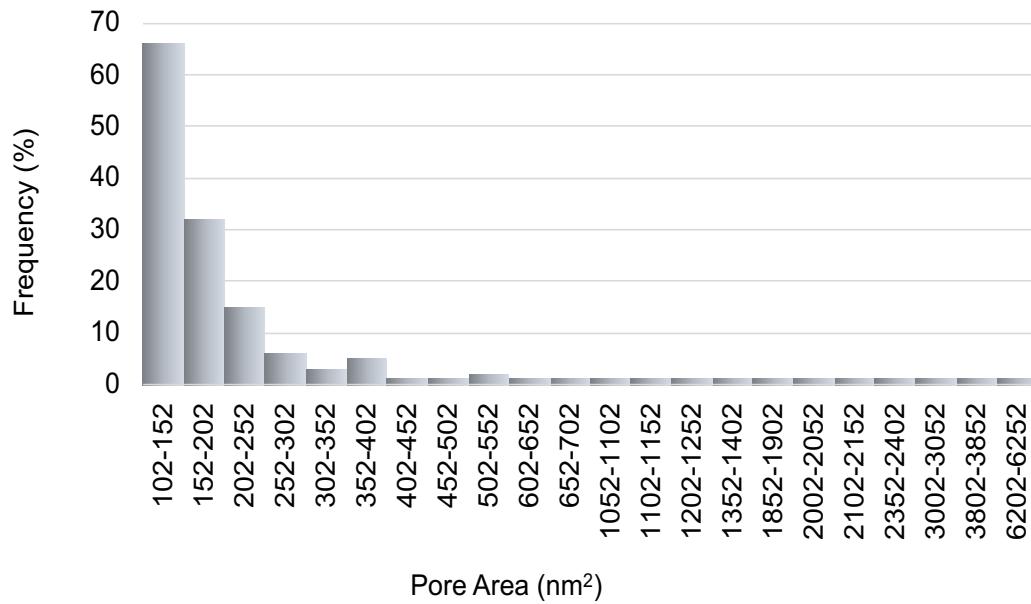


Figure 4.3 Pore area distribution for one SEM image of rGO/ANF sample [135].

Table 4.1 Summary of SEM image processing for porosity measurement [135].

Nanoarchitecture	House of Cards	Layered
Number of SEM images	12	7
Average number of pores	12444	402
Average pore size (nm ²)	447.81	317.86
Standard Deviation	190	150
Average porosity%	51.45	41.56

In nanoarchitecture modeling, the material is assumed to be made of uniform unit cells that are the representatives of the nanostructure. To design these unit cells the average length and thickness of rGO/ANF nanosheets are estimated through various measurements in the SEM images. The average length and thickness of nanosheets are determined to be around $L=500$ nm and $\lambda=90$ nm, respectively, as shown in Figure 4.4. The statistical analysis of length and thickness of rGO/ANF nanosheet are summarize Table 4.2.

Table 4.2 Summary of SEM image processing to estimate length and thickness [135].

Parameter	Length	Thickness
Number of SEM images	7	7
Number of measurements	200	200
Average Value (nm)	499.8	90.5
Standard Deviation	3.06	3.54

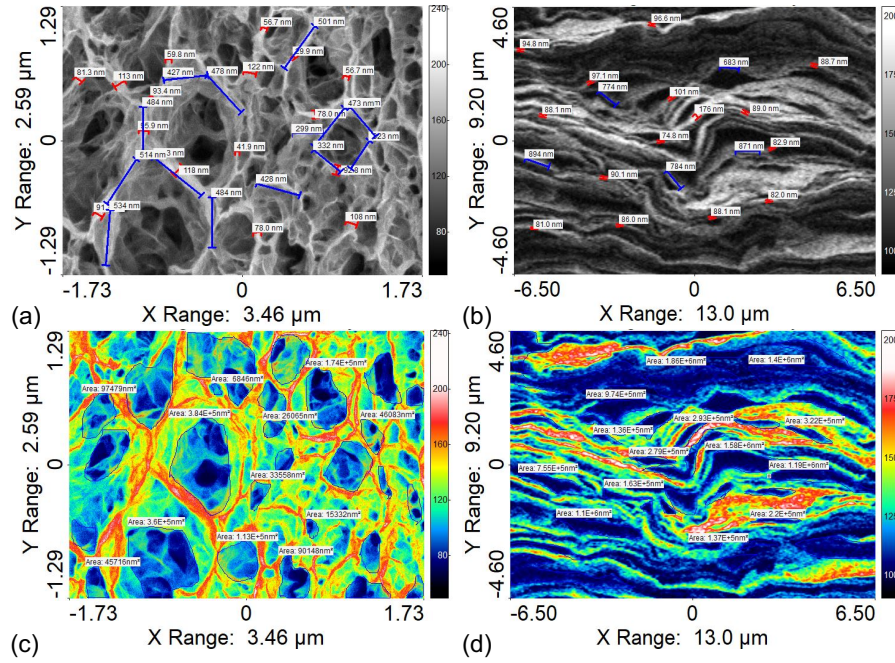


Figure 4.4 Image processing method to estimate (a),(b) the length and thickness of rGO/ANF nanosheets, (c),(d) the void fraction volume of nanocomposites for house of cards and layered structure, respectively [135].

Figure 4.5 shows the histogram plots of the average thickness and length distribution of rGO/ANF nanosheets as well as the average porosity distribution for each nanoarchitecture.

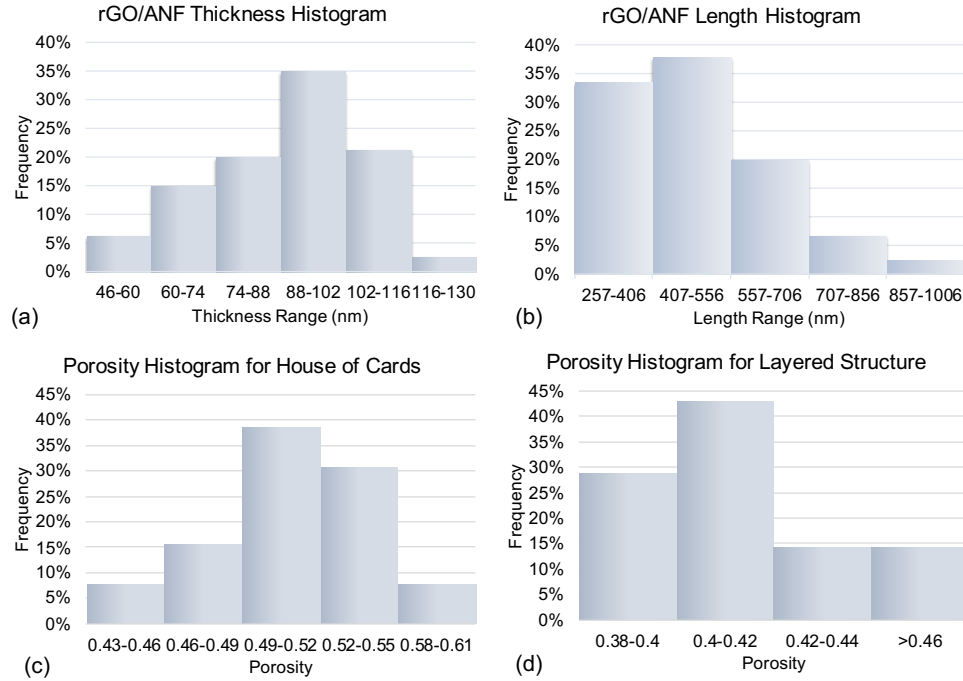


Figure 4.5 (a) average thickness distribution, (b) average length distribution of rGO/ANF nanosheets, (c), and (d) average porosity distribution for house of cards and layered nanocomposites, respectively [135].

4.3 Nanoarchitecture Based Computational Modeling

We have developed two nanoarchitectures for rGO/ANF electrode materials based on SEM images and digital image processing method. The information obtained from image processing are used to develop a representative volume element (RVE) for each architecture. In this study, it is assumed that ANF nanofibers are blended with rGO nanosheets. The rGO/ANF nanosheets are treated as impermeable building blocks of a repeating unit cell, arranged in square configuration for house of cards and staggered configuration for the layered structure as indicated in Figure 4.6. The distance between rGO/ANF nanosheets satisfies the void volume fraction of each architecture determined from digital image processing method. The electrolyte used in this simulation is monovalent binary electrolyte potassium hydroxide (KOH) solution which is also used in experimental measurements.

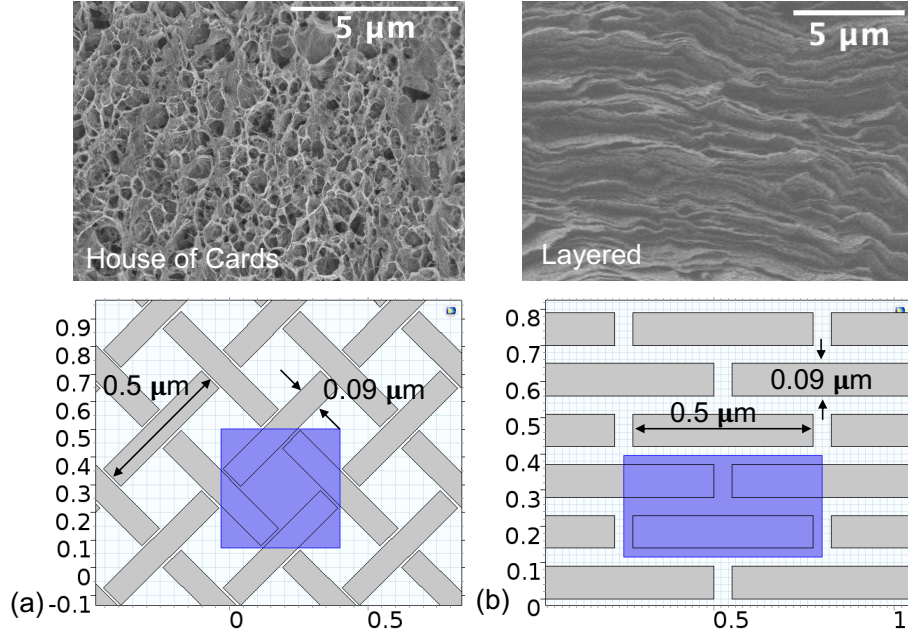


Figure 4.6 Unit cell development for (a) house of cards, (b) layered nanostructure based on SEM images; The rGO/ANF nanosheets, represented by gray rectangles as building blocks of each unit cell, are arranged in square and staggered configurations to describe house of cards and layered nanostructures, respectively [135].

4.4 Governing Equations

In a binary electrolyte such as KOH solution, the dilute-solution theory is equivalent to the concentrated-solution theory. In the absence of homogenous chemical reactions which is valid for electric double-layer capacitors, the flux of species i in the electrolyte follows the Nernst-Plank equation as [114][115][116]

$$J_i = -D_i \nabla c_i - D_i c_i \frac{z_i F}{RT} \nabla \Phi. \quad (4.1)$$

According to this equation, the mass conservation of ions depends on diffusion and migration phenomena. For stagnant condition where the density gradient is zero, the main equation would be [114][115][116]

$$\frac{\partial c_i}{\partial t} = \nabla \cdot \left[D_i \left(\nabla c_i + c_i \frac{z_i F}{RT} \nabla \Phi \right) \right], \quad (4.2)$$

where c_i (mol/m³) is the concentration of species i in the electrolyte. $\Phi(x, t)$ is the electric potential (V) and D_i is the diffusion coefficient (m²/s) of species i . Here, z_i is the number of charge and R , T and F are gas constant (J mol⁻¹ K⁻¹), room temperature (K) and Faraday's constant (C/mol), respectively. The Gouy-Chapman-Stern (GCS) theory is adopted to describe the electric double-layer close to the electrode-electrolyte surface. The Gouy-Chapman theory suggests that the electric potential $\Phi(x, t)$ in the diffuse layer is related to the total ionic charge density through Poisson equation (Gauss's Law) as [114][115]

$$\nabla^2 \Phi = -\frac{F}{\epsilon} (z_+ c_+ + z_- c_-), \quad (4.3)$$

where, ϵ (F/m) is the electrolyte permittivity or dielectric constant. The electric field inside the outer Helmholtz plane (OHP) follows the Stern's theory and since the charge density at any point from electrode surface to the OHP is zero the potential profile in the compact layer is linear. The thickness of the Stern layer is assumed to be 0.2 nm which is a typical diameter of an ion. The Gouy-Chapman theory predicts that the characteristic thickness of the diffuse double-layer to be of the same order as the Debye length, λ_D according to [114]

$$\lambda_D = \sqrt{\frac{RT \epsilon_0 \epsilon_r}{2F^2 c_b}}, \quad (4.4)$$

where, ϵ_r is the relative permittivity of KOH (80.5), ϵ_0 is the vacuum permittivity (8.85×10⁻¹² F/m) and c_b is the bulk concentration of the binary solution. To set the electric potential boundary conditions, we assume that the rGO/electrolyte interface carries a constant electric potential Φ_1 as a Dirichlet boundary condition

$$\Phi(x, t) = \Phi_1, \quad (4.5)$$

and due to electroneutrality condition, the bulk electrolyte potential satisfies

$$\nabla^2 \Phi_b = 0, \quad (4.6)$$

and

$$\Phi_b = 0. \quad (4.7)$$

For concentration boundary conditions, the bottom boundary in each unit cell is set to Dirichlet boundary condition equal to the ions bulk concentration

$$c(x, t) = c_{\pm}. \quad (4.8)$$

We assume that the K^+ and OH^- are dissociated equally throughout the electrolyte and also $D_+=D_-$. As it is mentioned before, the rGO/ANF sheets are assumed to be impermeable [133], therefore

$$-n \cdot D_{\pm} \left(\nabla c_{\pm} + c_{\pm} \frac{z_{\pm} F}{RT} \nabla \Phi \right) = 0. \quad (4.9)$$

Finally, to eliminate the net local current source at the electrode/electrolyte interface, it is assumed that the electric double-layer is stably formed and the surface electrosorption reaction has reached the equilibrium and therefore the Robin boundary condition is equal to zero[133][134]

$$-n \cdot D_{\pm} \left(\nabla c_{\pm} + c_{\pm} \frac{z_{\pm} F}{RT} \nabla \Phi \right) = f_{\pm}(c_+, c_-) = 0, \quad (4.10)$$

while the initial conditions are

$$\Phi(x, 0) = 0, \quad (4.11)$$

and

$$c(x, 0) = 0. \quad (4.12)$$

Boundary conditions for both nanoarchitecture unit cell is shown in Figure 4.7. The Poisson-Nernst-Planck equation for concentration and electric potential are solved utilizing COMSOL multiphysics software through coupling *Electrostatic* and *Transport of Dilute Species* physics with applied boundary conditions over each unit cell. The results obtained from simulation are discussed in detail in the results and discussion section.

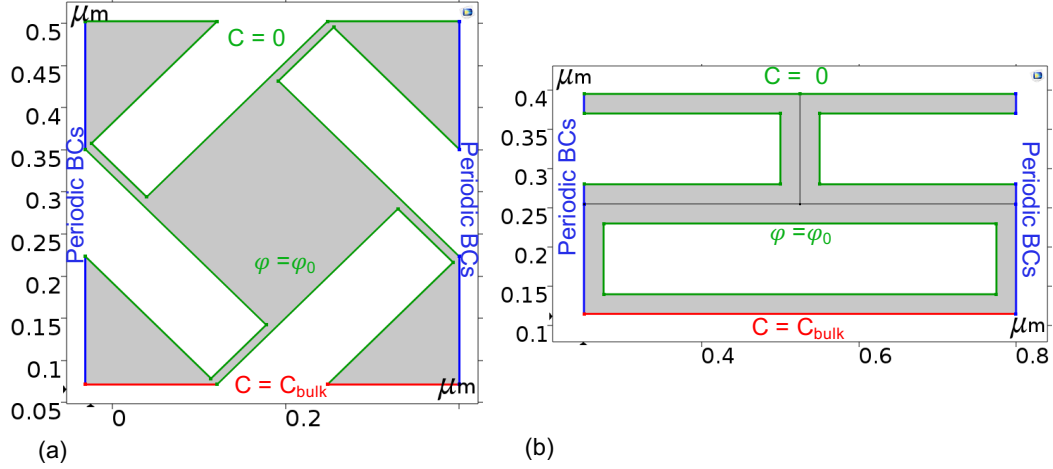


Figure 4.7 Applied boundary conditions in each geometry [135].

4.5 Experimental Section

4.5.1 Diffusion Coefficient Measurement

Electrochemical techniques such as cyclic voltammetry (CV) [140][141] and electrical impedance spectroscopy (EIS) [88][142] are the most common experimental methods to measure diffusion coefficient in an electrochemical system. In this work, the EIS measurement is used to evaluate the effective diffusivity of potassium ions (K^+) in rGO/ANF composite materials with house of cards structures. The cyclic voltammetry measurements reported in references [15][16] are used to measure the effective diffusion coefficient in layered structure rGO/ANF electrodes.

4.5.2 Cyclic Voltammetry

Cyclic voltammetry measurements are performed on the supercapacitors made of two identical rGO/ANF electrodes with layered nanostructure. The voltage window is set from 0 to 1 V and the CV plots are obtained for the scan rate of 20 mV/s for 5 cycles. The effective diffusion coefficient, D (m^2/s) can be calculated through Randles-Sevcik [88] equation, which is the relationship between the peak current, i_p (A) and the square root of scan rate, ν (V/s) obtained from CV plots [140][141] as

$$i_p = 0.4463 zFAc \left(\frac{zFvD}{RT} \right)^{\frac{1}{2}}, \quad (4.13)$$

the parameters z , A , and c are charge number, electrode surface area (m^2), and ionic concentration (mol/m^3), respectively. Also, the constants R , F , and T are universal gas constant ($\text{J}\cdot\text{mol}^{-1}\cdot\text{K}^{-1}$), Faraday's constant (C/mol) and room temperature (K), respectively.

4.5.3 Electrical Impedance Spectroscopy

Electrical impedance spectroscopy is performed on rGO/ANF with house of cards supercapacitor cells with 6M KOH electrolyte. The frequency range is set from 10 mHz to 100 kHz for the AC voltage of 10 mV (rms). The characteristic Nyquist and Bode plots are obtained to estimate the effective diffusion coefficient. The diffusion element on Nyquist plot, also known as Warburg impedance (Ω), appears as a line with the slope of 45° for non-ideal capacitors. The diffusion coefficient of electrode material can be calculated using [88][142]

$$\sigma = \frac{RT}{z^2 F^2 A \sqrt{2}} \left(\frac{1}{c D^{1/2}} \right), \quad (4.14)$$

the Warburg coefficient, σ ($\Omega \cdot \text{s}^{1/2}$) can be calculated as the slope of low frequency real impedance (Z_{real}) vs. $\omega^{-1/2}$ plot, where ω is the angular frequency $2\pi f$ (rad/s) with f as frequency as [142]

$$Z = \sigma (\omega)^{-1/2} (1 - j). \quad (4.15)$$

4.6 Results and Discussion

Figure 4.8 indicates the concentration profile of K^+ ions and the electric potential development at time = 0.01s and 0.05s in the layered and house of cards nanostructure, respectively. It can be seen that concentration of K^+ ions in the staggered arrangement

reaches the equilibrium faster than house of cards unit cell. The concentration contour plots for OH^- are also shown in Figure B.1 in the Appendix B.

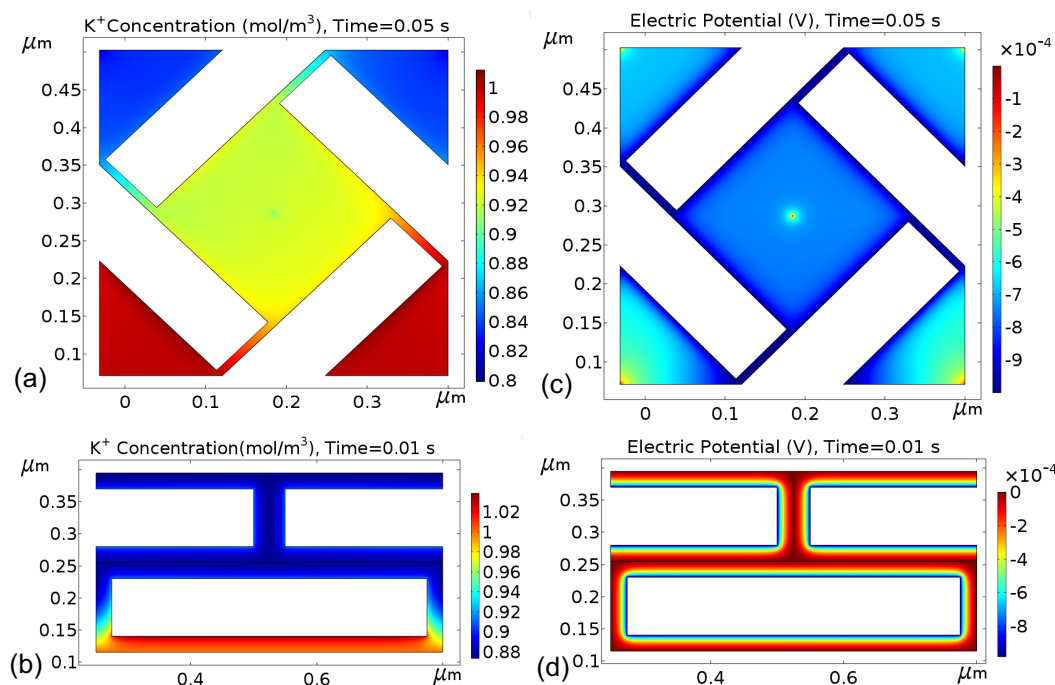


Figure 4.8 (a),(b) K^+ ions concentration contour plots, and (c),(d) electric potential profiles for square and staggered nanoarchitecture unit cells [135].

The maximum electric potential can be observed around rGO/ANF surfaces in both unit cells. Figure 4.9 shows the concentration-time profile of K^+ and OH^- ions at point P at the center of unit cell. The ions proceed in the unit cell through a Fickian diffusion mechanism. The lower equilibrium value for K^+ ions compared to OH^- ions at point P at the center of unit cell is due to accumulation of K^+ ions along the negatively polarized rGO/ANF surfaces with -1 mV potential against the bulk solution which attracts K^+ ions while repelling OH^- ions.

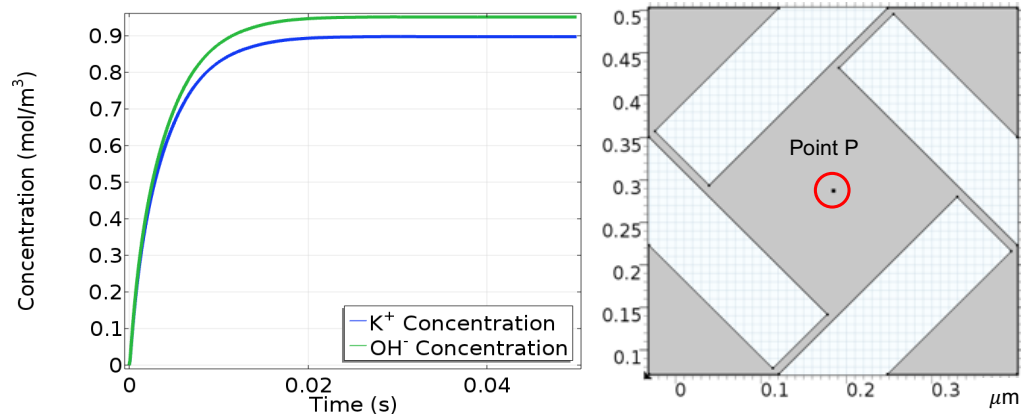


Figure 4.9 Concentration-time plot of K^+ and OH^- at point P shows that ions progress in the unit cell through a Fickian diffusion mechanism [135].

The concentration-length plot confirms that the cations in the electrolyte are accumulated at the surface of rGO/ANF, while the anions are depleted as shown in Figure 4.10. The Gouy-Chapman-Stern (GCS) theory predicts the thickness of diffuse layer to be in the same order of magnitude as the Debye length. The Debye length in KOH solution is calculated to be 9.74 nm away from rGO/ANF surface. Therefore, at the center of square unit cell which is 100 nm far from the rGO/ANF surface, the electrolyte is assumed to be electroneutral bulk solution with zero electric potential. The staggered unit cell concentration profiles against time and nanochannel length also are shown in Figure B.8 in the Appendix B. In this study, the average pore size in each nanostructure is estimated between 300-500 nm² through SEM image processing. The electrolyte used in both experiment and simulation is aqueous solution potassium hydroxide containing K^+ and OH^- ions with ionic radius of 0.133 nm and 0.110 nm, respectively as well as H_2O molecules with molecular radius of 0.138 nm. Since the average nanopore size is 1000 times larger than the diffusing ions, the interfaces are assumed to induce a homogenous charge distribution near the surface of the electric double-layer. However, in the nanochannels the counter-ions to the static charge of electrode surface can be predominant over the co-ions.

Since the electrode surface is assumed to be negatively charged, the amount of K^+ ions close to the surface of nanopores is greater than OH^- ions due to accumulating near the negatively charged electrode surface as shown in Figure 4.10. The GCS theory describes the electric double-layer and predicts the material behavior adequately. However, in case of near-complete exclusion of co-ions, such that only one ionic species exists in the nanoscale pores, the model may not provide sufficient information about the local potential and concentration distributions. In order to model nanopores smaller than 10 nm, nonadditive potential should be taken into account to correctly characterize the thermodynamic properties of nanocomposite materials [143][144][145].

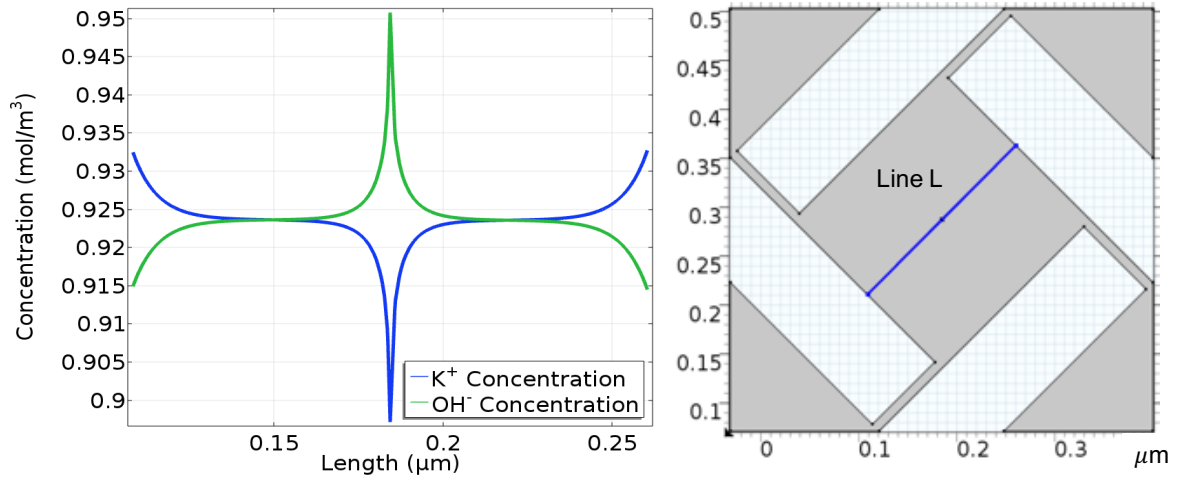


Figure 4.10 Concentration-length plot for line L shows that K^+ ions are attracted towards the negatively charged rGO/ANF surface while OH^- ions are repelled [135].

The electric potential profile for applied potential of -1 mV at the interface is obtained along line L. As it is shown in Figure 4.11a, the electrolyte potential increases exponentially on the Debye length and goes to -0.76 mV at equilibrium and then approaches to zero due to the applied ground boundary condition at the center. In the nanochannels, the electric potential reaches the maximum value of -0.985 mV after 0.05s

as shown in Figure 4.11b. For the electric potential development in nanochannel in the staggered unit cell refer to Figure B-9 in Appendix B.

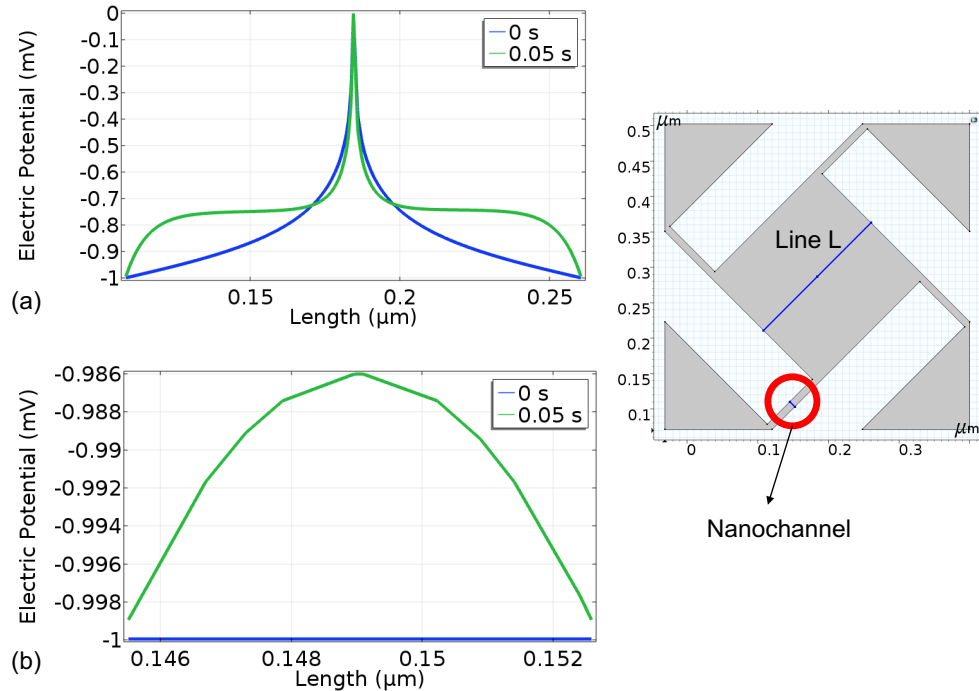


Figure 4.11 Electric potential profile at $t = 0$ s and $t = 0.05$ s for (a) Line L, (b) nanochannel. The electric potential near the surface of rGO/ANF sheets is -1 mV and at the center of line L goes to zero and increases to -0.986mV for nanochannel [135].

The effective diffusion coefficient for each composite material is calculated by evaluating the slope of the linear part of the average concentration-time^{1/2} plots shown in Figure 4.12 as [128]

$$D_{\text{eff}} = \frac{\pi}{t} \left(\frac{M_t L}{4M_{\text{eq}}} \right)^2, \quad (4.16)$$

here, M_t is the concentration (mol/m^3) at time t . In this simulation, D_{eff} is assumed to be Fickian effective diffusion coefficient (m^2/s), while L is the electrode thickness and M_{eq} is the equilibrium concentration. The results obtained from nanoarchitecture modeling and porous media approach are reported in Table 4.3 and Table 4.4 for house of cards and layered structures, respectively and compared with the experimental measurements.

The effective diffusion coefficients obtained from nanoarchitecture modeling have better agreement with experimental measurements.

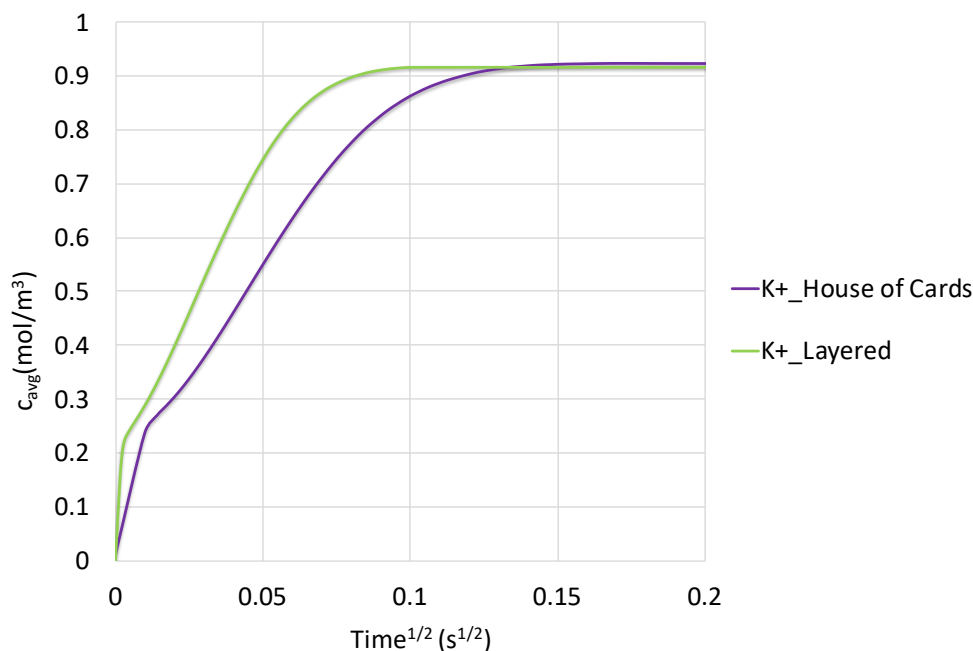


Figure 4.12 Average concentration-time^{1/2} for house of cards and layered structures to calculate effective diffusion coefficient of K⁺ ions [135].

The plot shown in Figure 4.13 compares the D_{eff} calculated from porous media approach and nanoarchitecture modeling for porosity percentages between 0%-70%. It can be seen that porous media approaches overestimate the value of D_{eff} which can decrease the accuracy of electrochemical properties in nanocomposite materials.

The higher values of ionic diffusivity obtained through simulation compared to experimental measurements are expected due to the perfectly arranged rGO/ANF sheets throughout the electrode medium. On the other hand, the lower value of D_{eff} in experimental measurements is due to randomly arranged rGO/ANF sheets that introduces more tortuosity and complexity in ionic pathways.

Table 4.3 Comparison of transport properties of house of cards nanostructure [135].

Approach	Porous Media Method		Nanoarchitecture Modeling	Experiment
	Bruggeman [130]	Millington-Quirk [132]	PNP Coupling [114]	EIS Measurement [142]
Governing Equation	$\tau = \varepsilon^{-1/2}$ $D_{\text{eff}} = \frac{\varepsilon}{\tau} D$	$\tau = \varepsilon^{-1/3}$ $D_{\text{eff}} = \frac{\varepsilon}{\tau} D$	$\tau = L_1/L_0$ $D_{\text{eff}} = \frac{\pi}{t} \left(\frac{M_t T}{4M_{\text{eq}}} \right)^2$	$\sigma = \frac{RT}{z^2 F^2 A \sqrt{2}} \left(\frac{1}{c D_{\text{eff}}^{1/2}} \right)$
Porosity (ε)%	51.45	51.45	NA	NA
Tortuosity (τ)	1.39	1.25	1.37	NA
D_{eff} (m ² /s)	3.69×10^{-11}	4.12×10^{-11}	2.43×10^{-12}	5.40×10^{-13}

Table 4.4 Comparison of transport properties of layered nanostructure [135].

Approach	Porous Media Method		Nanoarchitecture Modeling	Experiment
	Bruggeman [130]	Millington-Quirk [132]	PNP Coupling [114]	Cyclic Voltammetry [141]
Governing Equations	$\tau = \varepsilon^{-1/2}$ $D_{\text{eff}} = \frac{\varepsilon}{\tau} D$	$\tau = \varepsilon^{-1/3}$ $D_{\text{eff}} = \frac{\varepsilon}{\tau} D$	$\tau = L_1/L_0$ $D_{\text{eff}} = \frac{\pi}{t} \left(\frac{M_t T}{4M_{\text{eq}}} \right)^2$	$i_p = 0.45 zFAC \left(\frac{zFvD_{\text{eff}}}{RT} \right)^{1/2}$
Porosity (ε)%	41.56	41.56	NA	NA
Tortuosity (τ)	1.56	1.35	2.35	NA
D_{eff} (m ² /s)	2.61×10^{-11}	3.03×10^{-11}	1.95×10^{-12}	3.88×10^{-14}

The path tracking method is used to calculate tortuosity for each nanoarchitecture. The tortuosity is defined as the ratio of the actual path length inside pore channels L_1 to the thickness of the porous medium L_0 as shown in Figure 4.14. Path L_1 is understood here as the shortest continuous line between any two points within the pore space, divided by the straight path that connects two points and is calculated as [129]

$$\tau = \frac{L_1}{L_0}. \quad (4.17)$$

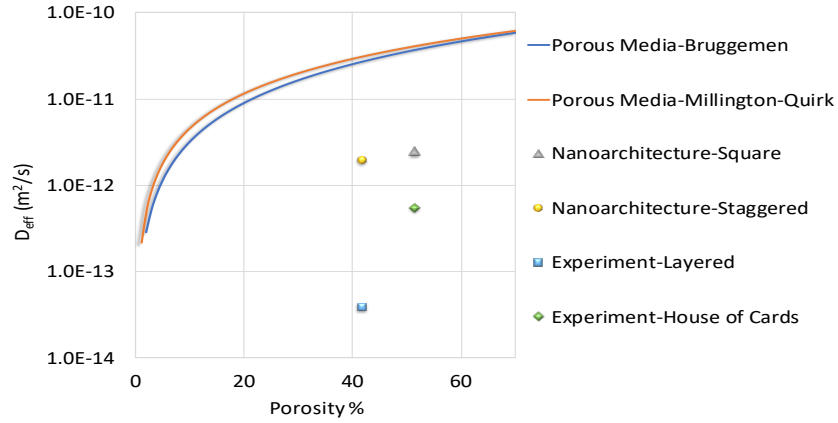


Figure 4.13 Comparison of the calculated D_{eff} for porosity% (0-70%) through porous media approaches and nanoarchitecture modeling [135].

The value of tortuosity calculated for house of cards nanoarchitecture is in the same range as porous media methods. However, the value of tortuosity in staggered nanoarchitecture has higher value due to the wider pathways between rGO/ANF sheets compared with house of cards structure.

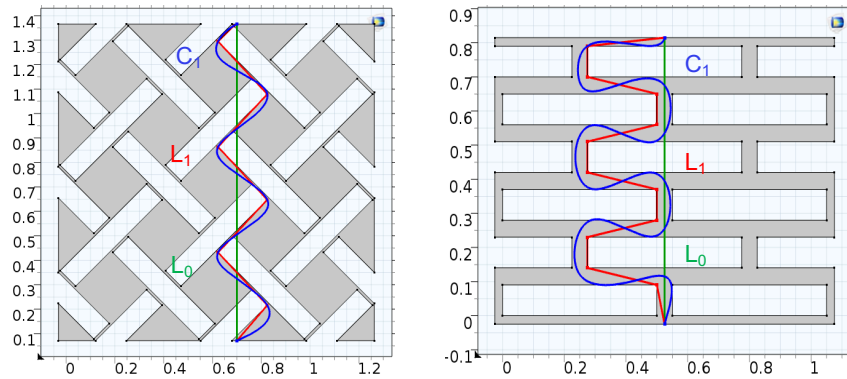


Figure 4.14 Path tracking method to calculate the tortuosity of the nanoarchitectures regarding $\tau = L_1/L_0$ which is defined as the shortest pathway between two points within the geometry; Curve C_1 can represent the longest pathway between two points [135].

5 Computational Modeling of rGO/ANF Structural Supercapacitors

5.1 Introduction

In the previous chapters, we mainly have focused on modeling the rGO/ANF structural electrodes and investigating the effect of various nanoarchitectures on ionic diffusivity within the electrode materials. In this chapter, we are going to move on to the device level and develop a model for a single cell supercapacitor made of two identical rGO/ANF electrodes [15][16][17][18][19]. However, to continue our previous work, the effective properties obtained from nanoarchitecture modeling are used to capture the electrochemical behavior of the whole cell supercapacitor, illustrated in Figure 5.1. Here, we aim to simulate the electric double layer dynamics in cyclic voltammetry measurements accounting for transport phenomena at the electrode/electrolyte interface.

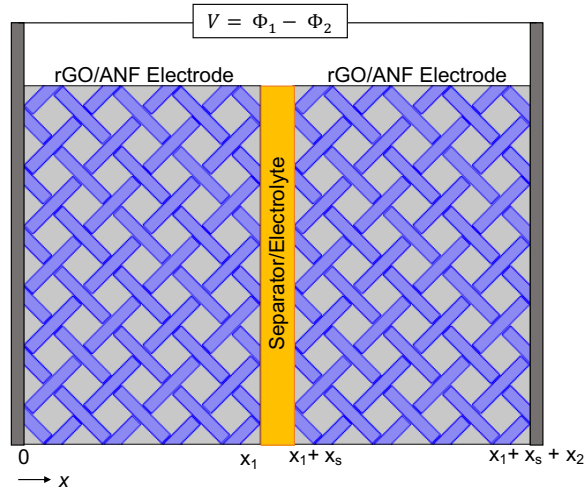


Figure 5.1 Schematics of rGO/ANF structural supercapacitor with house of cards nanoarchitecture.

Cyclic voltammetry measurement is one of the widely used electrochemical characterization techniques [146]. In cyclic voltammetry, the electric potential at the electrode surface varies periodically and linearly with time. The current-voltage waveform, called voltammogram, provides useful information about the reactivity and mass transport

properties of the electrolyte [115][116][146]. By applying an external electric potential to a supercapacitor, the electrolyte's solvated ions with the opposite charge adsorb to the electrode surface due to the electrostatic forces and form an electric double layer [1][114][115][116][146]. When the electrode surface potential varies in a “potential window”, the recorded current profile indicates the rates of chemical reactions in the solution and different physical phenomena for ionic transfer. The CV curve exhibits the competition between the rate of electrolysis in the electric double layer and the rate of transport of the reacting chemical species to the electrode surface by diffusion. The current is linearly dependent on the ionic concentration and the area enclosed by the CV curves is used to determine the capacitance of the supercapacitor [1][115][146][147].

In experimental studies, cyclic voltammetry has been extensively used to characterize the electrochemical behavior of anodes, cathodes and electrolytes in various energy storage devices such as Li-ion batteries [148][149][150][151][152][153][154][155][156][157][158][159], flow batteries [160][161][162][163][164], fuel cells [165][166][167][168][169][170], supercapacitors [171][172][173][174][175][176] and biological compounds [177][178][179][180][181]. For design and research however, experiments can be time-consuming and costly. Since the chemistry of the electrode-electrolyte interface is still not fully understood, characterization of cyclic voltammetry through thermodynamics fundamentals and computational modeling is essential to provide additional insights into the electrochemical kinetics and electrolysis.

5.2 Modeling Cyclic Voltammetry

Numerous models and simulation methods have been developed to predict the cyclic voltammetry measurements of supercapacitors. One of the modeling approaches is

to simulate CV curves by virtue of an equivalent circuit consists of an arbitrary number of resistors and capacitors, called RC circuit models. The RC circuit models require experimental measurements prior to the simulation, and they neglect the physical phenomena such as diffusion, electrolyte's non-uniform ion concentration and electrode morphology [182][183][184][185][186][187][188][189][190][191][192][193].

To investigate the ionic transfer at the electrode/electrolyte interface, many studies have focused on molecular dynamics simulations, alternatively. However, MD modeling has extensive limitations to simulate multiscale systems as well as long time-scale processes such as cyclic voltammetry due to the large number of particles required for simulation [194][195][196][197][198][199][200][201].

On the other hand, many literatures have considered continuum models to investigate transport phenomena and kinetics of supercapacitors through Nernst-Planck equation [78][79][80][81][82][83][98][93][95][94][92]. Continuum models are developed to analyze electrode/electrolyte interface considering diffusion, ionic concentration, particle size and electrode morphology over a potential window and timescale of cyclic voltammetry experiment [202][203][204][205][206][207][208][209][210].

Continuum modeling enables multi-dimension and multiscale simulations. For example, Wang and Pilon [202][203][204][205] have developed continuum models using the modified Poisson–Nernst–Planck (MPNP) model with a Stern layer to simulate and interpret cyclic voltammetry measurements of transient dynamics of electric double layer capacitors. In these studies, the electric double layer capacitance was numerically predicted for spherical ultra-microelectrodes of various radii in aqueous electrolyte [202]. They also concluded that Helmholtz model underestimates the Stern layer capacitance for sphere radii

less than 40 nm when accounting for field-dependent permittivity. They have expanded their model and considered various ionic sizes and electrode's nanoarchitectures [203][204][205]. It is concluded that the shape of CV curves is due to the saturation of ion concentration at the electrode surface as the electric potential increased. They have concluded that the morphology of mesoporous electrodes can significantly affect the charging and discharging of EDLCs. Also, the predicted electrolyte ionic conductivity obtained through this simulation was equal to the theoretical value when ignoring the electrode contribution to the resistance. In another study, Mei and Pilon [206] have developed a 3D model to simulate CV cycles of an electric double layer capacitor with carbon electrodes. In their model, the electrodes nanoarchitecture is considered through highly ordered monodisperse spherical carbon nanoparticles as simple cubic (SC) and face-centered cubic (FCC) packing. They have concluded that the areal capacitance increases with decreasing sphere diameter.

A thin layer model is used by Streeter et al. [207] to illustrate the effects of diffusion within a porous layer. They found that above a certain layer thickness, the diffusion layer is not perturbed by the insulating surface on the experimental timescale and a semi-infinite planar diffusion model alone is not appropriate for interpreting the kinetics of the electron transfer at this electrode surface. Some of the studies have focused mainly on electrode's pore size and distribution and its effects on CV measurements [208][209][210]. As an example, Chevallier et al. [210] explored the effects of different physical and electrochemical parameters on the mass transport properties and cyclic voltammetry of a planar electrode modified with an insulating surface coating containing non-interconnected cylindrical pores. They have shown that beside scan rate and the standard electron rate

constant, parameters such as pore distribution and pore radius have a considerable qualitative influence on the mass transport properties. Digital simulation techniques are used to investigate the cyclic voltammetry of polymer thin film [211], slow scan limit conditions of reversible electrode processes [212] and the voltammetry of the metal complex in the presence of DNA [213]. In one study the Artificial Neural Network (ANN) is used to simulate the cyclic voltammetry of MnO_2 supercapacitor with satisfactory low error rates [214]. Moreover, the fast Fourier transform methods are used to simulate the mechanisms of electrode process in alternating current (ac) voltammetry covering a large amplitude case [215].

Since electrochemical kinetics are frequently nonlinear and voltammetry is a transient problem, the theory is not admissible to analytical solutions, except in a few limiting cases [216]. For this purpose, computer simulation is necessary and software applications such as COMSOL Multiphysics can facilitate the design of electrodes in a more systematic and efficient way. COMSOL Multiphysics' modules can also account for various and complex phenomena and identify the dominant processes governing the capacitance behavior of the electrode by providing a powerful and flexible user interface for finite element methods [203][204][205][206][217]. For instance, Lavacchi et al. [217] developed a 2D model to capture CV behavior of micro-disk electrodes in square arrays of both inlaid and recessed. They examined the effect of different software features such as meshing on the results and were able to compare their simulated results with experimental measurements reported in the literatures.

In this study, we aim to utilize Electroanalysis module in COMSOL Multiphysics and simulate the cyclic voltammetry measurements of rGO/ANF structural

supercapacitors. Through a numerical simulation, the material properties such as bulk concentration of species, transport properties, and kinetic parameters of rGO/ANF composite electrodes are determined and compared with experimental measurements. In this model, a Parametric Sweep is used to compare voltammetry recorded at different voltammetric scan rates.

5.3 Governing Equations

The structural supercapacitor made of rGO/ANF nanocomposites is considered as an electric double layer capacitor without any Faradic redox reactions. The coupled Poisson-Nernst-Planck [114][115][116] model is adopted to describe the ionic transfer in the electric double layer capacitor. The Poisson equation governs the evolution of the electric potential, Φ in the diffuse layer as [114][115]

$$\nabla \cdot (\epsilon_0 \epsilon_r \nabla \Phi) = -F(z_+ c_+ - z_- c_-), \quad (5.1)$$

while it is zero in the Stern layer very close to the electrode surface. Here, $\epsilon_0 = 8.85 \times 10^{-12}$ F/m is the vacuum permittivity, and ϵ_r is the field-dependent dielectric constant of the electrolyte which is 80.5 for KHO solution as the electrolyte solution in this study. The Faraday constant is represented by F , while c_i is the concentration of the species (i) and z_i is the charge number, respectively.

The Nernst-Planck equation [114] evaluates the concentration of species in the binary electrolyte correspond to the ion fluxes due to diffusion and electromigration according to

$$\frac{\partial c_i}{\partial t} = \nabla \cdot \left[D_i \left(\nabla c_i + c_i \frac{z_i F}{RT} \nabla \Phi \right) \right], \quad (5.2)$$

where, D_i is the diffusion coefficient, and R and T are the universal gas constant and temperature, respectively. The Nernst diffusion layer or linear diffusion layer is the extent

of the region in the electrolyte solution where concentration changes take place [146][147]. Diffusion layer is usually considered to be some multiple of $(Dt)^{1/2}$, where $1/t$ equals to the scan rate. To ensure that the diffusion layer greatly exceeds the mean diffusion layer thickness, $(Dt)^{1/2}$ is multiplied by factor 6 as a conservative setting. Therefore, diffuse layer thickness δ is defined as the efficiency of diffusion (D) over the duration of the voltammetry experiment (t_{\max}) as

$$\delta = 6\sqrt{Dt_{\max}}. \quad (5.3)$$

This equation provides a useful approach to the species concentration profiles and the diffusive mass transport in electrochemical systems. In cyclic voltammetry the diffusion layer depends on scan rate. At slow scan rates, the diffusion layer is on the order of micrometers, whereas at fast scan rates, its thickness is in nanometers.

In boundary conditions, the “potential window” is applied at the electrode surface as a triangular waveform according to two vertex potentials along with a voltammetric scan rate, v in V/s. At the electrode surface the potential varies linearly and periodically with time according to [202][203]

$$\Phi(t) = \begin{cases} \Phi_{\min} + vt & \text{for } 2(n-1)t_0 \leq t < (2n-1)t_0, \\ \Phi_{\max} - v[t - (2n-1)t_0] & \text{for } (2n-1)t_0 \leq t \leq 2nt_0, \end{cases} \quad (5.4)$$

where n is the cycle number and $t_0 = (\Phi_{\max} - \Phi_{\min})/v$ is half the cycle period and represents the time for the surface potential to vary in the potential window from its Φ_{\min} to its Φ_{\max} values. The potential at the bulk solution is zero due to electroneutrality assumption. For ideal supercapacitors, it is assumed that no reaction happens at the electrode/electrolyte interface. However, the influence of transient applied voltage on the rate of the electrolysis reaction at the rGO/ANF electrode surface is investigated to accurately predict the shape

of voltammetry measurements obtained from experimental studies. One of the pre-built electrochemical kinetics in COMSOL Electroanalysis module is the Butler-Volmer equation which describes the local current density (i_{loc}) based on overpotential (η), reaction rate constant (κ_0), and transfer coefficient (α_c) for anode and cathode according to [115]

$$i_{loc} = zF\kappa_0 \left(c_1 \exp\left(\frac{(z - \alpha_c)F\eta}{RT}\right) - c_2 \exp\left(\frac{-\alpha_c F\eta}{RT}\right) \right). \quad (5.5)$$

The transfer coefficient describes the kinetics of electrochemical reaction and signifies the fraction of overpotential at the electrode electrolyte interface that helps in lowering the free energy barrier for the electrochemical reactions. Another pre-built electrochemical kinetics is the Tafel equation which relates the rate of an electrochemical reaction to the overpotential for single electrode as [115]

$$i_{loc} = i_0 10^{\frac{\eta}{A_c}}, \quad (5.6)$$

here, i_0 is the exchange current density (A/m²) and A_c is the Tafel slope (V). The Tafel slope for high scan rates can be determined as [115]

$$A_c = \frac{\alpha z F}{2.303 RT}. \quad (5.7)$$

The Tafel slope explains the amount of overpotential required to active a reaction. It is the magnitude of the change in activation energy for a given increase in overpotential. According to Faraday's laws of electrolysis, the flux of the reactant and product species are proportional to the current density [114][115][116]

$$-n_i J_i = \frac{v i_{loc}}{z_i F}, \quad (5.8)$$

here, the v is the applied potential scan rate at the electrode surface. The total current is related to the current density multiplied by the electrode area A drawn

$$I_{total} = i_{loc}A. \quad (5.9)$$

The concentration boundary condition at the bulk electrolyte is assumed to be a uniform concentration equal to c_{bulk} for reactants and zero for products. The parameters used in this simulation are reported in Table 5.1 while the unknown physical quantities such as capacitance and internal resistance in the system can be inferred by ‘fitting’ to experimental data.

Table 5.1 Parameters used in simulation of CV measurements of rGO/ANF electrodes.

Parameter	Symbol	Unit	Value
Voltammetric scan rate	ν	V/s	0.02
Reactant bulk concentration	c_{bulk}	mol/m ³	6000
Reactant diffusion coefficient	D_A	m ² /s	10 ⁻¹⁴
Product diffusion	D_B	m ² /s	10 ⁻¹⁴
Electrode thickness	L_e	mm	8
Temperature	T	K	298.15
Start potential	E_1	V	0
Switching potential	E_2	V	1
Reaction rate	κ_0	unitless	10 ¹⁰

5.4 Modeling Assumptions

A deliberate simplification of the underlying equations describing cyclic voltammetry is advantageous to make the model more tractable and understandable. For domain equation, it is assumed that a large amount of supporting electrolyte or an inert salt presents at the electrode/electrolyte interface. Supporting electrolyte mitigates electric fields by increasing the electrolyte conductivity and reducing its resistivity; hence the potential term in Nernst-Planck equation can be neglected. Also, the natural convection

$(c_i v_i)$ term in the domain equation is not considered, since it is assumed that the solution is unstirred and is in a stagnant condition. Therefore, in the domain equation only diffusion contributes to chemical species transport and only in the direction normal to the electrode surface and the influence of the electrode edge can be neglected. This makes voltammetric analysis a 1D time-dependent problem and diffusion of the electroactive species within the thin layer is described by Fick's second law as

$$\frac{\partial c_i}{\partial t} = D_i \frac{\partial^2 c_i}{\partial x^2}. \quad (5.10)$$

The reactions and transport are assumed to be uniform across the electrode surface. The Electroanalysis module in COMSOL Multiphysics is utilized to simulate cyclic voltammetry of both layered and hydrogel rGO/ANF structural electrodes.

5.5 Results and Discussion

The simulation results of cyclic voltammetry measurements are obtained for rGO electrodes with various compositions of ANF for “layered” nanostructure. Figure 5.2 shows the modeling results obtained for rGO, rGO/10wt%ANF, and rGO/25wt%ANF with layered nanostructure. The model shows a very good agreement with experimental measurements. The CV plots display a rectangular shape that is the characteristic of ideal supercapacitor. It can be seen that by increasing ANF percentage the capacitance of the electrodes decreases. The model shows a symmetric behavior for both cathodic and anodic processes. For ideal supercapacitor, the local current density i_0 is assumed to be zero and therefore the electrode kinetics is zero. In this case, the driven force in ion transfer is mainly due to the electrostatics and double layer electric potential. Since there is no chemical reaction, no obvious peaks can be seen in both anodic and cathodic processes. By applying potential triangular wave that switch the potential sweep rate from low to high, the steady

state current changes from vC_d during the forward scan (anodic process) to $-vC_d$ during the backward scan (cathodic process). The value of C_d is the constant capacitance of the system.

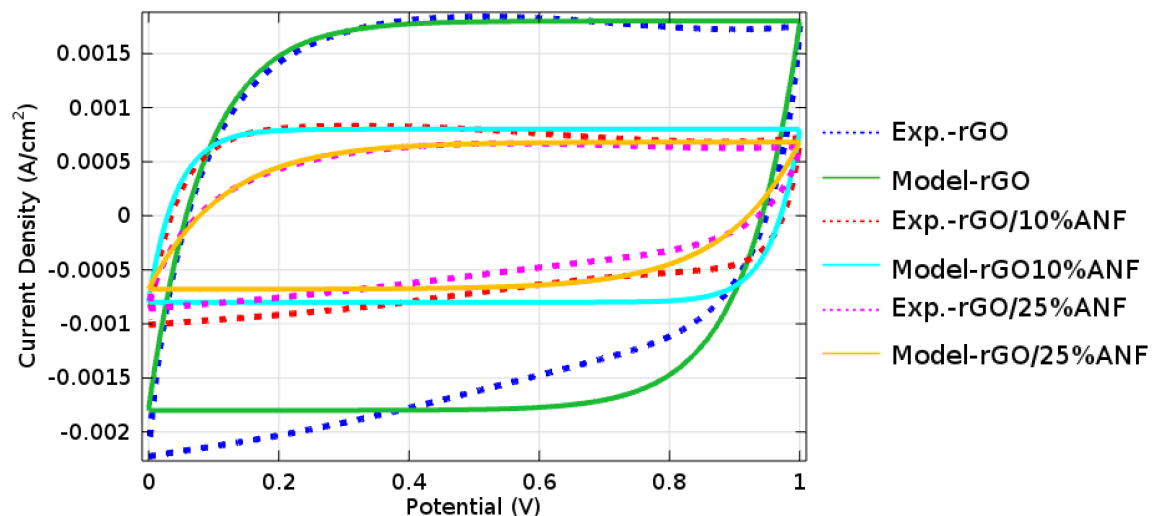


Figure 5.2 Ideal supercapacitor modeling for cyclic voltammetry measurements of rGO, rGO/10%ANF, and rGO/25%ANF.

However, increasing ANF percentage shows more asymmetric behavior in CV measurements. To investigate the electrochemical behavior of electrodes, different electrode kinetics with very low local current density are applied at the electrode/electrolyte interface. Figure 5.3 compares the ideal supercapacitor with the Butler-Volmer equation and the anodic Tafel equation. Here, the local current density is assumed to be 10^{-5} A/m². The Tafel equation with smaller values for Tafel slope (< 450) shows the electrolyte decomposition at the higher voltage values (> 0.7). Increasing the Tafel slope shows ideal capacitor behavior in the simulated CV curves. Modeling results for Butler-Volmer equation shows more symmetric behavior than the Tafel equation in CV measurements.

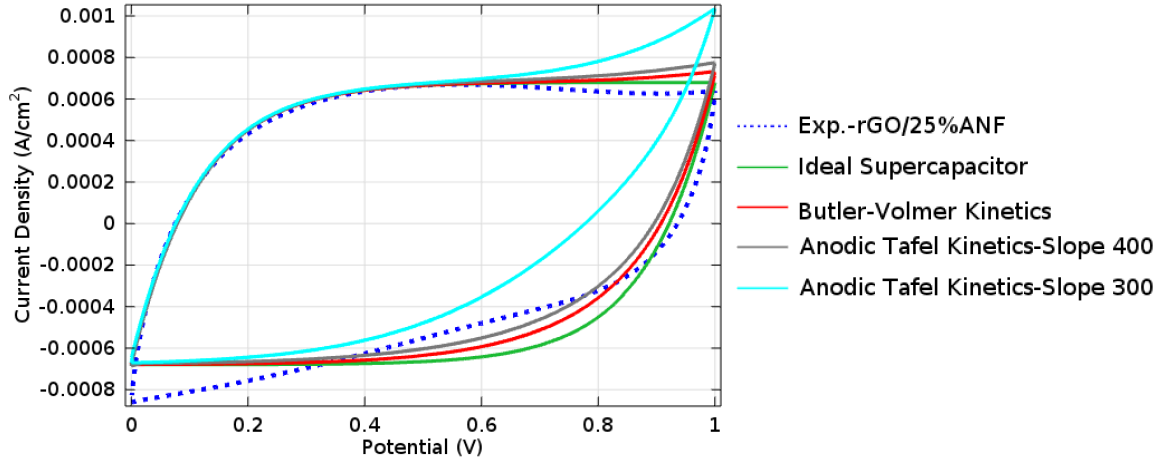


Figure 5.3 Comparison of various electrode kinetics for rGO/25%ANF CV measurements.

The CV curve for pure rGO electrode shows ideal capacitor behavior compared to rGO with higher percentage of ANF. Figure 5.4 shows electric potential profiles and the average current density. The electric potential sweep linearly as a triangular wave at the electrode/electrolyte interface. The ion concentration profile during the operation time is also shown in Figure 5.5. The concentration at the electrode surface is driven to zero as the current increases. Once the surface concentration is zero, the concentration gradient relaxes under diffusion. The concentration returns to its bulk value at the electrode surface as the current is inverted by the reverse reaction during the second part of the sweep.

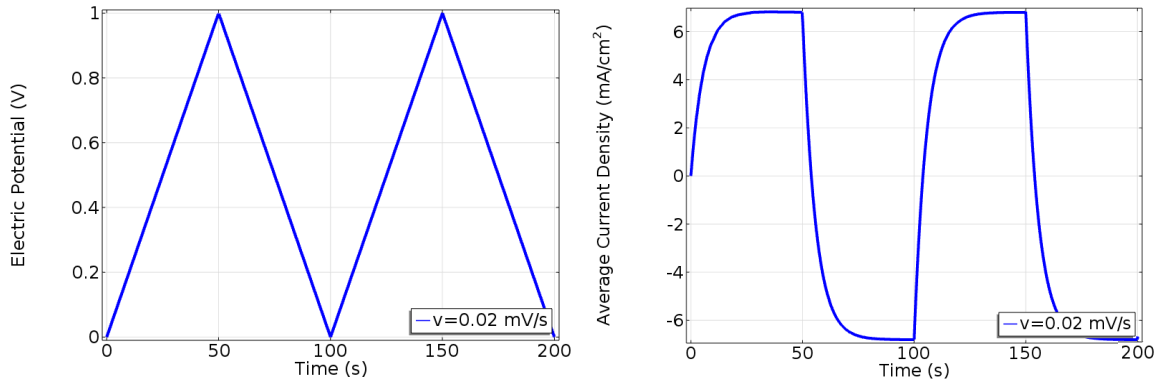


Figure 5.4 (a) Triangular cyclic potential sweep from 0V to 1V during two cycles, (b) the average current density obtained in a form of step function.

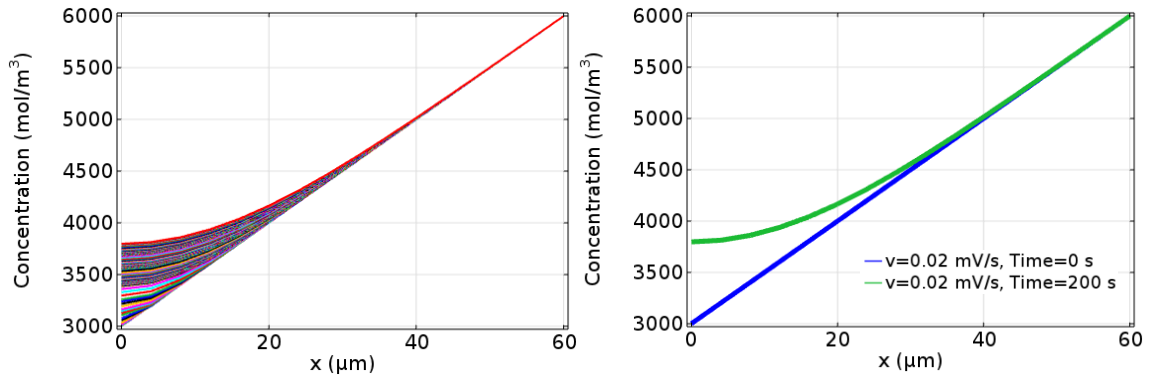


Figure 5.5 (a) Ion concentration development in the diffuse layer for rGO/10%wtANF with 20 mV/s scan rate obtained from modeling CV, (b) concentration profile at time 0s and after 200s.

The concentration profile remains the same for different electrode kinetics due to very small current density at the interface. Table 5.2 reports the capacitance and resistance of each rGO/ANF composition as fitting parameters. By increasing ANF percentage the capacitance decreases, while the internal film resistance increases. It can be explained that by the increasing the ANF percentage the nanopores in the composite are filled with ANF polymer that hinders the ionic transfer in the composite material. Moreover, increasing the nonconductive polymer matrix affects the electronic conductivity and decreases the capacitance of the supercapacitor.

Table 5.2 Resistance and capacitance obtained as fitting parameters in the simulation.

	rGO-0%ANF	rGO-10%ANF	rGO-25%ANF
Resistance (Ohm.m ²)	46.5	53	166
Capacitance (F/m ²)	0.09	0.04	0.034

5.6 Conclusions

The CV measurements of rGO/ANF structural electrodes are simulated through a multiphysics modeling. The ideal supercapacitor model is compared to various electrode kinetics such as Butler-Volmer equation and Tafel equation with very low local current density. The modeling results show a very good agreement with experimental measurements. Modeling cyclic voltammetry can provide useful information about kinetics and thermodynamics of structural supercapacitors and enables better control over the performance and life cycle of the device. Comparison of predicted and measured voltammograms enables determination of material properties and other system parameters that may be unknown, such as diffusion coefficients and reaction rates.

6 Solid Polymer Lithium-Ion Batteries

6.1 Overview

The potential safety issues related to the organic liquid electrolytes have become the main disadvantage of current commercial Li-ion batteries [219]. Although organic electrolytes are successful with high ionic conductivity and high performance, they are incorporated with risks of leakage, burning, explosion and thermal run away due to flammability and low boiling point. Incidents of overheating and burning Li-ion batteries in Samsung Galaxy Note 7, Tesla Model S, and Boeing 787 are examples that have enforced many attempts to investigate the substituting of organic liquid electrolytes with solid electrolytes such as polymers and ceramics [219][220].

Adopting solid electrolytes also prevents the dendrite growth issue in Li-metal batteries by providing a physical barrier between electrodes. Eliminating the dendrite growth issue enables the use of Li-metal anode that have higher energy density than Li-ion batteries. Compared with ceramic electrolytes, solid polymer electrolytes offer specific advantages of flexibility, excellent thermal stability, and high safety [220]. The polymers that are widely considered as solid polymer electrolytes include polyethylene oxide (PEO), polycarbonate and polysiloxane. Among these polymers, PEO and its derivatives have attracted many interests due to high ionic conductivity [34]. The polar groups of oxygens on the PEO are effective in dissolving lithium salts by involving in a Coulombic reaction, causing anions and cations of the lithium salt dissociate. The ion transport mechanism of polymer electrolyte under electric field is due to Li^+ cations jumping from one polymer segment to another, shown in Figure 6.1. The amorphous segment of PEO is responsible for ionic movement. However, the ion motion in polymer matrix is not as free as in liquid

organic electrolytes due to the boundary effect of crystalline domains and long PEO polymer chain. The low ionic conductivity of solid polymer electrolytes is still the main challenge in its commercial development [218][220].

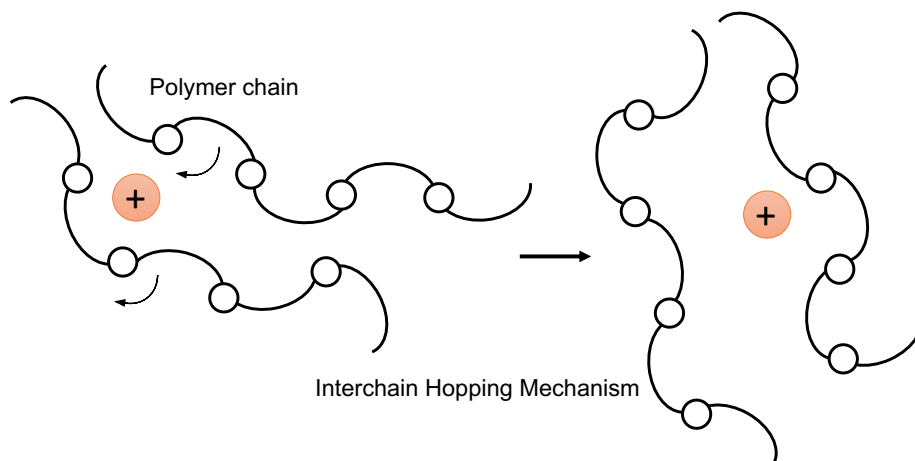


Figure 6.1 Ionic conductivity in solid polymer electrolyte is due to polymer chain segmental mobility [218].

The ionic conductivity in solid polymer electrolyte directly depends on temperature and the polymer glass transition, T_g . The ionic conductivity is very low for temperatures below T_g and improves by increasing temperature above glass transition. To improve ionic conductivity, many studies have focused on reducing T_g of PEO polymers by applying additives and plasticizers [218][219][220].

6.2 Polyethylene Oxide Solid Polymer Li-Ion Batteries

In order to investigate the effect of low temperature on solid polymer Li-ion batteries performance, several pouch cells are fabricated and tested at 4°C, 10°C, and 25°C. The electrochemical performance of the thin film batteries is tested at room temperature and low temperatures such as 10°C and 4°C inside a RH chamber (BTL 433), using the Arbin BT2000 with direct charge-discharge chronopotentiometry procedure and by applying an adequate current rate with defined lower and higher cut-off voltages (3 to

4.2V). The results show promising electrochemical properties that suit for low-temperature applications.

The average capacity of the solid polymer batteries is 0.09 mAh/cm² at room temperature and 0.02 mAh/cm² at 4°C. The high capacity drops at low temperatures can be mitigated by adding a small quantity of liquid electrolyte to the surface of the electrodes. It increases the average capacity to 0.63 mAh/cm² at 25°C and 0.19 mAh/cm² at 4°C. In the next chapter, a 1D thermo-electrochemical modeling is developed and the simulation results are compared with the experimental measurements [34].

6.3 Thermal Modeling of Li-Ion Batteries

The working environment of Li-ion batteries has significant influence on their performance. In application such as subsea and space, the extreme operating conditions such as external forces, low temperature and high temperature conditions accelerates battery degradation and loss of power [221].

Battery performance under low temperatures has been studied both experimentally and computationally [221]. Numerous researchers have addressed the development of thermo-electrochemical models that can predict the battery behavior at both high and low temperatures [222]. For example, Cai and White [45] have developed a thermal model by coupling the pseudo two-dimensional model and thermal model utilizing COMSOL Multiphysics. In their model, they have used single particle electrode model to describe electrochemical behavior of their conventional Li-ion battery. They have concluded that their model can predict the temperature increase inside the battery. Moreover, this model can be used to predict thermal runaway by considering different thermal boundary conditions. The same approach is adopted by many other researchers to investigate the

thermal effect on Li-ion batteries performance [223][224][225][226][227][228]. The effect of low temperature on Li-ion performance is considered recently, since the battery application in automotive as well as subsea are increasing and at low temperature battery performance significantly decreases. In one study, Ji et al. [229] have considered low temperature effects on 18650 cylindrical Li-ion battery performance. Their simulation and experimental results have demonstrated dramatic effects of cell self-heating upon electrochemical performance at low temperatures. Also, they have proposed a Ragone plot accounting for thermal effects for the first time for Li-ion cells. However, in their model the battery aging and degradation due to low temperature are neglected. In another work, Tippmann et al. [230] have considered a wide range of temperature from -25°C to 40°C with different C rates. The battery aging and degradation are also taken into account. They have determined the capacity fade after a significant number of cycles and compared the results to the data obtained through electrochemical impedance spectroscopy measurements. Their model can be used to predict the aging effects during the charging process which is due to lithium deposition on the anode surface.

In the next chapter, a thermo-electrochemical model is developed to investigate the low temperature effects on solid polymer Li-ion batteries. The modeling approach follows the coupling method reported in the literature. The battery performance is considered through voltage vs. discharge capacity plots.

7 The Effect of Low Temperatures on Solid Polymer Li-Ion Batteries

7.1 Introduction

In this chapter, a 1D thermo-electrochemical model is developed to investigate the effect of low temperatures on solid polymer Li-ion batteries performance. The battery device considered in this study is a flexible pouch cell consists of graphite (LiC_6) anode, lithium cobalt oxide (LiCoO_2) cathode, and polyethylene oxide (PEO) solid polymer electrolyte (SPE). Figure 7.1 shows the schematics of the pouch cell components and the single particle model applied to investigate the electrochemical performance of Li-ion batteries [45][223][224][227][229][230].

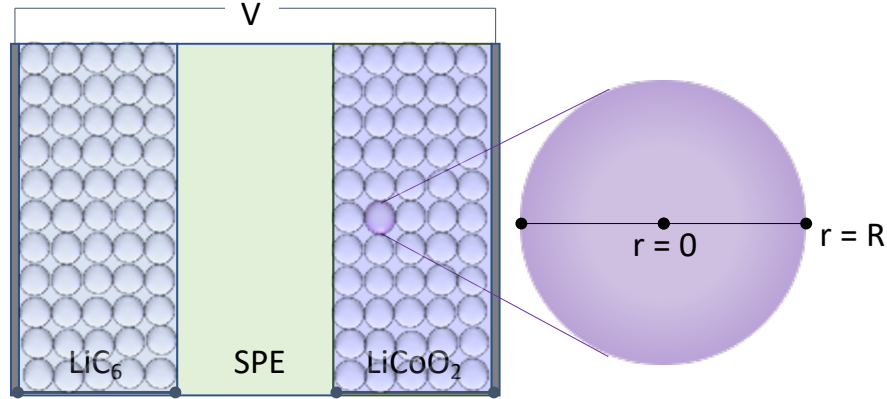


Figure 7.1 Schematics of pouch cell and the single particle model [223][224][225].

The porous electrode materials are assumed to be homogenous spherical particles with identical size. This assumption simplifies the boundary conditions for electrode materials since the reaction current distribution across the electrodes assumed to be uniform. It is also assumed that there are no side reactions [45][224]. In the real LIB system, side reactions may occur due to the solid electrolyte interface (SEI), electrolyte decomposition, and solvent reduction reaction. These side reactions will lead to irreversible

capacity loss. It is also assumed that the current collectors have a negligible impact on Li ions transfer and heat transfer. It is well known that the most common utilized current collector in the battery system such as the copper and aluminum are very good thermal conductor, and this can impact the battery performance [45][224]. However, this assumption is reasonable for low applied current densities and small sample dimensions. Diffusion of ions into active materials is assumed to be Fickian. In fact, non-Fickian transport may occur due to several effects like the effect of structural changes, relaxation, swelling, internal stresses caused by the temperature variation, age and pre-history of the device, and sample dimensions. All these factors are neglected in this work based on the first assumption [222].

7.2 Governing Equations

7.2.1 Electrochemical Single Particle Model

In this model, the mass balance equation for Li ions diffusion in the solid particle active material is governed by the Fick's second law of diffusion for both the positive and negative electrodes [45][80][78][82][83][224]. The material balance equation in spherical coordinate in one dimension is

$$\frac{\partial c_{s,j}}{\partial t} = \frac{D_{s,j}}{r^2} \frac{\partial}{\partial r} \left(r^2 \frac{\partial c_{s,j}}{\partial r} \right), \quad (7.1)$$

where $c_{s,j}$ and $D_{s,j}$ are the concentration and diffusion coefficient of Li ions in the solid electrode phase. This equation is the domain equation for both the positive and negative electrode particles and the subscript $j = p/n$ represents the positive/negative electrode.

The diffusion coefficient can be considered as a temperature-dependent parameter according to the Arrhenius equation through an exponential expression of [224]

$$D_{s,j} = D_{0,j} \exp\left(-\frac{E_{a,j}}{R}\left(\frac{1}{T_0} - \frac{1}{T}\right)\right), \quad (7.2)$$

where $D_{0,j}$ is reference diffusion coefficient (m^2/s) of Li ions in solid electrode active materials at the initial temperature, $E_{a,j}$ is the activation energy (J/mol), T is the temperature (K), and R is the universal gas constant, $8.314 \text{ (J mol}^{-1} \text{ K}^{-1})$.

The concentration of ions at the center of electrodes is assumed to be zero. Then, the boundary condition at the center is defined as [45]

$$-D_{s,j} \frac{\partial c_{s,j}}{\partial r} \Big|_{r=0} = 0. \quad (7.3)$$

At the electrode/electrolyte interface, the molar flux is equal to the consuming/producing rate of Li ions due to the electrochemical reaction as

$$-D_{s,j} \frac{\partial c_{s,j}}{\partial r} \Big|_{r=R_j} = J_j, \quad (7.4)$$

where J_j is the flux of Li ions away from the surface of the spherical particles with radius R_j and can be expressed as

$$J_j = \frac{\pm I_{app}}{zF\left(\frac{3}{R_j}\right)\varepsilon_j V_j}, \quad (7.5)$$

where I_{app} is the total current passing through the cell tabs and is defined in this work as positive for charge process and negative for discharge process. F is Faraday's constant, 96487 C/mol . ε_j and V_j are the volume fraction (porosity) and total volume of the electrodes, respectively.

The Butler-Volmer equation expresses the electrochemical reaction kinetics at the electrode/electrolyte interface as

$$J_j = i_{0,j} \left(\exp\left(\frac{0.5F}{RT}\eta_j\right) - \exp\left(-\frac{0.5F}{RT}\eta_j\right) \right), \quad (7.6)$$

where η_j is the overpotential and the exchange current density $i_{0,j}$ is defined as

$$i_{0,j} = F\kappa_j \sqrt{(c_{s,j,max} - c_{s,j})c_{s,j}(c_{l,j}/c_{l,j,ref})}, \quad (7.7)$$

here κ_j is the temperature-dependent reaction rate constant, and solid and solution phase concentrations are $c_{s,j}$ and $c_{l,j}$, respectively. The solution phase concentration is assumed to be a constant value and $c_{l,j,ref}$ is assumed to be equal to 1 mol/m³. The overpotential for each electrode is related to the solid phase potential ($\phi_{s,j}$), the solution phase potential ($\phi_{l,j}$), and the open circuit potential (U_j) as

$$\eta_j = \phi_{s,j} - \phi_{l,j} - U_j. \quad (7.8)$$

The equilibrium potential of the electrode material is a function of the battery's state of charge (SOC), while the SOC is defined as the local Li ion concentration divided by the maximum intercalable Li ion concentration as

$$SOC = \frac{c_{s,j}}{c_{s,j,max}}, \quad (7.9)$$

where c_s and $c_{s,j,max}$ are the surface and maximum concentration of Li ions in the electrode particles, respectively. Figure 7.2 shows that the equilibrium potential parameter $E_{eq,j}$ for the graphite and LiCoO₂ as the negative and positive electrodes, respectively.

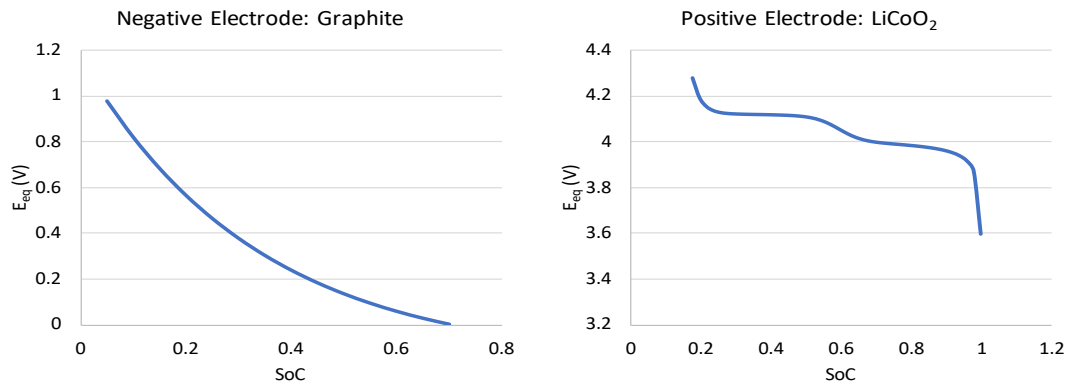


Figure 7.2 Equilibrium potential vs. SOC for Graphite and LiCoO₂ [45][114].

The potential drop at the electrode/electrolyte interface for solid polymer electrolyte (SPE) is related to the electrolyte resistance, R_{SPE} and applied current, I_{app} as

$$\varphi_{l,p} - \varphi_{l,n} = -I_{app}R_{SPE}, \quad (7.10)$$

here, R_{SPE} is an adjustable parameter that depends on the cell temperature, current, and the electrolyte type as

$$R_{SPE} = R_0(1 + \alpha(T_{amb} - T)), \quad (7.11)$$

where R_0 is the solid polymer electrolyte internal resistance, T is the temperature and α is the correction factor for the actual resistance of the electrolyte. The cell potential is determined as follow

$$E_{cell} = \varphi_{s,p} - \varphi_{s,n}. \quad (7.12)$$

7.2.2 The Thermal Energy Balance

The one dimensional thermal energy balance in Li-ion battery is governed by [45][224][231][232][233]

$$\rho_j C_{p,j} \frac{\partial T}{\partial t} = \lambda_j \frac{\partial^2 T}{\partial x^2} + q, \quad (7.13)$$

where λ_j is the thermal conductivity ($W m^{-1} K^{-1}$), $C_{p,j}$ is the heat capacity ($J kg^{-1} K^{-1}$), and ρ_j is the material density (kg/m^3). The heat source, q during charge and discharge processes in the Li-ion battery is defined as

$$q = Q_{rxn} + Q_{rev} + Q_{ohm}, \quad (7.14)$$

where Q_{rxn} is the total reaction heat generation rate, Q_{rev} is the total reversible heat generation rate, and Q_{ohm} is the total ohmic heat generation rate and are defined as

$$Q_{rxn} = FA_j J_j (\varphi_s - \varphi_l - U), \quad (7.15)$$

$$Q_{rev} = FA_j J_j T \left(\frac{\partial U}{\partial T} \right), \quad (7.16)$$

and

$$Q_{ohm} = \sigma_{eff} \left(\frac{\partial \varphi_s}{\partial x} \right)^2 + \kappa_{eff} \left(\frac{\partial \varphi_l}{\partial x} \right)^2, \quad (7.17)$$

where ohmic heat generation can also be defined as

$$Q_{ohm} = I_{app}^2 R_{SPE}. \quad (7.18)$$

The open circuit potential of electrode is temperature dependent and can be approximated by Taylor's first order expansion around a reference temperature as

$$U_j = U_{j,ref} + (T - T_{ref}) \frac{dU_j}{dT}, \quad (7.19)$$

where $U_{j,ref}$ is the open circuit potential under the reference temperature T_{ref} . The boundary condition for energy balance is expressed as

$$-\lambda_j \frac{\partial T}{\partial x} \Big|_{x=0} = h(T_{amb} - T), \quad (7.20)$$

and

$$-\lambda_j \frac{\partial T}{\partial x} \Big|_{x=L} = h(T - T_{amb}), \quad (7.21)$$

where h is convective heat transfer coefficient ($\text{Wm}^{-2}\text{K}^{-1}$), and T_{amb} is the absolute ambient temperature (K).

7.3 Results and Discussion

The voltage versus discharge capacity plots obtained from simulation are compared with experimental measurements and reported in Figure 7.3. The modeling results show a good agreement against the experimental measurements. The potential vs. discharge capacity for each temperature shows a sharp voltage drop for low temperatures at the early stages. This voltage drop is significant for 4°C compared to 10°C and 25°C which indicates the battery capacity decreases dramatically at low temperatures. The voltage drop can be

related to internal resistance of solid polymer electrolyte that plays a significant role in battery performance. The higher value of internal resistance in solid polymer electrolyte leads to lower ionic conductivity due to dominating the crystalline segment of the PEO matrix. The ionic conductivity of polymer electrolytes directly depends on the operating temperature and polymer glass transition temperature.

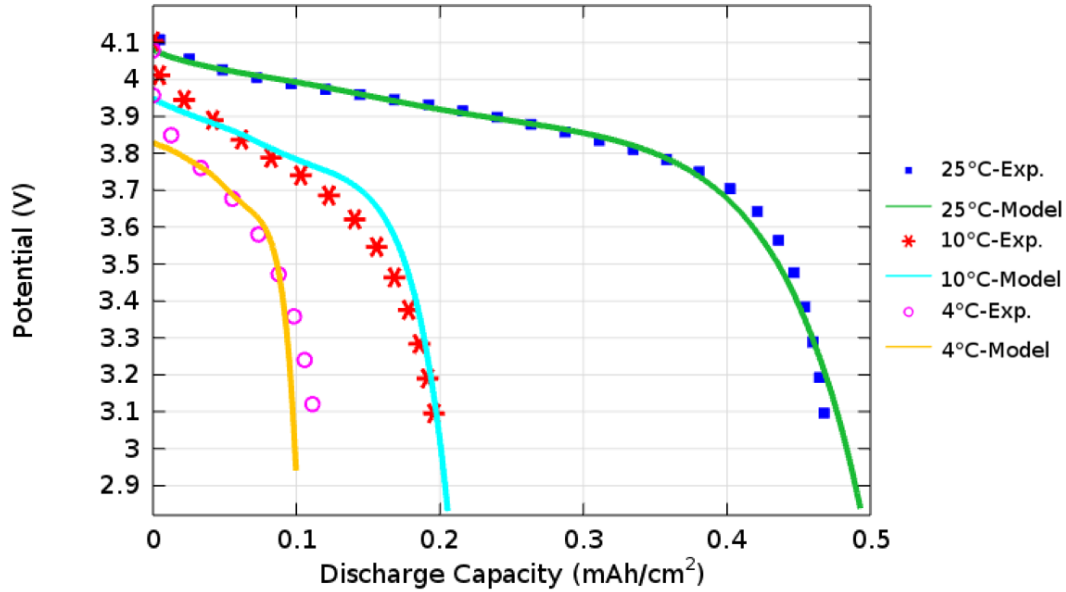


Figure 7.3 Potential (V) vs. discharge capacity (mAh/cm²) through both modeling and experimental measurements. The model can predict the battery performance in low temperatures.

The internal resistance is determined through simulation as a fitting parameter for each temperature. For battery at 4°C, this value is determined to be about 100 mΩ.m² while at 10°C it is about 60 mΩ.m². The internal resistance of the solid polymer electrolyte at room temperature is determined to be about 20 mΩ.m² which is 5 times lower than resistance at 4°C. The simulated cell temperature profiles during discharge process starting at 25°C for different operating temperatures are presented in Figure 7.4.

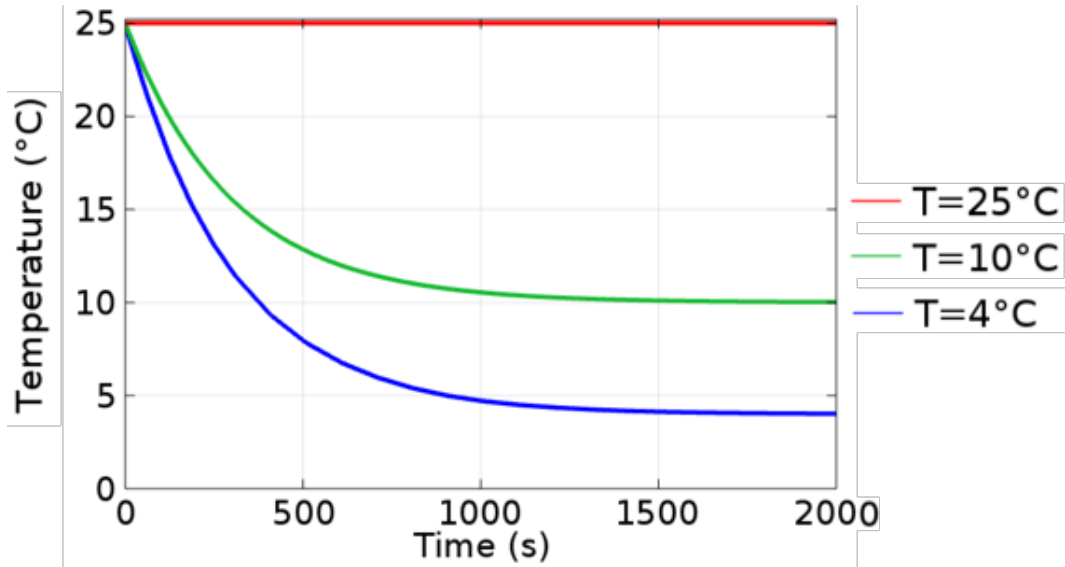


Figure 7.4 Temperature profile for 4°C, 10°C, and 25°C.

Through modeling, it is concluded that the battery performance at low temperatures can be improved by increasing the Li ion salt concentration in negative electrode. Figure 7.5 indicates that the battery performance at 4°C that is enhanced by 10%, 20%, and 30% increase of salt concentration. Higher salt concentration can boost ionic conductivity and reduce the resistance of polymer at lower temperatures.

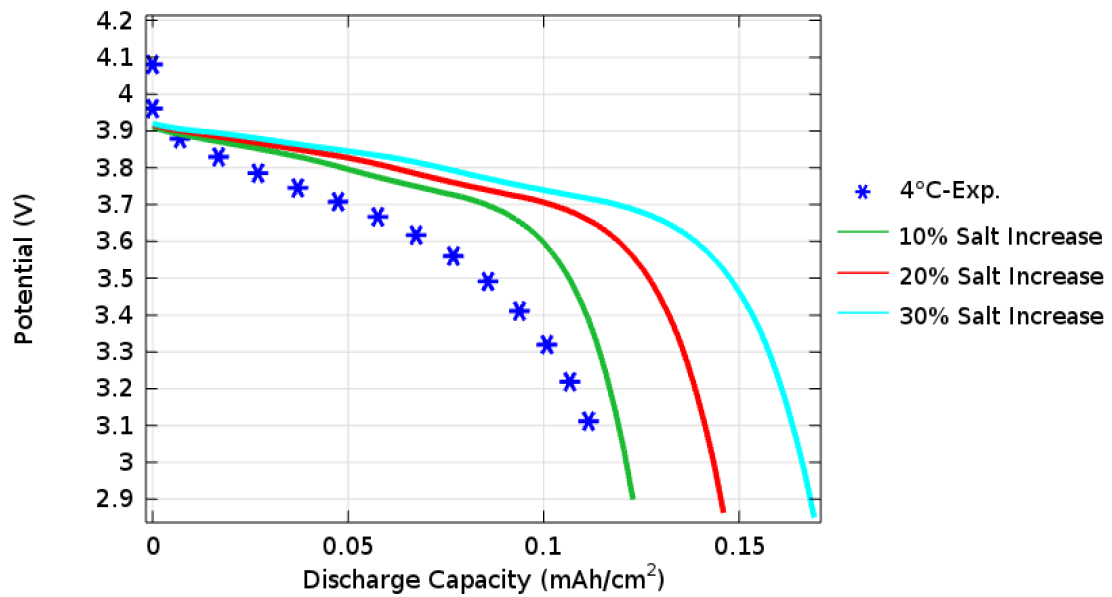


Figure 7.5 Modeling shows by increasing salt concentration in negative electrode the battery performance can be improved at 4°C.

7.4 Conclusions

In this study, a 1D thermo-electrochemical model is developed to investigate the effect of low temperatures on solid polymer electrolyte Li-ion batteries for subsea and space applications. The modeling results show a good agreement with experimental data. It is shown that by increasing the salt concentration in the negative electrode, the battery performance enhances at low temperatures. Some of the parameters such as concentration of Li ions and resistance of solid polymer electrolyte at low temperatures are estimated based on experimental measurements and adjusted in the model. An accurate estimation of these parameters is crucial for model accuracy and reliability. However, the parametric study helps battery designers to understand the effect of various parameters on battery performance in different operating conditions. The insights from this study enable a more effective design and fabrication of solid polymer electrolyte with enhanced electrochemical properties for flexible and structural Li-ion batteries and energy storage devices.

8 Conclusions and Future Work

8.1 Conclusions

8.1.1 Layered Nanostructure Modeling

In this study, two-dimensional models have been developed to investigate the effect of material architecture on ionic diffusivity for layered nanostructure composites. The focus of this study is specifically on composite material consisting of reduced graphene oxide (rGO) with 25wt% aramid nanofiber (ANF). The model considers two experimentally realizable aligned and staggered arrangements of rGO sheets in ANF matrix. Also, various degrees of rGO sheets' waviness are considered to mimic the structure of material depicted through SEM images. The results show that the waviness impedes the ionic diffusivity in both arrangements. However, this effect is more significant in staggered arrangement than in aligned arrangement. The effective diffusivity and tortuosity of each arrangement agrees with the aforementioned conclusion.

Architecture based diffusion analysis can provide a more rigorous approach to assess and screen various composite electrode structures. In comparison with porous media modeling that ignores material architecture and MD simulation that narrows the focus on localized properties of the material at atomic and molecular levels, architecture-based study is a good strategy to investigate micro and nano structure of composite materials in the field of supercapacitors and Li-ion batteries. The insights from this study enable a more effective design of electrode architectures toward enhanced ion diffusion and conductivity in electrochemical energy storage devices.

8.1.2 Nanoarchitecture Modeling vs. Porous Electrode Theory

In this study, the effective diffusion coefficient of K^+ and OH^- are obtained through nanoarchitecture modeling and compared with porous media approaches and validated with experimental measurements. The effect of nanoarchitectures of rGO/ANF composite electrodes obtained through sol-gel method called “house of cards” and vacuum filtration method called “layered” on effective diffusion coefficient is investigated through multiphysics computational modeling. Two unit-cells are developed with different arrangements of rGO/ANF sheets in square and staggered configurations to describe house of cards and layered nanostructures, respectively. The D_{eff} calculated from nanoarchitecture modeling is in a better agreement with experimental measurements. It is concluded that the porous media approach overestimates the value of D_{eff} for materials with high porosity. Modeling composite materials with high porosity requires more rigorous models that can be obtained through nanoarchitecture modeling.

8.1.3 Simulation of Cyclic Voltammetry

The modeling of structural supercapacitors is concluded by modeling the cyclic voltammetry measurements of a whole cell supercapacitor. The structural supercapacitor is made of two identical rGO/ANF electrodes and KOH electrolyte. The cyclic voltammetry of rGO/ANF structural supercapacitor is simulated various electrode kinetics such as Butler-Volmer equation and Tafel equation with very low local current density. However, the cyclic voltammetry behavior of rGO/ANF supercapacitor is similar to the ideal supercapacitor CV behavior. The modeling results show a very good agreement with experimental measurements. Modeling cyclic voltammetry can provide useful information about kinetics and thermodynamics of structural supercapacitors and enables better control

over the performance and life cycle of the device. Comparison of predicted and measured voltammograms enables determination of unknown material properties such as diffusion coefficients and reaction rates.

8.1.4 Thermal Modeling of Solid Polymer Li-Ion Batteries

In this study, the effect of low temperatures on solid polymer electrolyte Li-ion batteries is investigated through modeling and the results validated with experimental measurements. The modeling results show a very good agreement with experimental measurements. It is also predicted that increasing the Li-ion salt concentration at the negative electrode by 10 to 30 percent improves the battery performance considerably. However, more accurate experimental measurements are required to estimate fitting parameters to ensure the model reliability and accuracy. The insights from this study enable a more effective design and fabrication of solid polymer electrolyte with enhanced electrochemical properties for flexible and structural Li-ion batteries and energy storage devices.

8.2 Future Work

8.2.1 Nanoarchitecture Modeling

In nanoarchitecture modeling, assuming that the structure is consistent along the third dimension, 2D modeling is more efficient than 3D modeling. However, for cases when there are some variabilities in the third dimension, 3D modeling can provide more accurate information about the material behavior. The 3D modeling should be considered in the future work to provide more accurate value of D_{eff} in the composite materials. Also, a more rigorous 2D and 3D models that mimics the SEM images can provide a system to

calculate and determine the effective diffusion coefficient for electrode materials with various nanoarchitectures.

8.2.2 Cyclic Voltammetry Modeling

The CV modeling can be used to simulate cyclic voltammetry of house of cards nanostructure as well as other electrode materials. The CV plot provide very useful information about the material electrochemical behavior. The voltage, current density and concentration profile for each nanostructure can be compared with experimental measurements. Modeling long and multiple voltammetric cycles can be performed. Various nonstandard voltage waveforms (other than triangular wave) can be applied at the interface and a predictive simulation can be achieved. Coupling to a fluid flow model with convection of the reacting species allows the investigation of hydrodynamic electrochemistry.

8.2.3 Thermal Effect on Li-Ion Batteries

Thermal behaviors, operating conditions, and heat generation during charge and discharge play important roles on electrochemical energy storage performance, lifetime, reliability, and safety. To investigate the solid polymer electrolyte performance in different conditions, a wider range of temperatures can be considered in the modeling thermal effect of Li-ion batteries. Modeling Li-ion batteries in extreme cold and hot temperatures combined with radiation effect can be very interesting in applications such as space and subsea. Various parametric studies can help rational material design with preferred specification for different applications. The model can be modified to provide more predictive results for the situations that the experiment is not possible.

References

- [1] J. B. Goodenough, H. D. Abruna, M. V. Buchanan, “Basic Research Needs for Electric Energy Storage: Report of the Basic Energy Sciences Workshop on Electrical Energy Storage,” *U.S. Department of Energy, Office of Basic Energy Sciences*, Washington, DC, 2007.
- [2] A. A. Hoffmann, C. M. Sgro, “Climate Change and Evolutionary Adaptation,” *Nature*, 470 (2011) 479–485.
- [3] C. Parmesan, G. Yohe, “A Globally Coherent Fingerprint of Climate Change Impacts Across Natural Systems,” *Nature*, 421 (2003) 37–42.
- [4] T. Kousksou, P. Bruel, A. Jamil, T. ElRhafiki, Y. Zeraouli, “Energy Storage: Applications and Challenges,” *Solar Energy Materials & Solar Cells*, 120 (2014) 59–80.
- [5] R. M. Dell, D. A. J. Rand, “Energy Storage –A Key Technology for Global Energy Sustainability,” *Journal of Power Sources*, 100 (2001) 2–17.
- [6] N.-S. Choi, Z. Chen, S. A. Freunberger, X. Ji, Y.-K. Sun, K. Amine, G. Yushin, L. F. Nazar, J. Cho, P. G. Bruce, “Challenges Facing Lithium Batteries and Electrical Double-Layer Capacitors,” *Angew. Chem. Int.*, 51 (2012) 9994 – 10024.
- [7] B. E. Conway, *Electrochemical Supercapacitors: Scientific Fundamentals and Technological Applications*. Kluwer Academic Plenum, New York, 1999.
- [8] A. S. Arico, P. Bruce, B. Scrosati, J. M. Tarascon, and W. V. Schalkwijk, “Nanostructured Materials for Advanced Energy Conversion and Storage Devices,” *Nature Materials*, 4 (2005) 366–377.
- [9] T. Pereira, Z. Guo, S. Nieh, J. Arias, H. Thomas Hahn, “Energy Storage Structural

- Composites: A Review,” *Journal of Composite Materials*, 43 (2009) 549–560.
- [10] N. Shirshova, H. Qian, M. Houllé, J. H. G. Steinke, A. R. J. Kucernak, Q. P. V. Fontana, E. S. Greenhalgh, A. Bismarck, M. S. P. Shaffer, “Multifunctional Structural Energy Storage Composite Supercapacitors,” *Faraday Discussions*, 172 (2014) 81–103.
- [11] E. Pomerantseva, Y. Gogotsi, “Two-Dimensional Heterostructures for Energy Storage,” *Nature Energy*, 2 (2017) 17089.
- [12] Y. Lin, H. A. Sodano, “Characterization of Multifunctional Structural Capacitors for Embedded Energy Storage,” *J. Appl. Phys.*, 106 (2009) 114108.
- [13] S. W. Lee, B. M. Gallant, H. R. Byon, P. T. Hammond, Y. Shao-Horn, “Nanostructured Carbon-Based Electrodes: Bridging the Gap between Thin-Film Lithium-Ion Batteries and Electrochemical Capacitors,” *Energy Environ. Sci.*, 4 (2011) 1972–1985.
- [14] Y. Zhang, W. Bai, X. Cheng, J. Ren, W. Weng, P. Chen, X. Fang, Z. Zhang, H. Peng, “Flexible and Stretchable Lithium-Ion Batteries and Supercapacitors Based on Electrically Conducting Carbon Nanotube Fiber Springs,” *Angew. Chem. Int.*, 53 (2014) 14564–14568.
- [15] S. Kwon, M. B. Elinski, J. D. Batteas, J. L. Lutkenhaus, “Robust and Flexible Aramid Nanofiber/Graphene Layer-by-Layer Electrodes,” *ACS Appl. Mater. Interfaces*, 9 (2017) 17125–17135.
- [16] S. Kwon, J. Harris, T. Zhou, D. Loufakis, J. L. Lutkenhaus, “Mechanically Strong Graphene/Aramid Nanofiber Composite Electrodes for Structural Energy and Power,” *ACS Nano*, 11 (2017) 6682–6690.
- [17] P. Flouda, X. Feng, J. G. Boyd, E. L. Thomas, D. C. Lagoudas, J. L. Lutkenhaus,

- “Interfacial Engineering of Reduced Graphene Oxide for Aramid Nanofiber-Enabled Structural Supercapacitors,” *Batteries & Supercaps*, 2 (2019) 464–472.
- [18] P. Flouda, S. A. Shah, D. C. Lagoudas, M. J. Green, J. L. Lutkenhaus, “Highly Multifunctional Dopamine Functionalized Reduced Graphene Oxide Supercapacitors,” *Matter*, 1 (2019) 1–15.
- [19] S. A. Shah, D. Kulhanek, W. Sun, X. Zhao, S. Yu, D. Parviz, J. L. Lutkenhaus, M. J. Green, “Aramid Nanofiber-Reinforced Three-Dimensional Graphene Hydrogels for Supercapacitor Electrodes,” *Journal of Colloid and Interface Science*, 560 (2020) 581–588.
- [20] M. Winter, R. J. Brodd, “What Are Batteries, Fuel Cells, and Supercapacitors?” *Chem. Rev.*, 104 (2004) 4245–4269.
- [21] P. Simon, Y. Gogotsi, B. Dunn, “Where Do Batteries End and Supercapacitors Begin?” *Science*, 343 (2014) 1210–1211.
- [22] A. Burke, “Ultracapacitors: Why, How, and Where Is the Technology,” *Journal of Power Sources*, 91 (2000) 37–50.
- [23] T. Christen, M. W. Carlen, “Theory of Ragone Plots,” *Journal of Power Sources*, 91 (2000) 210–216.
- [24] R. Kotz, M. Carlen, “Principles and Applications of Electrochemical Capacitors,” *Electrochimica Acta*, 45 (2000) 2483–2498.
- [25] J. Yan, Q. Wang, T. Wei, Z. Fan, “Recent Advances in Design and Fabrication of Electrochemical Supercapacitors with High Energy Densities,” *Adv. Energy Mater.*, 4 (2014) 1300816.
- [26] T. Christen, C. Ohler, “Optimizing Energy Storage Devices Using Ragone Plots,”

Journal of Power Sources, 110 (2002) 107–116.

- [27] R. Mukherjee, R. Krishnan, T.-M. Lu, N. Koratkar, “Nanostructured Electrodes for High-Power Lithium-Ion Batteries,” *Nano Energy*, 1 (2012) 518–533.
- [28] B. J. Landi, C. D. Cress, R. P. Raffaele, “High Energy Density Lithium-Ion Batteries with Carbon Nanotube Anodes,” *J. Mater. Res.*, 25 (2010) 1636–1644.
- [29] J. W. Choi, D. Aurbach, “Promise and Reality of Post-Lithium-Ion Batteries with High Energy Densities,” *Nature Reviews Materials*, 1 (2016) 16013.
- [30] X. Fang, M. Ge, J. Rong, C. Zhou, “Graphene-Oxide-Coated $\text{LiNi}_{0.5}\text{Mn}_{1.5}\text{O}_4$ as High Voltage Cathode for Lithium-Ion Batteries with High Energy Density and Long Cycle Life,” *J. Mater. Chem. A*, 1 (2013) 4083–4088.
- [31] H. Yoshizawa, T. Ohzuku, “An Application of Lithium Cobalt Nickel Manganese Oxide to High-Power and High-Energy Density Lithium-Ion Batteries,” *Journal of Power Sources*, 174 (2007) 813–817.
- [32] G. Zhou, F. Li, H.-M. Cheng, “Progress in Flexible Lithium Batteries and Future Prospect,” *Energy Environ. Sci.*, 7 (2014) 1307–1338.
- [33] Q. Li, H. Ardebili, “Flexible Thin-Film Battery Based on Solid-Like Ionic Liquid-Polymer Electrolyte,” *Journal of Power Sources*, 303 (2016) 17–21.
- [34] M. Kammoun, S. Berg, H. Ardebili, “Flexible Thin-Film Battery Based on Graphene-Oxide Embedded in Solid Polymer Electrolyte,” *Nanoscale*, 7 (2015) 17516.
- [35] S.-H. Kim, K.-H. Choi, S.-J. Cho, E.-H. Kil, S.-Y. Lee, “Mechanically Compliant and Lithium Dendrite Growth-Suppressing Composite Polymer Electrolytes for Flexible Lithium-Ion Batteries,” *J. Mater. Chem. A*, 1 (2013) 4949–4955.
- [36] X. Peng, L. Peng, C. Wu, Y. Xie, “Two Dimensional Nanomaterials for Flexible

- Supercapacitors,” *Chem. Soc. Rev.*, 43 (2014) 3303–3323.
- [37] Z. Weng, Y. Su, D.-W. Wang, F. Li, J. Du, H.-M. Cheng, “Graphene–Cellulose Paper Flexible Supercapacitors,” *Adv. Energy Mater.*, 1 (2011) 917–922.
- [38] G. Ceder, M. Doyle, P. Arora, Y. Fuentes, “Computational Modeling and Simulation for Rechargeable Batteries,” *Portable Power: Advanced Rechargeable Lithium Batteries*, 27 (2002) 619–623.
- [39] A. Wang, S. Kadam, H. Li, S. Shi, Y. Qi, “Review on Modeling of the Anode Solid Electrolyte Interphase (SEI) for Lithium-Ion Batteries,” *NPJ. Comput. Mater.*, 4 (2018) 1–26.
- [40] L. Zhang, X. Hu, Z. Wang, F. Sun, D. G. Dorrell, “A Review of Supercapacitor Modeling, Estimation, and Applications: A Control/Management Perspective,” *Renewable and Sustainable Energy Reviews*, 81 (2018) 1868–1878.
- [41] N. Devillers, S. Jemei, M.-C. Péra, D. Bienaimé, F. Gustin, “Review of Characterization Methods for Supercapacitor Modelling,” *Journal of Power Sources*, 246 (2014) 596–608.
- [42] Multiphysics, COMSOL. Introduction to COMSOL Multiphysics®. 1998.
- [43] R. W. Pryor, *Multiphysics Modeling Using COMSOL: A First Principles Approach*. Jones & Bartlett Learning: Sudbury, MA, 2011.
- [44] E. J. F. Dickinson, H. Ekström, E. Fontes, “COMSOL Multiphysics®: Finite Element Software for Electrochemical Analysis. A Mini-Review,” *Electrochemistry Communications*, 40 (2014) 71–74.
- [45] L. Cai, R. E. White, “Mathematical Modeling of a Lithium-Ion Battery with Thermal Effects in COMSOL Inc. Multiphysics (MP) Software,” *Journal of Power*

- Sources*, 196 (2011) 5985–5989.
- [46] I. J. Cutress, E. J. F. Dickinson, R. G. Compton, “Analysis of Commercial General Engineering Finite Element Software in Electrochemical Simulations,” *Journal of Electroanalytical Chemistry*, 638 (2010) 76–83.
- [47] P. Simon, Y. Gogotsi, “Materials for Electrochemical Capacitors,” *Nature Mater.*, 7 (2008) 845–854.
- [48] E. Frackowiak, “Carbon Materials for Supercapacitor Application,” *Chem. Phys.*, 9 (2007) 1774–1785.
- [49] B. You, J. Jiang, S. Fan, “Three-Dimensional Hierarchically Porous All-Carbon Foams for Supercapacitor,” *ACS Appl. Mater. Interfaces*, 6 (2014) 15302–15308.
- [50] D. Qu, “Studies of the Activated Carbons Used in Double-Layer Supercapacitors,” *Journal of Power Sources*, 109 (2002) 403–411.
- [51] W. S. Hummers, R. E. Offeman, “Preparation of Graphitic Oxide,” *J. Am. Chem. Soc.*, 80 (1958) 1339–1339.
- [52] M. D. Stoller, S. Park, Y. Zhu, J. An, R. S. Ruoff, “Graphene Based Ultracapacitors,” *Nano Lett.*, 8 (2008) 3498–3502.
- [53] L. L. Zhang, R. Zhou, X. S. Zhao, “Graphene Based Materials as Supercapacitor Electrodes,” *J. Mater. Chem.*, 20 (2010) 5983–5992.
- [54] D. A. C. Brownson, D. K. Kampouris, C. E. Banks, “An Overview of Graphene in Energy Production and Storage Applications,” *J. Power Sources*, 196 (2011) 4873–4885.
- [55] L. Ji, P. Meduri, V. Agubra, X. Xiao, M. Alcoutlabi, “Graphene Based Nanocomposites for Energy Storage,” *Advanced Energy Materials*, 6 (2016) 1502159.
- [56] M. Wang, L. D. Duong, N. T. Mai, S. Kim, Y. Kim, H. Seo, Y. C. Kim, W. Jang,

- Y. Lee, J. Suhr, J.-D. Nam, “All-Solid-State Reduced Graphene Oxide Supercapacitor with Large Volumetric Capacitance and Ultra-long Stability Prepared by Electrophoretic Deposition Method,” *ACS Appl. Mater. Interfaces*, 7 (2015) 1348–1354.
- [57] U. N. Maiti, J. Lim, K. E. Lee, W. J. Lee, S. O. Kim, “Three-Dimensional Shape Engineered, Interfacial Gelation of Reduced Graphene Oxide for High Rate, Large Capacity Supercapacitors,” *Adv. Mater.*, 26 (2014) 615–619.
- [58] L. L. Zhang, S. Zhao, X. N. Tian, X. S. Zhao, “Layered Graphene Oxide Nanostructures with Sandwiched Conducting Polymers as Supercapacitor Electrodes,” *Langmuir*, 26 (2010) 17624–17628.
- [59] G. Eda, G. Fanchini, M. Chhowalla, “Large-Area Ultrathin Films of Reduced Graphene Oxide as a Transparent and Flexible Electronic Material,” *Nature Nanotechnology*, 3 (2008) 270–274.
- [60] J. Fan, Z. Shi, L. Zhang, J. Wang, J. Yin, “Aramid Nanofiber-Functionalized Graphene Nanosheets for Polymer Reinforcement,” *Nanoscale*, 4 (2012) 7046–7055.
- [61] J. Fan, Z. Shi, M. Tian, J. Yin, “Graphene-Aramid Nanofiber Nanocomposite Paper with High Mechanical and Electrical Performance,” *RSC Adv.*, 3 (2013) 17664–17667.
- [62] L. Jianhua, A. Junwei, Z. Yecheng, M. Yuxiao, L. Mengliu, Y. Mei, L. Songmei, “Preparation of an Amide Group-Connected Graphene–Polyaniline Nanofiber Hybrid and Its Application in Supercapacitors,” *ACS Appl. Mater. Interfaces*, 4 (2012) 2870–2876.
- [63] A. Junwei, J. Liu, Y. Zhou, H. Zhao, Y. Ma, M. Li, M. Yu, S. Li, “Polyaniline-Grafted Graphene Hybrid with Amide Groups and Its Use in Supercapacitors,” *J. Phys. Chem. C*, 116 (2012) 19699–19708.
- [64] J. Fan, Z. Shi, L. Zhang, J. Wang, J. Yin, “Aramid Nanofiber-Functionalized

- Graphene Nanosheets for Polymer Reinforcement,” *Nanoscale*, 4 (2012) 7046–7055.
- [65] B. Park, W. Lee, E. Lee, S. H. Min, B. Kim, “Highly Tunable Interfacial Adhesion of Glass Fiber by Hybrid Multilayers of Graphene Oxide and Aramid Nanofiber,” *ACS Appl. Mater. Interfaces*, 7 (2015) 3329–3334.
- [66] D. Tanner, J. A. Fitzgerald, B. R. Phillips, “The Kevlar Story-An Advanced Materials Case Study,” *Angew. Chem., Int. Ed. Engl.*, 28 (1989) 649–654.
- [67] M. Yang, K. Cao, L. Sui, Y. Qi, J. Zhu, A. Waas, E. M. Arruda, J. Kieffer, M. D. Thouless, N. A. Kotov, “Dispersions of Aramid Nanofibers: A New Nanoscale Building Block,” *ACS Nano*, 5 (2011) 6945–6954.
- [68] K. Cao, C. P. Siepermann, M. Yang, A. M. Waas, N. A. Kotov, M. D. Thouless, E. M. Arruda, “Reactive Aramid Nanostructures as High-Performance Polymeric Building Blocks for Advanced Composites,” *Adv. Funct. Mater.*, 23 (2013) 2072–2080.
- [69] S. O. Tung, S. Ho, M. Yang, R. Zhang, N. A. Kotov, “A Dendrite-Suppressing Composite Ion Conductor from Aramid Nanofibres,” *Nat. Commun.*, 6 (2015) 6152.
- [70] S. W. Lee, B. S. Kim, S. Chen, Y. Shao-Horn, P. T. Hammond, “Layer-by-Layer Assembly of All Carbon Nanotube Ultrathin Films for Electrochemical Applications,” *J. Am. Chem. Soc.*, 131 (2009) 671–679.
- [71] M. A. Worsley, P. J. Pauzauskie, T. Y. Olson, J. Biener, J. H. Satcher, Jr., T. F. Baumann, “Synthesis of Graphene Aerogel with High Electrical Conductivity,” *J. Am. Chem. Soc.*, 132 (2010) 14067–14069.
- [72] D. Parviz, S. D. Metzler, S. Das, F. Irin, M. J. Green, “Tailored Crumpling and Unfolding of Spray-Dried Pristine Graphene and Graphene Oxide Sheets,” *Small*, 11 (2015) 2661–2668.

- [73] Y. Xu, K. Sheng, C. Li, G. Shi, "Self-Assembled Graphene Hydrogel via a One-Step Hydrothermal Process," *ACS Nano*, 4 (2010) 4324–4330.
- [74] W. Chen, L. Yan, "In Situ Self-Assembly of Mild Chemical Reduction Graphene for Three-Dimensional Architectures," *Nanoscale*, 3 (2011) 3132–3137.
- [75] M. Okamoto, P. H. Nam, P. Maiti, T. Kotaka, N. Hasegawa, A. Usuk, "A House of Cards Structure in Polypropylene/Clay Nanocomposites under Elongational Flow," *Nano Lett.*, 1 (2001) 295–298.
- [76] X. Jin, K. Adpakpang, I. Y. Kim, S. M. Oh, N.-S. Lee, S.-J. Hwang, "An Effective Way to Optimize the Functionality of Graphene-Based Nanocomposite: Use of the Colloidal Mixture of Graphene and Inorganic Nanosheets," *Scientific Reports*, 5 (2015) 11057.
- [77] J. D. Mangadlao, K. J. Lim, C. Danda, M. L. Dalida, R. C. Advincula, "House of Cards Nanostructuring of Graphene Oxide and Montmorillonite Clay for Oil-Water Separation," *Macromol. Mater. Eng.*, 303 (2018) 1700314.
- [78] B. Pillay, J. Newman, "The Influence of Side Reactions on the Performance of Electrochemical Double-Layer Capacitors," *J. Electrochem. Soc.*, 143 (1996) 1806–1814.
- [79] S. A. Kazaryan, S. N. Razumov, S. V. Litvinenko, G. G. Kharisov, V. I. Kogan, "Mathematical Model of Heterogeneous Electrochemical Capacitors and Calculation of Their Parameters," *J. Electrochem. Soc.*, 153 (2006) A1655–A1671.
- [80] A. M. Johnson, J. Newman, "Desalting by Means of Porous Carbon Electrodes," *J. Electrochem. Soc.*, 118 (1971) 510–517.
- [81] F. A. Posey, T. Morozumi, "Theory of Potentiostatic and Galvanostatic Charging of the Double Layer in Porous Electrodes," *J. Electrochem. Soc.*, 113 (1966) 176–184.

- [82] W. Tiedemann, J. Newman, "Double-Layer Capacity Determination of Porous Electrodes," *J. Electrochem. Soc.*, 122 (1975) 70–74.
- [83] D. Dunn, J. Newman, "Predictions of Specific Energies and Specific Powers of Double-Layer Capacitors Using a Simplified Model," *J. Electrochem. Soc.*, 147 (2000) 820–830.
- [84] R. Li, H. Cheng, Y. Su, S.-W. Hwang, L. Yin, H. Tao, M. A. Brenckle, D.-H. Kim, F. G. Omenetto, J. A. Rogers, Y. Huang, "An Analytical Model of Reactive Diffusion for Transient Electronics," *Adv. Functional Mater.*, 23 (2013) 3106–3114.
- [85] Y. Joliff, L. Belec, J. F. Chailan, "Modified Water Diffusion Kinetics in Unidirectional Glass/Fiber Composite Due to the Interphase Area: Experimental, Analytical and Numerical Approach," *Composite Structures*, 97 (2013) 296–303.
- [86] J. B. Yang, T. P. Chen, S. S. Tan, L. Chan, "Analytical Reaction-Diffusion Model and the Modeling of Nitrogen-Enhanced Negative Bias Temperature Instability," *Applied Physics Letters*, 88 (2006) 172109.
- [87] P. Yu, B. N. Popov, J. A. Ritter, R. E. White, "Determination of the Lithium-Ion Diffusion Coefficient in Graphite," *J. Electrochem. Soc.*, 146 (1999) 8–14.
- [88] H. Kahlert, U. Retter, H. Lohse, K. Siegler, F. Scholz, "On the Determination of the Diffusion Coefficients of Electrons and of Potassium Ions in Copper (II) Hexacyanoferrate (II) Composite Electrodes," *J. Phys. Chem. B*, 102 (1998) 8757–8765.
- [89] S.-H. Kim, W. Choi, K.-B. Lee, S. Choi, "Advanced Dynamic Simulation of Supercapacitors Considering Parameter Variation and Self-Discharge," *IEEE Transactions on Power Electronics*, 26 (2011) 3377–3385.
- [90] S. Buller, M. Thele, R.W.A.A. De Doncker, E. Karden, "Impedance-Based

Simulation Models of Supercapacitors and Li-Ion Batteries for Power Electronic Applications,” *IEEE Transactions on Industry Applications*, 41 (2005) 742–747.

[91] C. Lin, B. N. Popov, H. J. Ploehn, “Modeling the Effects of Electrode Composition and Pore Structure on the Performance of Electrochemical Capacitors,” *J. Electrochem. Soc.*, 149 (2002) A167–A175.

[92] M. W. Verbrugge, P. Ping Liu, “Microstructural Analysis and Mathematical Modeling of Electric Double-Layer Supercapacitors,” *J. Electrochem. Soc.*, 152 (2005) D79–D87.

[93] V. Srinivasan, J. W. Weidner, “Mathematical Modeling of Electrochemical Capacitors,” *J. Electrochem. Soc.*, 146 (1999) 1650–1658.

[94] H. Kim, B. N. Popov, “A Mathematical Model of Oxide/Carbon Composite Electrode for Supercapacitors,” *J. Electrochem. Soc.*, 150 (2003) A1153–A1160.

[95] C. Lin, J. A. Ritter, B. N. Popov, R. E. White, “A Mathematical Model of an Electrochemical Capacitor with Double-Layer and Faradaic Processes,” *J. Electrochem. Soc.*, 146 (1999) 3168–3175.

[96] D. Zhang, Q. Dong, X. Wang, W. Yan, W. Deng, L. Shi, “Preparation of a Three-Dimensional Ordered Macroporous Carbon Nanotube/Polypyrrole Composite for Supercapacitors and Diffusion Modeling,” *J. Phys. Chem. C*, 117 (2013) 20446–20455.

[97] M. Kaus, J. Kowa, D. S. Sauer, “Modeling the Effects of Charge Redistribution during Self-discharge of Supercapacitors,” *Electrochimica Acta*, 55 (2010) 7516–7523.

[98] I. J. Ong, J. Newman, “Double-Layer Capacitance in a Dual Lithium-Ion Insertion Cell,” *J. Electrochem. Soc.*, 146 (1999) 4360–4365.

[99] S. Kondrat, P. Wu, R. Qiao, A. A. Kornyshev, “Accelerating Charging Dynamics

in Subnanometer Pores,” *Nature Materials*, 13 (2014) 387–393.

[100] Y. Shim, Y. J. Jung, H. J. Kim, “Graphene-Based Supercapacitors: A Computer Simulation Study,” *J. Phys. Chem. C*, 115 (2011) 23574–23583.

[101] C. Pean, B. Daffos, B. Rotenberg, P. Levitz, M. Haefele, P.-L. Taberna, P. Simon, M. Salanne, “Confinement, Desolvation, and Electrosorption Effects on the Diffusion of Ions in Nanoporous Carbon Electrodes,” *J. Am. Chem. Soc.*, 137 (2015) 12627–12632.

[102] T. G. A. Youngs, C. Hardacre, “Application of Static Charge Transfer within an Ionic-Liquid Force Field and Its Effect on Structure and Dynamics,” *J. Chem. Phys. Chem.*, 9 (2008) 1548–1558.

[103] C. Merlet, A. C. Forse, J. M. Griffin, D. Frenkel, C. P. Grey, “Lattice Simulation Method to Model Diffusion and NMR Spectra in Porous Materials,” *J. Chem. Phys.*, 142 (2015) 094701.

[104] X. Tang, J. D. Whitcomb, Y. Li, H. J. Sue, “Micromechanics Modeling of Moisture Diffusion in Woven Composites,” *Composites Science and Technology*, 65 (2005) 817–826.

[105] E. L. Cussler, S. E. Hughes, W. J. Ward III, R. Aris, “Barrier Membranes,” *Journal of Membrane Science*, 38 (1988) 161–174.

[106] F. Korkees, S. Alston, C. Arnold, “Directional Diffusion of Moisture into Unidirectional Carbon Fiber/Epoxy Composites: Experiments and Modeling,” *Polymer Composites*, 39 (2018) E2306–E2315.

[107] S. Zid, M. Zinet, E. Espuche, “3D Mass Diffusion in Ordered Nanocomposite Systems: Finite Element Simulation and Phenomenological Modeling,” *J. Polym. Sci.*,

Part B: Polym. Phys., 57 (2019) 51–61.

- [108] S. Aderyani, P. Flouda, J. L. Lutkenhaus, H. Ardebili, “The Effect of Nanoscale Architecture on Ionic Diffusion in rGO/Aramid Nanofiber Structural Electrodes,” *Journal of Applied Physics*, 125 (2019) 185106.
- [109] S. L. Devadoss, J. O'Rourke, *Discrete and Computational Geometry*. Princeton University Press. Princeton, 2011; pp 128–129.
- [110] A. Gray, *Parallel Curves*. In *Modern Differential Geometry of Curves and Surfaces with Mathematica*. CRC Press, Boca Raton, 1997; pp 115–117.
- [111] J. D. A Lawrence, *Catalog of Special Plane Curves*. Dover, New York, 1972; pp 42–43.
- [112] R. C. Yates, *Parallel Curves*. *A Handbook on Curves and Their Properties*. J. W. Edwards, Ann Arbor, 1952; pp 155–159.
- [113] J. R. Sendra, F. Winkler, S. Pérez Díaz, *Rational Algebraic Curves: A Computer Algebra Approach*. Springer Science & Business Media, 2007; pp 10.
- [114] J. Newman, K. E. Thomas-Alyea, *Electrochemical Systems*. Wiley & Sons, New Jersey, 2004; pp 269–315.
- [115] A. J. Bard, L. R. Faulker, *Electrochemical Methods, Fundamentals and Applications*. Wiley and Sons, New Jersey, 2001; pp 137–153.
- [116] T. F. Fuller, J. N. Harb, *Electrochemical Engineering*. Wiley & Sons, New Jersey, 2018; pp 41–87.
- [117] J. Crank, *The Mathematics of Diffusion*. Oxford University, Bristol, England, 1975.
- [118] G. E. Bell, J. Crank, “Influence of Imbedded Particles on Steady-State Diffusion,”

J. Chem. Soc., Faraday Trans. II, 70 (1974) 1259–1273.

[119] B. M. Braun, H. Weingartner, “Accurate Self-Diffusion Coefficients of Li^+ , Na^+ , and Cs^+ Ions in Aqueous Alkali Metal Halide Solutions from NMR Spin-Echo Experiment,” *J. of Physical Chemistry*, 95 (1988) 1342–1346.

[120] K. Persson, V. A. Sethuraman, L. J. Hardwick, Y. Hinuma, Y. S. Meng, A. van der Ven, V. Srinivasan, R. Kosteck, G. Ceder, “Lithium Diffusion in Graphitic Carbon,” *J. Phys. Chem. Lett.*, 1 (2010) 1176–1180.

[121] C. Fărcaș, D. Petreus, I. Ciocan and N. Palaghiță, “Modeling and Simulation of Supercapacitors,” *15th Int. Symposium for Design and Technology of Electronics Packages*, (2009) 195–200.

[122] M. Forsyth, H. Yoon, F. Chen, H. Zhu, D. R. MacFarlane, M. Armand, P. C. Howlett, “Novel Na^+ Ion Diffusion Mechanism in Mixed Organic–Inorganic Ionic Liquid Electrolyte Leading to High Na^+ Transference Number and Stable, High Rate Electrochemical Cycling of Sodium Cells,” *J. Phys. Chem. C*, 120 (2016) 4276–4286.

[123] Z. Wang, A. P. Ratvik, T. Grande, S. M. Selbach, “Diffusion of Alkali Metals in the First Stage Graphite Intercalation Compounds by vdW-DFT Calculations,” *RSC Advances*, 5 (2015) 15985–15992.

[124] H. L. Yeager and B. Kipling, “Sodium Ion Diffusion in Nafion Ion Exchange Membranes,” *J. Electrochem. Soc.*, 127 (1980) 303–307.

[125] X. Zou, P. Xiong, J. Zhao, J. Hu, Z. Liu, Y. Xu, “Recent Research Progress in Non-Aqueous Potassium-Ion Batteries,” *Phys. Chem.*, 19 (2017) 26495–26506.

[126] M. Zuleta, P. Björnbom, A. Lundblad, “Effects of Pore Surface Oxidation on Electrochemical and Mass-Transport Properties of Nanoporous Carbon,” *J.*

- Electrochem. Soc.*, 152 (2005) A270–A276.
- [127] J. Ding, W. Hu, E. Paek, D. Mitlin, “Review of Hybrid Ion Capacitors: From Aqueous to Lithium to Sodium,” *Chem. Rev.*, 118 (2018) 6457–6498.
- [128] H. Ardebili, E. H. Wong, M. Pecht, “Hygroscopic Swelling and Sorption Characteristics of Epoxy Molding Compounds Used in Electronic Packaging,” *IEEE Transactions on Components and Packaging Technologies*, 26 (2003) 206–214.
- [129] L. Shen, Z. Chen, “Critical Review of the Impact of Tortuosity on Diffusion,” *Chemical Engineering Science*, 62 (2007) 3748–3755.
- [130] B. Tjaden, S. J. Cooper, D. J. L. Brett, D. Kramer, P. R. Shearing, “On the Origin and Application of the Bruggeman Correlation for Analyzing Transport Phenomena in Electrochemical Systems,” *Current Opinion in Chemical Engineering*, 12 (2016) 44–51.
- [131] R. J. Millington, J. P. Quirk, “Transport in Porous Media [in Soil Science],” *Trans. Int. Congr. Soil Sci.*, 7 (1961) 97–106.
- [132] R. J. Millington, J. P. Quirk, “Permeability of Porous Solids,” *Trans. Faraday Soc.*, 57, (1961) 1200–1207.
- [133] X. Zhang, D. M. Tartakovsky, “Effective Ion Diffusion in Charged Nanoporous Materials,” *Journal of The Electrochemical Society*, 164 (2017) E53–E61.
- [134] J. Zhang, Y. Xiang, M. I. Jamil, J. Lu, Q. Zhang, X. Zhan, F. Chen, “Polymers/Zeolite Nanocomposite Membranes with Enhanced Thermal and Electrochemical Performances for Lithium-Ion Batteries,” *Journal of Membrane Science*, 564 (2018) 753–761.
- [135] S. Aderyani, S. A. Shah, A. Masoudi, M. J. Green, J. L. Lutkenhaus, H. Ardebili, “Comparison of Nanoarchitecture to Porous Media Diffusion Models in Reduced

- Graphene Oxide/Aramid Nanofiber Electrodes for Supercapacitors,” *ACS Nano*, (2020).
- [136] I. Masselin, L. Durand-Bourlier, J.-M. Laine, P.-Y. Sizaret, X. Chassera, D. Lemordant, “Membrane Characterization Using Microscopic Image Analysis,” *Journal of Membrane Science*, 186 (2001) 85–96.
- [137] R. Ziel, A. Haus, A. Tulke, “Quantification of the Pore Size Distribution (Porosity Profiles) in Microfiltration Membranes by SEM, TEM And Computer Image Analysis,” *Journal of Membrane Science*, 323 (2008) 241–246.
- [138] P. Elia, E. Nativ-Roth, Y. Zeiri, Z. Porat, “Determination of the Average Pore-Size and Total Porosity in Porous Silicon Layers by Image Processing of SEM Micrographs,” *Microporous and Mesoporous Materials*, 225 (2016) 465–471.
- [139] M. Inagaki, T. Suwa “Pore Structure Analysis of Exfoliated Graphite Using Image Processing of Scanning Electron Micrographs,” *Carbon*, 39 (2001) 915–920.
- [140] X. Yuan, N. Xu, “Determination of Hydrogen Diffusion Coefficient in Metal Hydride Electrode by Cyclic Voltammetry,” *Journal of Alloys and Compounds*, 316 (2001) 113–117.
- [141] G. Leftheriotis, S. Papaefthimiou, P. Yianoulis, “Dependence of the Estimated Diffusion Coefficient of Li_xWO_3 Films on the Scan Rate of Cyclic Voltammetry Experiments,” *Solid State Ionics*, 178 (2007) 259–263.
- [142] N. Ding, J. Xu, Y.X. Yao, G. Wegner, X. Fang, C.H. Chen, I. Lieberwirth, “Determination of the Diffusion Coefficient of Lithium-Ions in Nano-Si,” *Solid State Ionics*, 180 (2009) 222–225.
- [143] R. H. French, V. A. Parsegian, R. Podgornik, R. F. Rajter, A. Jagota, J. Luo, D.

- AsthaGiri, M. K. Chaudhury, Y.-M. Chiang, S. Granick, S. Kalinin, M. Kardar, R. Kjellander, D. C. Langreth, J. Lewis, S. Lustig, D. Wesolowski, J. S. Wettlaufer, W.-Y. Ching, M. Finnis, "Long Range Interactions in Nanoscale Science," *Rev. Mod. Phys.*, 82 (2010) 1887–1944.
- [144] C. A. Silvera Batista, R. G. Larson, N. A. Kotov, "Nonadditivity of Nanoparticle Interactions," *Science*, 350 (2015) 1242477.
- [145] Y. Zhong, G. L. Warren, S. Patel, "Thermodynamic and Structural Properties of Methanol–Water Solutions Using Nonadditive Interaction Models," *Journal of Computational Chemistry*, 29 (2007) 1142–1152.
- [146] R. G. Compton, C. E. Banks, *Understanding Voltammetry*, World Scientific, Hackensack, New Jersey, 2007.
- [147] C. Batchelor-McAuley, E. Katelhon, E. O. Barnes, R. G. Compton, E. Laborda, A. Molina, "Recent Advances in Voltammetry," *Chemistry Open*, 4 (2015) 224 – 260.
- [148] G. A. Mabbott, "An Introduction to Cyclic Voltammetry," *Journal of Chemical Education*, 60 (1983) 697–702.
- [149] P. T. Kissinger, W. R. Heineman, *Laboratory Techniques in Electroanalytical Chemistry*. Dekker, New York, 1996.
- [150] J. Heinze, "Cyclic Voltammetry-Electrochemical Spectroscopy," *Angew. Chem. Int. Ed. Engl.*, 23 (1984) 831–847.
- [151] J. J. Van Benschoten, J. Y. Lewis, W. R. Heineman, D. A. Roston, P. T. Kissinger, "Cyclic Voltammetry Experiment," *Journal of Chemical Education*, 60 (1983) 772–776.
- [152] R. S. Nicholson, "Theory and Application of Cyclic Voltammetry for Measurement

- of Electrode Reaction Kinetics,” *Analytical Chemistry*, 37 (1965) 1351–1355.
- [153] D. O. Wipf, E. W. Kristensen, M. R. Deakin, R. M. Wightman, “Fast-Scan Cyclic Voltammetry as a Method to Measure Rapid Heterogeneous Electron-Transfer Kinetics,” *Analytical Chemistry*, 60 (1988) 306–310.
- [154] B. Wu, V. Yufit, Y. Merla, R. F. Martinez-Botas, N. P. Brandon, G. J. Offer, “Differential Thermal Voltammetry for Tracking of Degradation in Lithium-Ion Batteries,” *Journal of Power Sources*, 273 (2015) 495–501.
- [155] B. Garcia, S. Lavallée, G. Perron, C. Michot, M. Armand, “Room Temperature Molten Salts as Lithium Battery Electrolyte,” *Electrochimica Acta*, 49 (2004) 4583–4588.
- [156] L. Fransson, T. Eriksson, K. Edstrom, T. Gustafsson, J.O. Thomas, “Influence of Carbon Black and Binder on Li-Ion Batteries,” *Journal of Power Sources*, 101 (2001) 1–9.
- [157] Ben-Lin He, Bin Dong, Hu-Lin Li, “Preparation and Electrochemical Properties of Ag-Modified TiO₂ Nanotube Anode Material for Lithium-Ion Battery,” *Electrochemistry Communications*, 9 (2007) 425–430.
- [158] M. Takahashi, S. Tobishima, K. Takei, Y. Sakurai, “Reaction Behavior of LiFeO₄ as a Cathode Material for Rechargeable Lithium Batteries,” *Solid State Ionics*, 148 (2002) 283–289.
- [159] H. Yamada, H. Nakamura, F. Nakahara, I. Moriguchi, T. Kudo, “Electrochemical Study of High Electrochemical Double Layer Capacitance of Ordered Porous Carbons with Both Meso/Macropores and Micropores,” *J. Phys. Chem. C*, 111 (2007) 227–233.
- [160] M. H. Chakrabarti, R. A. W. Dryfe, E. P. L. Roberts, “Evaluation of Electrolytes

- for Redox Flow Battery Applications,” *Electrochimica Acta*, 52 (2007) 2189–2195.
- [161] H. Kaneko, K. Nozaki, Y. Wada, T. Aoki, A. Negishi, M. Kamimoto, “Vanadium Redox Reactions and Carbon Electrodes for Vanadium Redox Flow Battery,” *Electrochimica Acta*, 36 (1991) 1191–1196.
- [162] Z. González, A. Sánchez, C. Blanco, M. Granda, R. Menéndez, R. Santamaria, “Enhanced Performance of a Bi-Modified Graphite Felt as the Positive Electrode of a Vanadium Redox Flow Battery,” *Electrochemistry Communications*, 13 (2011) 1379–1382.
- [163] K. Lin, Q. Chen, M. R. Gerhardt, L. Tong, S. B. Kim, L. Eisenach, A. W. Valle, D. Hardee, R. G. Gordon, M. J. Aziz, M. P. Marshak, “Alkaline Quinone Flow Battery,” *Science*, 349 (2015) 1529–1532.
- [164] H. Q. Zhu, Y. M. Zhang, L. Yue, W. S. Li, G. L. Li, D. Shu, H. Y. Chen, “Graphite–Carbon Nanotube Composite Electrodes for All Vanadium Redox Flow Battery,” *Journal of Power Sources*, 184 (2008) 637–640.
- [165] K. Fricke, F. Harnisch, U. Schröder, “On the Use of Cyclic Voltammetry for the Study of Anodic Electron Transfer in Microbial Fuel Cells,” *Energy Environ. Sci.*, 1 (2008) 144–147.
- [166] M. M. P. Janssen, J. Moolhuysen, “State and Action of the Tin Atoms in Platinum–Tin Catalysts for Methanol Fuel Cells,” *Journal of Catalysis*, 46 (1977) 289–296.
- [167] E. Gyenge, “Electrooxidation of Borohydride on Platinum and Gold Electrodes: Implications for Direct Borohydride Fuel Cells,” *Electrochimica Acta*, 49 (2004) 965–978.
- [168] S. J. C. Cleghorn, D. K. Mayfield, D. A. Moore, J. C. Moore, G. Rusch, T. W.

- Sherman, N. T. Sisofo, U. Beuscher, “A Polymer Electrolyte Fuel Cell Life Test: 3 Years of Continuous Operation,” *Journal of Power Sources*, 158 (2006) 446–454.
- [169] A. Taniguchi, T. Akita, K. Yasuda, Y. Miyazaki, “Analysis of Electrocatalyst Degradation in PEMFC Caused by Cell Reversal During Fuel Starvation,” *Journal of Power Sources*, 130 (2004) 42–49.
- [170] M. Aulice Scibioh, S.-K. Kim, E. A. Cho, T.-H. Lim, S.-A. Hong, H. Y. Ha, “Pt-CeO₂/C Anode Catalyst for Direct Methanol Fuel Cells,” *Applied Catalysis B: Environmental*, 84 (2008) 773–782.
- [171] E. Frackowiak, F. Beguin, “Carbon Materials for Supercapacitor Application,” *Carbon*, 39 (2001) 937.
- [172] W. G. Pell, B. E. Conway, “Analysis of Power Limitations at Porous Supercapacitor Electrodes Under Cyclic Voltammetry Modulation and DC Charge,” *Journal of Power Sources*, 96 (2001) 57–67.
- [173] A. Laforgue, P. Simon, C. Sarrazin, J.F. Fauvarque, “Polythiophene-Based Supercapacitors,” *Journal of Power Sources*, 80 (1999) 142–148.
- [174] D. Zhang, X. Zhang, Y. Chen, P. Yu, C. Wang, Y. Ma, “Enhanced Capacitance and Rate Capability of Graphene/Polypyrrole Composite as Electrode Material for Supercapacitors,” *Journal of Power Sources*, 196 (2011) 5990–5996.
- [175] H. Gómez, M. K. Ram, F. Alvi, P. Villalba, E. Stefanakos, A. Kumar, “Graphene-Conducting Polymer Nanocomposite as Novel Electrode for Supercapacitors,” *Journal of Power Sources*, 196 (2011) 4102–4108.

- [176] C.-C. Hu, K.-H. Chang, "Cyclic Voltammetric Deposition of Hydrous Ruthenium Oxide for Electrochemical Supercapacitors: Effects of the Chloride Precursor Transformation," *Journal of Power Sources*, 112 (2002) 401–409.
- [177] J. F. Arteaga, M. Ruiz-Montoya, A. Palma, G. Alonso-Garrido, S. Pintado, J. M. Rodríguez-Mellado, "Comparison of the Simple Cyclic Voltammetry (CV) and DPPH Assays for the Determination of Antioxidant Capacity of Active Principles," *Molecules*, 17 (2012) 5126–5138.
- [178] M. A. Samra, V. S. Chedea, A. Economou, A. Calokerinos, P. Kefalas, "Antioxidant/Prooxidant Properties of Model Phenolic Compounds: Part I. Studies on Equimolar Mixtures by Chemiluminescence and Cyclic Voltammetry," *Food Chem.*, 125, (2011) 622–629.
- [179] S. Chevion, M. A. Roberts, M. Chevion, "The Use of Cyclic Voltammetry for the Evaluation of Antioxidant Capacity," *Free Rad. Biol. Med.*, 28 (2000) 860–870.
- [180] S. Martinez, L. Valek, J. Resetic, D. Ferenec Ruzic, "Cyclic Voltammetry Study of Plasma Antioxidant Capacity. Comparison with the DPPH and TAS Spectrophotometric Methods," *J. Electroanal. Chem.*, 588 (2006) 68–73.
- [181] A. Gomes, E. Fernandes, M. B. Garcia, A. M. Silva, D. C. Pinto, C. M. Santos, J. A. Cavaleiro, J. L. Lima, "Cyclic Voltammetric Analysis of 2-Styrylchromones: Relationship with the Antioxidant Activity," *Bioorg. Med. Chem.*, 16 (2008) 7939–7943.
- [182] B. E. Conway, W. G. Pell, "Power Limitations of Supercapacitor Operation Associated with Resistance and Capacitance Distribution in Porous Electrode Devices," *Journal of Power Sources*, 105 (2002) 169–181.

- [183] S. Yoon, J. H. Jang, B. H. Ka, S. M. Oh, “Complex Capacitance Analysis on Rate Capability of Electric-Double Layer Capacitor (EDLC) Electrodes of Different Thickness,” *Electrochimica Acta*, 50 (2005) 2255–2262.
- [184] O. Bohlen, J. Kowal, D. Sauer, “Ageing Behavior of Electrochemical Double Layer Capacitors: Part I. Experimental Study and Ageing Model,” *Journal of Power Sources*, 172 (2007) 468–475.
- [185] S. Yoon, C. W. Lee, S. M. Oh, “Characterization of Equivalent Series Resistance of Electric Double-Layer Capacitor Electrodes Using Transient Analysis,” *Journal of Power Sources*, 195 (2010) 4391–4399.
- [186] R. Spyker, R. Nelms, “Classical Equivalent Circuit Parameters for a Double-Layer Capacitor,” *IEEE Transactions on Aerospace and Electronic Systems*, 36 (2000) 829–836.
- [187] M. Z. Bazant, K. Thornton, A. Ajdari, “Diffuse-Charge Dynamics in Electrochemical Systems,” *Physical Review E*, 70 (2004) 021506.
- [188] L. H. Olesen, M. Z. Bazant, H. Bruus, “Strongly Nonlinear Dynamics of Electrolytes in Large AC Voltages,” *Physical Review E*, 82 (2010) 011501.
- [189] K. T. Chu, M. Z. Bazant, “Nonlinear Electrochemical Relaxation Around Conductors,” *Physical Review E*, 74 (2006) 011501.
- [190] R. De Levie, “On Porous Electrodes in Electrolyte Solutions-IV,” *Electrochimica Acta*, 9 (1964) 1231–1245.
- [191] J. F. Robinson, Y. P. Kayinamura, “Charge Transport in Conducting Polymers: Insights from Impedance Spectroscopy,” *Chemical Society Reviews*, 38 (2009) 3339–3347.

- [192] M. G. Ancona, S. D. Jhaveri, D. A. Lowy, L. M. Tender, E. E. Foos, A. W. Snow, "Modeling Cyclic Voltammetry of Electrode-Immobilized Gold Nanoclusters," *Electrochimica Acta*, 48 (2003) 4157–4165.
- [193] M. D. Levi and D. Aurbach, "Simultaneous Measurements and Modeling of the Electrochemical Impedance and the Cyclic Voltammetric Characteristics of Graphite Electrodes Doped with Lithium," *J. Phys. Chem. B*, 101 (1997) 4630–4640.
- [194] R. Burt, G. Birkett, X. Zhao, "A Review of Molecular Modelling of Electric Double Layer Capacitors," *Physical Chemistry Chemical Physics*, 16 (2014) 6519–6538.
- [195] N. Georgi, A. A. Kornyshev, M. V. Fedorov, "The Anatomy of the Double Layer and Capacitance in Ionic Liquids with Anisotropic Ions: Electrostriction Vs. Lattice Saturation," *J. Electroanal. Chem.*, 649 (2010) 261–267.
- [196] M. Z. Bazant, B. D. Storey, A. A. Kornyshev, "Double Layer in Ionic Liquids: Overscreening Versus Crowding," *Physical Review Letter*, 106 (2011) 046102.
- [197] C. Cagle, G. Feng, R. Qiao, J. Huang, B. G. Sumpter, V. Meunier, "Structure and Charging Kinetics of Electrical Double Layers at Large Electrode Voltages," *Microfluidics and Nanofluidics*, 8 (2010) 703–708.
- [198] M. V. Fedorov, A. A. Kornyshev, "Towards Understanding the Structure and Capacitance of Electrical Double Layer in Ionic Liquids," *Electrochimica Acta*, 53 (2008) 6835–6840.
- [199] X. Jiang, J. Huang, H. Zhao, B. G. Sumpter, R. Qiao, "Dynamics of Electrical Double Layer Formation in Room-Temperature Ionic Liquids Under Constant-Current Charging Conditions," *Journal of Physics: Condensed Matter*, 26 (2014) 284109.

- [200] C. Merlet, B. Rotenberg, P. A. Madden, P.-L. Taberna, P. Simon, Y. Gogotsi, M. Salanne, “On the Molecular Origin of Supercapacitance in Nanoporous Carbon Electrodes,” *Nature Materials* 11 (2012) 306–310.
- [201] J. E. Heffner, J. C. Raber, O. A. Moe, C. T. Wigal, “Using Cyclic Voltammetry and Molecular Modeling to Determine Substituent Effects in the One-Electron Reduction of Benzoquinones,” *J. of Chemical Education*, 75 (1998) 365–367.
- [202] H. Wang and L. Pilon, “Accurate Simulations of Electric Double Layer Capacitance of Ultramicroelectrodes,” *J. Phys. Chem. C*, 115 (2011) 16711–16719.
- [203] H. Wang, L. Pilon, “Physical Interpretation of Cyclic Voltammetry for Measuring Electric Double Layer Capacitances,” *Electrochimica Acta*, 64 (2012) 130–139.
- [204] H. Wang, A. Thiele, L. Pilon, “Simulations of Cyclic Voltammetry for Electric Double Layers in Asymmetric Electrolytes: A Generalized Modified Poisson- Nernst-Planck Model,” *J. Phys. Chem. C*, 117 (2013) 18286–18297.
- [205] H. Wang, L. Pilon, “Mesoscale Modeling of Electric Double Layer Capacitors with Three-Dimensional Ordered Structures,” *Journal of Power Sources*, 221 (2013) 252–260.
- [206] B. A. Mei, L. Pilon, “Three-Dimensional Cyclic Voltammetry Simulations of EDLC Electrodes Made of Ordered Carbon Spheres,” *Electrochimica Acta*, 255 (2017) 168–178.
- [207] I. Streeter, G. G. Wildgoose, L. Shao, R. G. Compton, “Cyclic Voltammetry on Electrode Surfaces Covered with Porous Layers: An Analysis of Electron Transfer Kinetics at Single-Walled Carbon Nanotube Modified Electrodes,” *Sensors and Actuators B*, 133 (2008) 462–466.

- [208] C. Lian, D. Jiang, H. Liu, J. Wu, “A Generic Model for Electric Double Layers in Porous Electrodes,” *J. Phys. Chem. C*, 120 (2016) 8704–8710.
- [209] M. Kroupa, G. J. Offer, J. Kosek, “Modelling of Supercapacitors: Factors Influencing Performance,” *J. Electrochem. Soc.*, 163 (2016) A2475-A2487.
- [210] F. G. Chevallier, L. Jiang, T. G. J. Jones, R. G. Compton, “Mathematical Modelling and Numerical Simulation of Cyclic Voltammetry at an Electrode Covered with an Insulating Film Containing Cylindrical Micropores,” *J. Electroanalytical Chemistry* 587 (2006) 254–262.
- [211] P. J. Pearce, A. J. Bard “Polymer Films on Electrodes Part III. Digital Simulation Model for Cyclic Voltammetry of Electroactive Polymer Film and Electrochemistry of Poly (Vinyl ferrocene) on Platinum,” *J. Electroanal. Chem.*, 114 (1980) 89–115.
- [212] A. M. Bond, R. J. O'halloran, I. Ruzic, D. E. Smith, “A.C. Cyclic Voltammetry: A Digital Simulation Study of the Slow Scan Limit Condition for a Reversible Electrode Process,” *Electroanal. Chem.*, 90 (1978) 381–388.
- [213] D. H. Johnston, H. H. Thorp, “Cyclic Voltammetry Studies of Polynucleotide Binding and Oxidation by Metal Complexes: Homogeneous Electron-Transfer Kinetics,” *J. Phys. Chem.*, 100 (1996) 13837–13843.
- [214] T. D. Dongale, P. R. Jadhav, G. J. Navathe, J. H. Kim, M. M. Karanjkar, P. S. Patil, “Development of Nano Fiber MnO₂ Thin Film Electrode and Cyclic Voltammetry Behavior Modeling Using Artificial Neural Network for Supercapacitor Application,” *Materials Science in Semiconductor Processing*, 36 (2015) 43–48.
- [215] D. J. Gavaghan, A. M. Bond, “A Complete Numerical Simulation of the Techniques of Alternating Current Linear Sweep and Cyclic Voltammetry: Analysis of

- a Reversible Process by Conventional and Fast Fourier Transform Methods,” *J. Electroanalytical Chemistry*, 480 (2000) 133–149.
- [216] K. B. Oldham, J. C. Myland, “Modelling Cyclic Voltammetry Without Digital Simulation,” *Electrochimica Acta*, 56 (2011) 10612–10625.
- [217] A. Lavacchi, U. Bardi, C. Borri, S. Caporali, A. Fossati, I. Perissi, “Cyclic Voltammetry Simulation at Microelectrode Arrays with COMSOL Multiphysics,” *J. Appl. Electrochem.*, 39 (2009) 2159–2163.
- [218] K. Xu, “Nonaqueous Liquid Electrolytes for Lithium-Based Rechargeable Batteries,” *Chem. Rev.*, 104 (2004) 4303–4417.
- [219] D. Ouyang, M. Chen, Q. Huang, J. Weng, Z. Wang, J. Wang, “A Review on the Thermal Hazards of the Lithium-Ion Battery and the Corresponding Countermeasures,” *Appl. Sci.*, 9 (2019) 2483.
- [220] P. Yao, H. Yu, Z. Ding, Y. Liu, J. Lu, M. Lavorgna, J. Wu, X. Liu, “Review on Polymer-Based Composite Electrolytes for Lithium Batteries,” *Frontiers in Chemistry*, 7 (2019) 522.
- [221] D. Ouyang, Y. He, J. Weng, J. Liu, M. Chen, J. Wang, “Influence of Low Temperature Conditions on Lithium-Ion Batteries and the Application of an Insulation Material,” *RSC Adv.*, 9 (2019) 9053–9066.
- [222] S. Abada, G. Marlair, A. Lecocq, M. Petit, V. Sauvant-Moynot, F. Huet, “Safety Focused Modeling of Lithium-Ion Batteries: A Review,” *Journal of Power Sources*, 306 (2016) 178–192.

- [223] M. Doyle, T. F. Fuller, J. Newman, “Modeling of Galvanostatic Charge and Discharge of the Lithium/Polymer/Insertion Cell,” *J. Electrochem. Soc.*, 140 (1993) 1526–1533.
- [224] M. Guo, G. Sikha, R. E. White, “Single-Particle Model for a Lithium-Ion Cell: Thermal Behavior,” *J. Electrochem. Soc.*, 158 (2011) A122–A132.
- [225] Y. Ye, Y. Shi, N. Cai, J. Lee, and X. He, “Electro-Thermal Modeling and Experimental Validation for Lithium-Ion Battery,” *Journal of Power Sources*, 199 (2012) 227–238.
- [226] K. Somasundaram, E. Birgersson, A. S. Mujumdar, “Thermal–Electrochemical Model for Passive Thermal Management of a Spiral-Wound Lithium-Ion Battery,” *Journal of Power Sources*, 203 (2012) 84–96.
- [227] J. Newman, and W. Tiedemann, “Potential and Current Distribution in Electrochemical Cells Interpretation of the Half-Cell Voltage Measurements as a Function of Reference-Electrode Location,” *J. Electrochem. Soc.*, 140 (1993) 1962–1968.
- [228] D. Danilov, R. A. H. Niessen, P. H. L. Notten, “Modeling All-Solid-State Li-Ion Batteries,” *J. Electrochem. Soc.*, 158 (2011) A215–A222.
- [229] Y. Ji, Y. Zhang, C.-Y. Wang, “Li-Ion Cell Operation at Low Temperatures,” *J. Electrochem. Soc.*, 160 (2013) A636–A649.
- [230] S. Tippmann, D. Walper, L. Balboa, B. Spier, W. G. Bessler, “Low-Temperature Charging of Lithium-Ion Cells Part I: Electrochemical Modeling and Experimental Investigation of Degradation Behavior,” *Journal of Power Sources*, 252 (2014) 305–316.

- [231] K. Kumaresan, G. Sikha, R. E. White, “Thermal Model for a Li-Ion Cell,” *J. Electrochem. Soc.*, 155 (2008) A164–A171.
- [232] W. B. Gu, C. Y. Wang, “Thermal-Electrochemical Modeling of Battery Systems,” *J. Electrochem. Soc.*, 147 (2000) 2910–2922.
- [233] C. R. Pals, J. Newman, “Thermal Modeling of the Lithium/Polymer Battery: I. Discharge Behavior of a Single Cell,” *J. Electrochem. Soc.*, 142 (1995) 3282.

Appendix A

A.1 Fabrication of rGO/ANF Composite Structural Electrodes

A.1.1 Vacuum Filtration Method

Graphene oxide (GO) was synthesized using the modified Hummers method [51]. Aramid nanofibers (ANFs) were prepared by dissolving bulk Kevlar® thread in dimethyl sulfoxide (DMSO) and potassium hydroxide (KOH), as described in previous reports [15][16][70]. The electrodes were fabricated using vacuum-assisted filtration while the total mass was held constant at 40 mg. More specifically, desired amounts of GO/DMSO and ANF/DMSO were mixed and stirred together for one hour. Then, deionized water was added to assist the formation of hydrogen bonding between the ANF amide bonds and the oxygen containing groups of GO. The mixture was heated for two hours and filtrated on a nylon membrane (47 mm diameter and 0.2 μm pore size). The electrodes were peeled off and dried in a vacuum oven at 80°C for 3 days. Finally, the composite electrodes were thermally reduced under vacuum at 200°C [15][16]. The morphology of the electrodes was characterized through scanning electron microscopy (SEM) (JSM-7500F, JEOL).

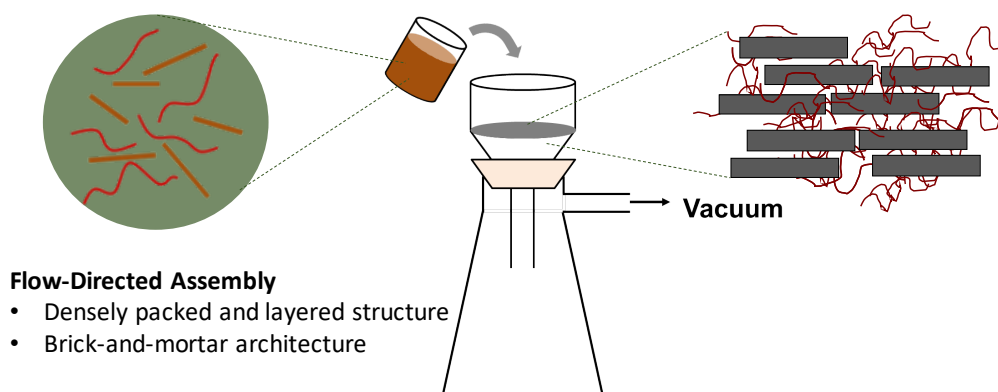


Figure A.1 Schematics of vacuum filtration method [15][16][17][18][108].

A.1.2 Sol-Gel Method

This method is reported in references [19][72]. The GO-ANF mixture in DMSO/water was solvent exchanged to water using dialysis. As-obtained aqueous GO-ANF mixture was concentrated in a rotary evaporator to yield a GO-ANF slurry with a GO loading of 10 mg/ml. For sol-gel reaction, the aqueous GO- ANF slurry was mixed with ammonium hydroxide (NH_4OH), with a $\text{NH}_4\text{OH}/\text{GO}$ ratio (v/w) of 0.024 mL/mg. $\text{GO}(\text{ANF}_X)$ hydrogels with desired ANF concentration (X wt.% dry solid basis) were obtained by heating the aqueous GO-ANF- NH_4OH mixture at 90°C in a sealed hydrothermal chamber for 3 days. Excess ammonia and reaction byproducts were removed by washing with DI water. Then, an additional chemical reduction step is performed to obtain rGO (ANF_X) hydrogels by treating $\text{GO}(\text{ANF}_X)$ hydrogels in 40 mg/ml aqueous L-sodium ascorbate solution at 90°C for 5 h. The residual L-sodium ascorbate and reaction byproducts were removed by washing with DI water [19]

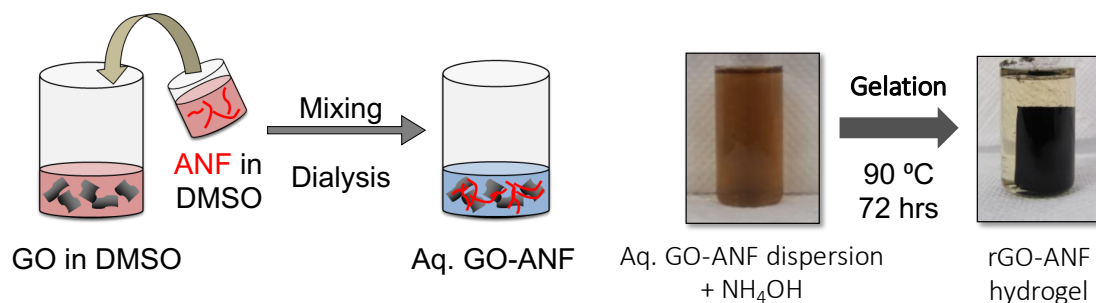


Figure A.2 Schematics of sol-gel method [19][72].

A.2 Mathematical Relations for Energy and Power in Supercapacitors

The following equations are regarding diffusion current and capacitance in supercapacitors [7][92][93][114][115][116]. It can be seen that increasing the ionic diffusivity directly increases the diffusion current as well as the energy and power in supercapacitors. The flux relation with current density and concentration gradient is [114][115]

$$J(x, t) = -\frac{i_d}{zFA} = -D \frac{\partial c(x, t)}{\partial x}, \quad (\text{A. 1})$$

where J is the ionic flux ($\text{mol.m}^{-2} \cdot \text{s}^{-1}$), i_d is the diffusion current (A), z is charge number, F is the Faraday's constant (C/mol), A is the area normal to the flux (m^2), D is diffusion coefficient (m^2/s), and c is the concentration (mol/m^3). The simplified equation for diffusion current is described as [114]

$$i_d = zFAD \frac{\partial c(x, t)}{\partial x}. \quad (\text{A. 2})$$

The capacitance, C (μF) of a supercapacitor is the ratio of the change in electric charge, q , to the corresponding change in its electric potential, V , as [92][93]

$$C = \frac{\Delta q}{\Delta V} = i_d \frac{\Delta t}{\Delta V}. \quad (\text{A. 3})$$

The energy, W (J), of a supercapacitor is related to the capacitance (C) and applied voltage (V) as described in the form of [94]

$$W = \frac{1}{2} CV^2, \quad (\text{A. 4})$$

and the power is the energy vs time as

$$P = \frac{dW}{dt} = \frac{d}{dt} \left[\frac{1}{2} CV^2 \right]. \quad (\text{A. 5})$$

A.3 Determination of ionic diffusivity through experimental measurements

The ionic diffusivity of K^+ and OH^- ions through cyclic voltammetry measurements can be determined through Randles-Sevcik equation [88] as

$$i_p = 0.4463 zFAc \left(\frac{zFvD}{RT} \right)^{1/2}, \quad (A.6)$$

where, D is the diffusion coefficient (m^2/s), i_p is the peak current (A) obtained from CV plots, z is the charge number, v is the scan rate (V/s), A is the electrode surface area (m^2), and c is the ionic concentration (mol/m^3).

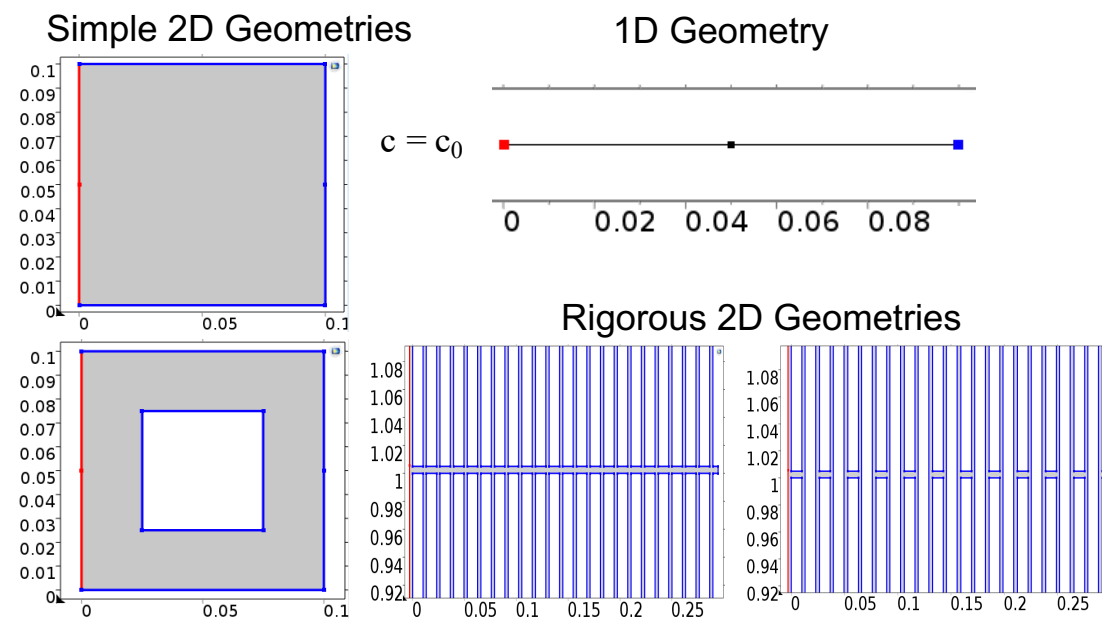


Figure A.3 1D and 2D geometry development with boundary conditions; blue indicates zero flux and red indicates $c=c_0$ [108].

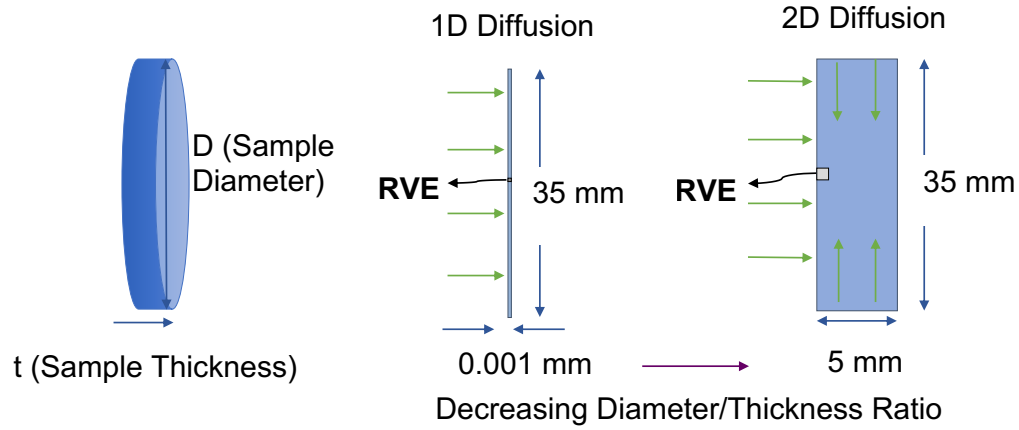


Figure A.4 One-dimensional diffusion mass transfer is preferred in thin films, when the value of diameter/thickness ratio of the sample is large enough to neglect the diffusion of ions from the sample edges [108].

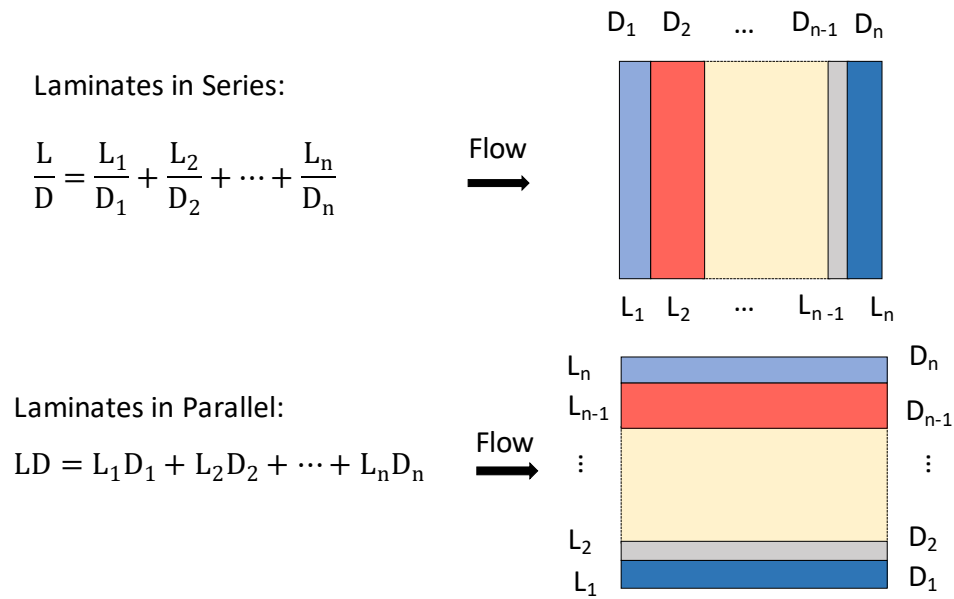


Figure A.5 Series and parallel laminates and related equations to determine effective diffusion coefficient [108][117][118].

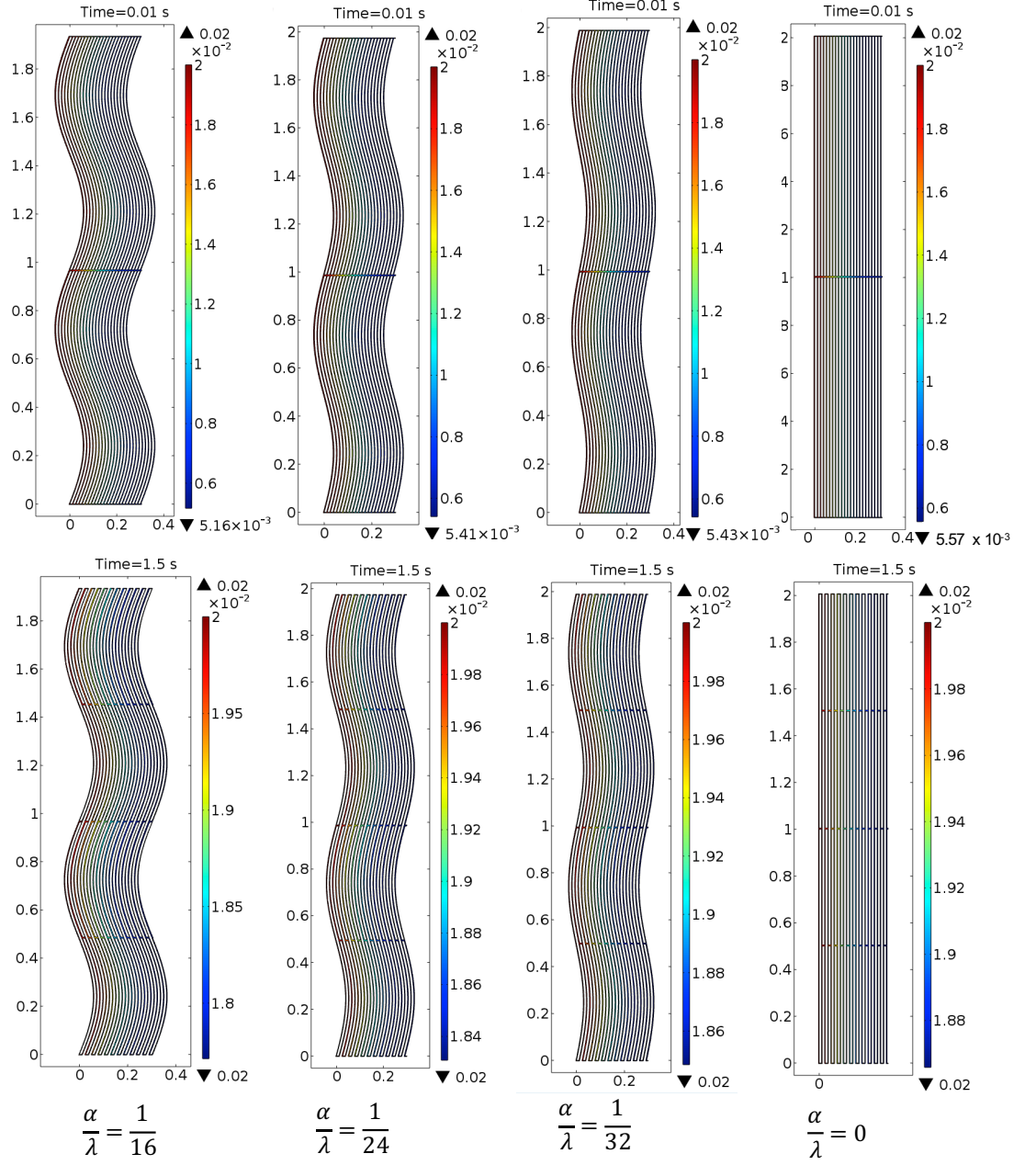


Figure A.6 Concentration contour plots for rGO/25wt%ANF in aligned and staggered arrangements with various degrees of waviness of $a/\lambda = 1/16, 1/24, 1/32$, and 0 (straight sheets) [108].

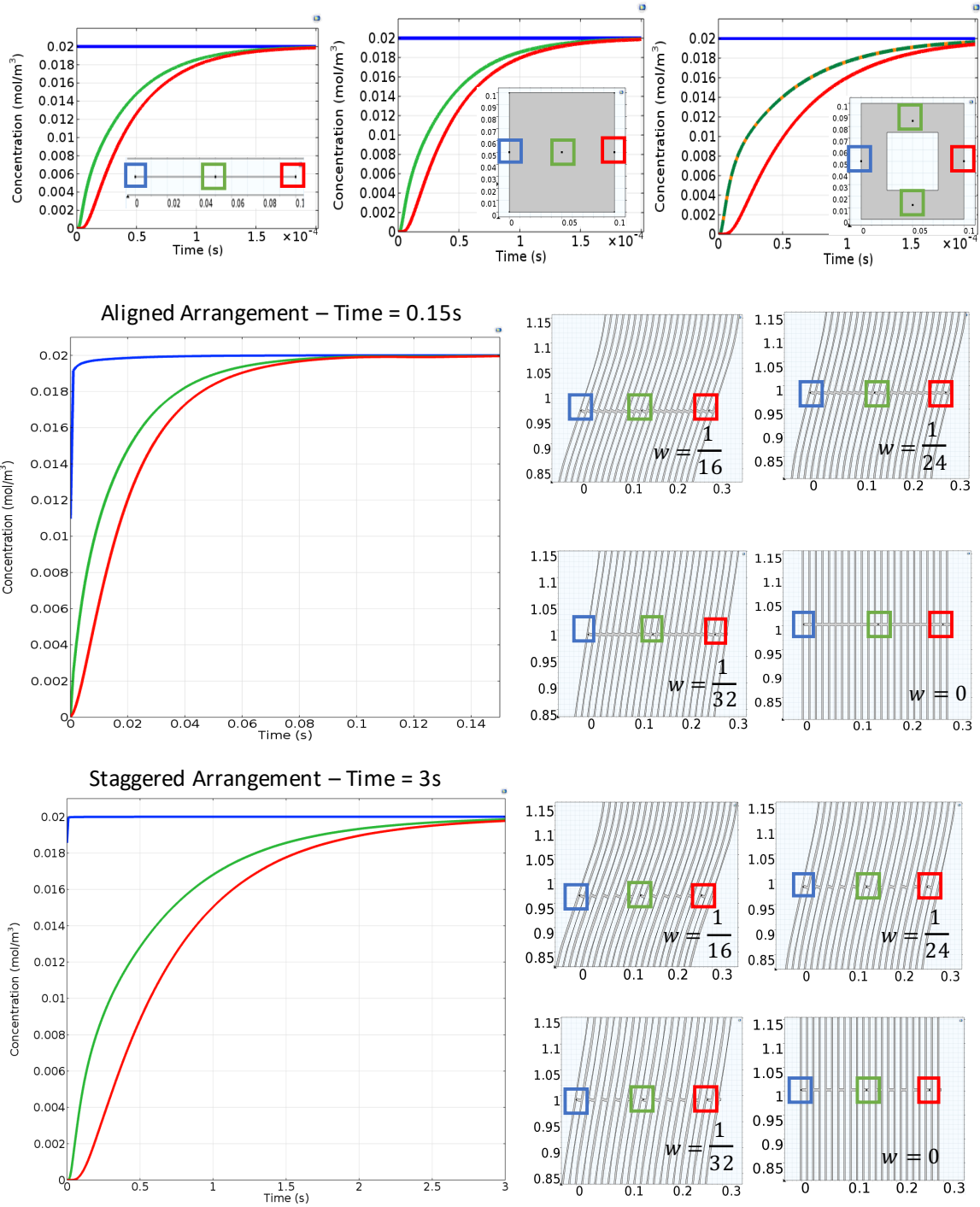


Figure A.7 Concentration-time plot of 3-points in the geometry- left (blue), middle (green), and right (red). These plots indicate that how ion transfer develops through the geometry in three-time stages: (1) time needed for ions to reach the point, (2) transient, and (3) equilibrium [108].

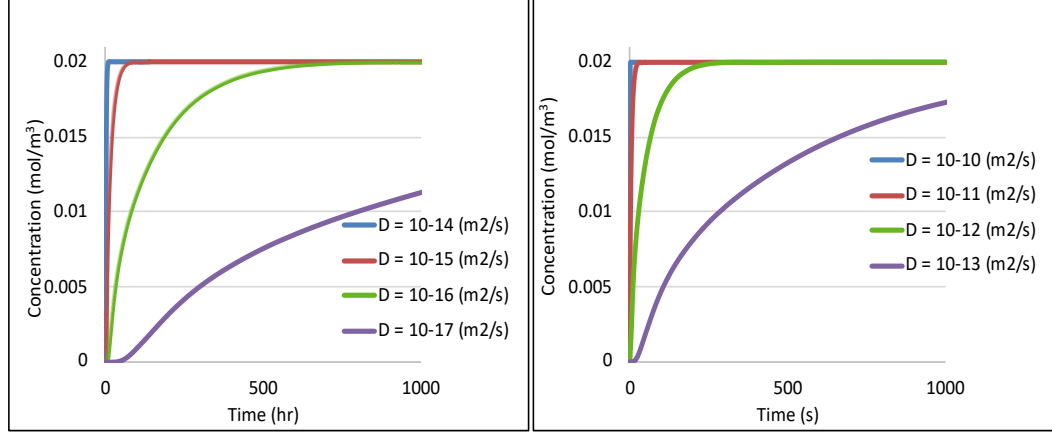


Figure A.8 The effect of diffusion coefficient on concentration for staggered arrangement with $w = 1/24$, $D = 10^{-17} \text{ m}^2/\text{s}$ to $D = 10^{-10} \text{ m}^2/\text{s}$ [108].

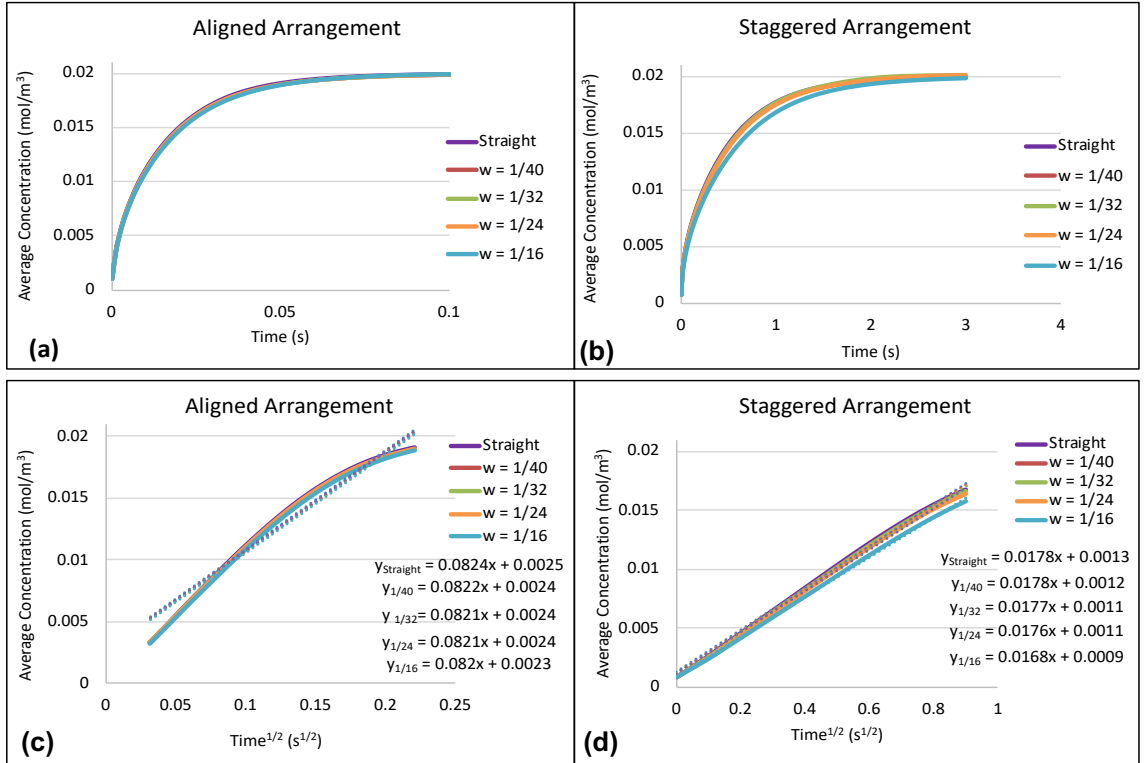


Figure A.9 (a),(b) Average concentration-time plots for aligned and staggered arrangements ($D = 10^{-10} \text{ m}^2/\text{s}$). Increasing waviness of rGO sheets, decreases the ionic concentration in both aligned and staggered arrangements. (c),(d) Average concentration-time^{1/2} plots for aligned and staggered arrangements ($D = 10^{-10} \text{ m}^2/\text{s}$) is used to calculate effective diffusivity and tortuosity [108].

Table A.1 Diffusion coefficient (m^2/s) for common ions in various electrolytes [108].

Species	Aqueous Electrolytes	Organic Electrolytes	Carbon Electrodes	Polymer Electrolyte
Li^+	10^{-5} [119]	$10^{-5} - 10^{-6}$ [120]	$10^{-6} - 10^{-12}$ [120]	10^{-8} (PEO) [120]
Na^+	10^{-5} [121]	$10^{-10} - 10^{-12}$ [122]	$10^{-12} - 10^{-13}$ [123]	$10^{-7} - 10^{-9}$ [124]
K^+	10^{-5} [121]	$10^{-10} - 10^{-12}$ [125]	$10^{-9} - 10^{-10}$ [126]	NA
Mg^{2+}	10^{-5} [121]	$10^{-10} - 10^{-12}$ [25]	NA	NA

NA: Not Available

Appendix B

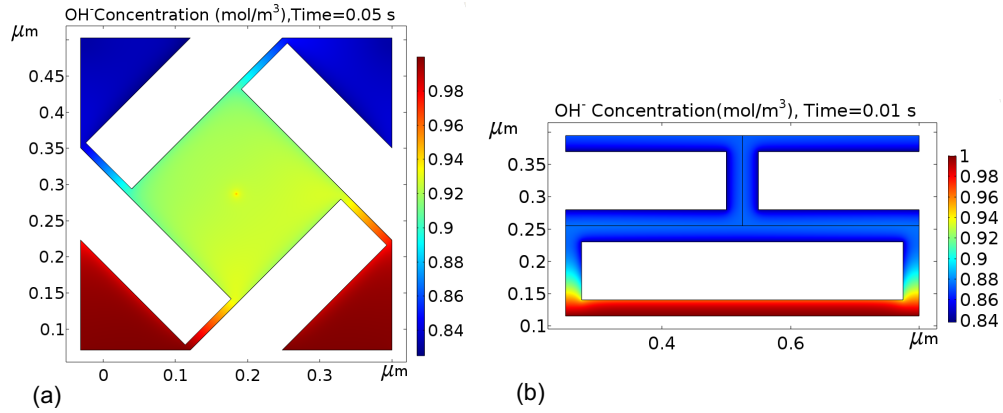


Figure B.1 Concentration contour plots for OH^- ions in (a) square unit cell for house of cards, and (b) staggered unit cell for layered nanoarchitectures [135].

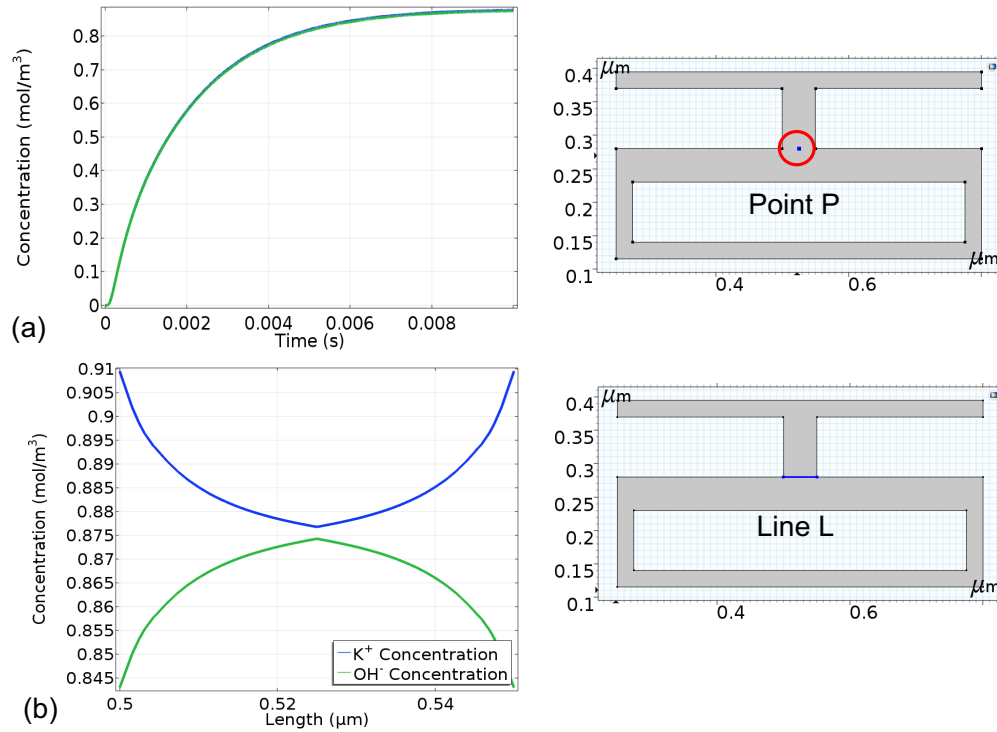


Figure B.2 (a) Concentration-time plot for K^+ and OH^- at point P in staggered unit cell for layered nanostructure shows a Fickian diffusion behavior. (b) concentration development of K^+ and OH^- along line L in the nanochannel indicates that K^+ ions are accumulated at the rGO/ANF surface due to negatively charged surfaces and OH^- ions are repelled from the surfaces [135].

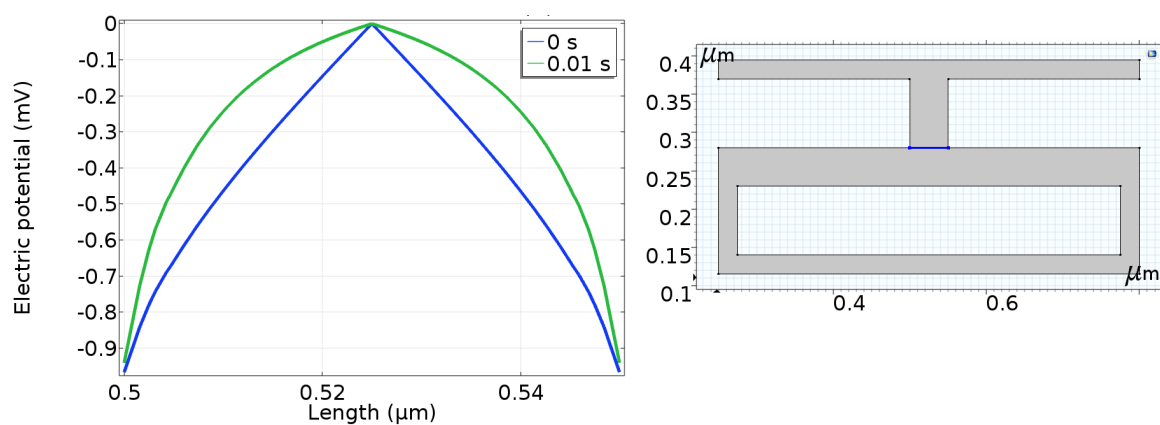


Figure B.3 Electric potential for line L in the nanochannel at time 0s and 0.01s, the electric potential is -1 mV at the rGO/ANF surface and goes to zero at the boundary condition in the middle of nanochannel [135].

